

Aus dem Departement für Physik
Universität Freiburg (Schweiz)



Optical magnetic resonance tomography
and
Laser spectroscopy of cesium atoms trapped in solid
helium

Inaugural-Dissertation

zur Erlangung der Würde eines
Doctor rerum naturalium
der Mathematisch-Naturwissenschaftlichen Fakultät
der Universität Freiburg in der Schweiz

vorgelegt von

Daniel Nettels

aus Münster (Deutschland)

Nummer der Dissertation:
Paulusdruckerei Freiburg
2003

Von der Mathematisch-Naturwissenschaftlichen Fakultät der Universität Freiburg in der Schweiz angenommen, auf Antrag der Herren

Prof. Dr. Fritz Müller , Universität Freiburg (Präsident der Jury)

Prof. Dr. Antoine Weis, Universität Freiburg (Referent)

Prof. Dr. Jean-Claude Dousse, Universität Freiburg (Koreferent)

Priv.-Doz. Dr. Robert Wynands, PTB Braunschweig (Koreferent)

Freiburg, den 17. Dezember 2003

Der Leiter der Dissertation



Prof. Dr. Antoine Weis

Der Dekan



Prof. Dr. Dionys Baeriswyl

Abstract

The present thesis has resulted from my research work carried out at the University of Bonn and at the University of Fribourg. The thesis can be roughly divided into two distinct parts, which reflect the research carried out in both places. In Bonn I worked on optical magnetic resonance tomography of atoms in the gas phase, while all of my time in Fribourg was devoted to study specific problems of foreign atoms trapped in solid helium crystals. The results are given in terms of five publications (two published, 2 accepted for publication and one in the process of being submitted).

The magnetic resonance tomography discussed in the first part is a novel technique, which allowed us the two-dimensional imaging of the motion of spin-polarized alkali atoms in a buffer gas using magnetic resonance spectroscopy combined with optical preparation and optical read-out. I have applied this novel technique to study the diffusion of cesium atoms in a gas of neon atoms, and to determine the diffusion coefficient D_0 of that motion to be $0.20(1) \text{ cm}^2/\text{s}$ in standard conditions.

The second and main part of this work presents research on the optical and magneto-optical properties of cesium atoms trapped in solid ^4He . The experiments were performed either in the hexagonal close-packed (hcp) or in the body-centered cubic (bcc) phase of solid helium. The matrix-isolated cesium atoms reside in bubble-like cavities, which have a spherical shape, when the atom is in its radially symmetric $6S_{1/2}$ ground state. The spherical symmetry and the purely none-magnetic properties of helium make that extremely long electron spin relaxation times ($\approx 1\text{s}$) of the cesium atoms can be observed in the isotropic bcc phase. On the other hand, magnetic resonance lines measured in the hcp phase are significantly broader (by three orders of magnitude) and show a complex substructure due to a small deformation of the bubble shape.

There was a long standing mystery in the literature regarding the fluorescence of alkali atoms in condensed helium: while the heavy alkalis Cs and Rb emitted fluorescence light, no fluorescence could be detected from the lighter alkali atoms, and it was commonly accepted that the emission is quenched by the formation of exciplex molecules, i.e., bound states of excited alkali atoms and one or several helium atoms. It was also believed that such exciplexes would not exist for cesium. In the present work the research was extended to the investigation of the atomic D_2 -excitation and to a detailed study of the subsequent deexcitation of the $6P_{3/2}$ state. No direct D_2 emission had been observed in the past. Only a weak D_1 emission following the D_2 excitation was detected indicating the existence a quenching channel to the $6P_{1/2}$ state. By extending the wavelength range of our detection system two new, broad and intense emission lines were discovered at 7130 cm^{-1} and 10520 cm^{-1} . The energetically higher emission line was recently also observed in a cold helium gas environment and in liquid helium by a group at Kyoto University. The origin of this line could be attributed to the decay of Cs^*He_2 exciplexes, where the electronic state of this complex is denoted as $A\Pi_{3/2}$ in molecular spectroscopic notation. The second line could not be observed in He gas nor in liquid He and may occur in a solid helium environment only. In order to assign the new lines to specific exciplex structures we have performed model calculation of the emission spectra of decaying Cs^*He_n exciplexes using semi-empirical Cs-He pair potentials. By comparison with the experimental data it could be confirmed that the first emission line corresponds indeed to the decay of Cs^*He_2 . The energetically lower

second line originates from a different exciplex. Our calculations suggest that the corresponding structure consist of an excited cesium atom of dumbbell-like shaped electronic configuration with a ring of n helium atoms bound around its waist. The exact number n of bound helium atoms could not definitely assigned, because of a lacking precision of the calculation. However, Cs^*He_6 seems to be the most probable candidate with our present knowledge. Cs^*He_n exciplexes with $n > 2$ were not observed previously, thus seemingly confirming statements found in the literature that these complexes are not stable. Finally, a third, very faint emission line was discovered at 10160 cm^{-1} , which could be attributed to the decay of Cs^*He_2 from the electronic $\text{A}\Pi_{1/2}$ state. This line was observed following D_1 -excitation.

Another part of the present work is the study of multi-photon processes in the magnetic resonance spectra in the ground state of cesium atoms trapped in solid helium. The experimental technique used in these experiments as in the tomography experiments is optically-detected magnetic resonance. In this technique resonant circularly polarized laser light is used both to spin polarize the sample and to detect magnetic resonance transitions. Multi-photon transitions, i.e. processes in which several radio-frequency photons are absorbed simultaneously in the magnetic resonance transition, were in the focus of interest. These processes become observable when the magnetic sublevels are split by the quadratic Zeeman effect. The long relaxation times of spin coherences of Cs in solid He allowed us to spectrally resolve such transitions in fields as low as 1 mT. We have observed all allowed multi-photon transitions up to the $\Delta M = 8$ transition in the $F = 4$ -state. Multi-photon transitions can find applications in magnetometry, in the suppression of systematic effects in edm experiments and may further allow one to study relaxation phenomena in doped He crystals. The demonstration of this latter feature is still hindered by inhomogeneous line broadening. We compare our experimental spectra with theoretical spectra obtained from numerical solutions of the Liouville equation including optical pumping and the interaction with the static and oscillating fields. The experimental spectra are very well described when allowing in the calculations for a magnetic field inhomogeneity of $2 \cdot 10^{-5}$.

We have also performed a theoretical study of the influence of stochastic perturbations of given multipole orders on the various multi-photon coherences. Algebraic and numerical results for perturbations of both dipolar and quadrupolar symmetry were obtained, which may in future help to identify the mechanism governing spin relaxation in helium crystals.

The original idea behind the study of alkali doped helium crystals, pursued in our group since almost a decade, is to design a novel technique to search for a permanent electric dipole moment (edm) of cesium. The existence of such an edm would be a direct proof of a violation of time reversal symmetry (T-violation) in an atomic system. Edm experiments search for a linear Stark shift of a very narrow magnetic resonance line. The necessary experimental conditions of long spin relaxation times and the possibility to apply high electric fields are both fulfilled by atoms trapped in helium crystals. A setup for performing magnetic resonance experiments in the presence of strong electric fields is shortly presented in the work. Electric fields up to 30 kV/cm could be applied in our samples. Because of technical problems Stark effect studies has not led to conclusive results yet.

Zusammenfassung

Die vorliegende Arbeit enthält die Ergebnisse meiner Forschungsarbeit an der Universität Bonn und an der Universität Fribourg (Schweiz). Sie beinhaltet zwei Teile, entsprechend den unterschiedlichen Themen, die ich an diesen Orten behandelt habe. In Bonn arbeitete ich an optischer Magnetresonanztomographie von Atomen in der Gasphase, während ich mich in Fribourg der Untersuchung von in festen Heliumkristallen eingeschlossenen Fremdatomen widmete. Die Resultate sind in Form von fünf Veröffentlichungen dargestellt: zwei publizierte, zwei zur Publikation akzeptierte und ein im Prozess der Einreichung befindlicher Artikel.

Bei der im ersten Teil behandelten optischen Magnetresonanztomographie handelt es sich um eine neuartige Technik, die die zweidimensionale Bildgebung der Bewegung spin-polarisierter Alkaliatome erlaubt. Sie unterscheidet sich von konventioneller Magnetresonanztomographie durch ihre optische Präparation und ihren optischen Nachweis von Spinpolarisation. Wir haben diese Technik angewandt, um Diffusionsprozesse von Cäsiumatomen in Neongas zu studieren, dabei bestimmten wir die Diffusionskonstante dieses Systems zu $0.20(1) \text{ cm}^2/\text{s}$ unter Standardbedingungen.

Der zweite Teil und zugleich Hauptteil dieser Arbeit befasst sich mit den optischen und magneto-optischen Eigenschaften von in festem He^4 eingeschlossenen Cäsiumatomen. Die Experimente wurden in der kubisch-raumzentrierten (bcc) oder in der hexagonal-dichtgepackten (hcp) Phase von festem Helium durchgeführt. Matrixisolierte Cäsiumatome befinden sich in einer blasen-ähnlichen Kavität sphärischer Form, wenn sich das Atom in seinem radial symmetrischen $6S_{1/2}$ -Grundzustand befindet. Die sphärische Symmetrie und die gänzlich unmagnetischen Eigenschaften von Helium erklären die ungewöhnlich langen Spinrelaxationszeiten ($\approx 1\text{s}$), die in der bcc Phase beobachtet wurden. Im Gegensatz dazu sind in der hcp Phase gemessenen Magnetresonanzlinien signifikant breiter (um drei Größenordnungen) und sie zeigen eine komplexe Unterstruktur bedingt durch eine kleine Deformation der Blasenform.

Ein in der Literatur viel diskutiertes Problem ist die Fluoreszenz von Alkaliatomen in kondensiertem Helium: Während die schweren Alkalis Rb und Cs Fluoreszenz emittieren, konnte keine Fluoreszenz von den leichteren Alkalis beobachtet werden. Es wurde allgemein angenommen, dass die Emission beeinträchtigt ist durch die Bildung von Exciplex-Molekülen, d.h. von gebundenen Zuständen angeregter Alkaliatome mit einem oder mehreren Heliumatomen. Weiter wurde angenommen, dass für Helium solche Exciplexe nicht existieren. In dieser Arbeit haben wir unsere Forschung auf die Untersuchung von atomarer D_2 -Anregung und der genauen Analyse der darauf folgenden Abregung des $6P_{3/2}$ -Zustands ausgeweitet. Direkte D_2 -Emission war bisher nicht beobachtet worden. Man detektierte lediglich eine schwache D_1 -Emission nach erfolgter D_2 -Anregung, welche auf einen Zerfallskanal zum $6P_{1/2}$ -Zustand hinweist. Durch die Ausweitung des Wellenlängenbereichs unseres Detektionssystems konnten wir nun zwei neue, breite Linien starker Intensität bei 7130 cm^{-1} und 10520 cm^{-1} nachweisen. Die energetisch höher liegende Linie war kürzlich auch in kaltem Heliumdampf und in flüssigem He II von einer in Kyoto ansässigen Forschungsgruppe beobachtet worden. Der Ursprung dieser Linie liess sich dem Zerfall von $\text{Cs}(\text{AI}_{3/2})\text{He}_2$ -Exciplexen zuordnen. Die zweite Linie war vorher nicht beobachtet worden und ist möglicherweise nur in festen Helium nachzuweisen. Um die neuen Linien zuordnen zu können, führten wir Modellrechnungen der Emissionsspektren von zerfallen-

den Cs^*He_n -Exciplexen durch. Durch Vergleich mit den experimentellen Daten bestätigte sich die Zuordnung der Cs^*He_2 -Linie. Die energetisch niedriger liegende Linie ist durch den Zerfall eines anderen Exciplexes verursacht. Unsere Berechnungen legen nahe, dass es sich bei der Struktur um ein angeregtes Cäsiumatom mit hantelförmiger Elektronenkonfiguration handelt, um dessen Taille sich ein Ring von n Heliumatomen befindet. Die genaue Zahl der n gebundenen Heliumatome liess sich aufgrund mangelnder Modellgenauigkeit bisher nicht bestimmen. Jedoch scheint Cs^*He_6 der wahrscheinlichste Kandidat zu sein. Cs^*He_n -Exciplexe mit $n > 2$ waren zuvor nicht beobachtet worden. Dies schien die in der Literatur zu findenden Aussagen zu bestätigen, dass solche Komplexe nicht stabil seien.

Schliesslich konnten wir nach D_1 -Anregung eine dritte, sehr schwache Linie bei 10160 cm^{-1} nachweisen, welche sich dem Zerfall von $\text{Cs}(\text{AII}_{1/2})\text{He}_2$ zuordnen lässt.

Ein weiteres Thema der vorliegenden Arbeit ist die Untersuchung von Multi-Photonen-Prozessen in den Zeeman-Struktur des Grundzustandes von Cäsium in festem Helium. Die benutzte experimentelle Technik ist, wie im Tomographie-Experiment, die optisch-detektierte Magnetresonanz (ODMR). In dieser wird zirkular polarisiertes Laserlicht sowohl zur Präparation von Spinpolarisation als auch zum Nachweis von Magnetresonanzübergängen benutzt. Die betrachteten Multi-Photonen-Übergänge sind Prozesse, in denen mehrere Photonen gleichzeitig bei Magnetresonanzübergängen beteiligt sind. Sie werden nachweisbar, wenn die magnetischen Unterzustände durch den quadratischen Zeeman-Effekt aufgespalten sind. Die langen Spinrelaxationszeiten von Cs in festem Helium erlauben uns, diese Übergänge auch bei kleinen magnetischen Feldern (1 mT) auflösen zu können. Wir beobachteten alle erlaubten Multi-Photonen-Übergänge bis zum 8-Photonenübergang im $F = 4$ Hyperfeinmultiplet. Multi-Photonen-Übergänge können in der Magnetometrie, in der Unterdrückung systematischer Effekte in EDM-Experimenten Anwendung finden und sie mögen darüberhinaus zur Identifikation von Relaxationsprozessen in dotierten Heliumkristallen dienen. Die Demonstration des letzteren ist jedoch zur Zeit noch durch inhomogene Linienverbreitungen verhindert. Wir verglichen unsere experimentellen Spektren mit theoretischen, die wir aus der numerischen Lösung der Liouville-Gleichung unter Berücksichtigung des optischen Pumpens und der Wechselwirkung mit dem statischen und dem oszillierenden Feld erhalten haben. Die experimentellen Daten sind sehr gut wiedergegeben, wenn magnetische Feldinhomogenitäten von $2 \cdot 10^{-5}$ angenommen werden. Zusätzlich haben wir theoretische Studien des Einflusses stochastischer Störungen definierter Multipolordnung auf die Multi-Photon-Kohärenzen durchgeführt. Es wurden algebraische sowie numerische Resultate für dipolare und quadrupolare Störungen erzielt, welche in Zukunft helfen können, den Spinrelaxationsmechanismus in Heliumkristallen zu identifizieren.

Das ursprüngliche und weiterhin verfolgte Ziel des Heliumexperiments ist der Nachweis eines permanenten elektrischen Dipolmoments (EDM) von Cäsium. Dieser Nachweis wäre ein direkter Beleg für Zeitumkehrverletzung in einem atomaren System. EDM-Experimente suchen nach einer linearen Stark-Verschiebung schmalbandiger Magnetresonanzlinien. Die notwendige experimentelle Voraussetzung langer Spinrelaxationszeiten sowie die Möglichkeit hohe elektrische Felder anlegen zu können, sind in unserem Experiment gegeben. Es wird kurz ein Aufbau zur Durchführung von Magnetresonanzexperimenten bei gleichzeitig angelegten hohen elektrischen Feldern demonstriert. Elektrische Felder von bis zu 30 kV/cm konnten bisher angelegt werden. Technische Probleme verhinderten jedoch bisher aussagekräftige Stark-Effekt-Messungen.

Contents

Preface	1
I Optical magnetic resonance tomography	3
1 Diffusion of Cs atoms in Ne buffer gas measured by optical magnetic resonance tomography	5
1.1 Introduction	5
1.2 Experiment	6
1.3 Discussion	8
1.4 Conclusion and outlook	11
II Laser spectroscopy of cesium atoms trapped in solid helium	15
2 Introduction	17
2.1 Historical overview	17
2.2 Solid He ⁴	18
2.2.1 Phase diagram of ⁴ He	18
2.2.2 Structure of the bcc and hcp phases	18
2.2.3 He-He interaction	19
2.2.4 Optical properties	19
2.3 Setup and implantation technique	20
2.4 The optical properties of Cs atoms in solid helium: The spherical bubble model .	21
2.5 Optical Pumping	23
2.6 Optically detected magnetic resonance (ODMR)	24
3 Observation of apple- and dumbbell-shaped Cs*He_n exciplexes in solid He⁴	29
3.1 Introduction	29
3.2 Theoretical calculation of the emission spectra	31
3.2.1 Cs*-He _n exciplex potentials	31
3.2.2 Vibrational structure of the Cs*He _n exciplexes	35
3.2.3 The emission spectra	37
3.3 Experiment	38
3.3.1 Experimental setup	38
3.3.2 Observed emission spectra	39

3.3.3	Pressure dependence of the Cs ($6\Pi_{3/2}$)He ₂ emission line	41
3.4	Discussion	42
3.4.1	Cs*He ₂	42
3.4.2	Cs*He _{<i>n_{max}</i>}	44
3.4.3	Formation of Cs*He _{<i>n_{max}</i>} in solid helium	45
3.5	Summary and outlook	46
4	Multiphoton processes in the Zeeman structure of atomic Cs trapped in solid helium	49
4.1	Introduction	49
4.1.1	Akali-doped helium crystals	50
4.1.2	Multi-photon transitions	50
4.2	Multi-photon transitions	51
4.2.1	Basics	51
4.2.2	Resonance frequencies in the ground state of ¹³³ Cs trapped in the b.c.c. phase of solid ⁴ He	53
4.2.3	Optical Detection	54
4.2.4	Numerical calculations	54
4.3	Experiment	55
4.3.1	The experimental set-up	55
4.3.2	Experimental results	55
4.3.3	Comparison with calculations	57
4.4	Use of multi-photon transitions	61
4.5	Summary	63
5	Relaxation mechanisms of multi-quantum coherences in the Zeeman structure of atomic Cs trapped in solid He	67
5.1	Introduction	68
5.2	Simple theory of multi-photon transitions	69
5.2.1	Multi-photon transition between substates of a hyperfine level <i>F</i> in a magnetic field	69
5.2.2	Lineshapes of multi-quantum transitions	70
5.3	Numerical Calculation of the ODMR signal	71
5.3.1	Optically detected magnetic resonance	71
5.3.2	Magnetic interaction	72
5.3.3	Optical pumping and detection signal	73
5.3.4	Relaxation	74
5.3.5	Relaxation of multi-quantum coherences	76
5.3.6	Gain in spectroscopic sensitivity	77
5.3.7	Technical details of the calculations	79
5.4	Experiment	79
5.4.1	Experimental setup and data recording	79
5.4.2	Experimental results	80
5.4.3	Comparison with the calculations	82

5.5	Effect of intrinsic multipole relaxations on the multi-photon spectra	85
5.6	Summary and outlook	86
5.7	Appendix: Ground state master equation for optical pumping	89
6	Magnetic and electric properties of alkali atoms in solid helium	93
6.1	Introduction	93
6.2	Setup	94
6.3	The phase stabilized magnetometer	95
	Danksagung	99
	Curriculum vitae	101

Preface

This thesis is based on research carried out at the *Institut für Angewandte Physik der Universität Bonn, Germany* and at the *Departement für Physik der Universität Freiburg, Switzerland*. It is divided into two parts: The first part is devoted to the motion of alkali vapor atoms studied by optical magnetic resonance tomography. This research was a continuation of my diploma thesis, during which Guido Hinz and myself built up an experimental apparatus for optical magnetic resonance tomography. In the first year of my PhD student time Dominik Giel and myself then studied diffusion processes of spin polarized cesium atoms in Neon buffer gas by means of this novel technique. The one and only chapter of this part consists of an article presenting the results of our work.

The second and main part of this thesis deals with laser spectroscopy of cesium atoms trapped in solid helium. An introducing chapter is followed by four chapters, which present some of our research on this topic. These four chapters consist of independent articles written during this thesis. Consequently, each chapter can be read as an independent text, which includes an introduction, a description of the experiment, results, a discussion and the references of the article.

The articles included in this thesis are:

1. D. Giel, G.Hinz, D. Nettels, and A. Weis. Diffusion of Cs atoms in Ne buffer gas measured by optical magnetic resonance tomography. *Opt. Express*, 6(13):251, 2000.
2. D. Nettels, R. Müller-Siebert, X. Huang, S. Ulzega, and A. Weis. Magnetic and electric properties of alkali atoms in solid helium. *Physica B*, 329:406, 2003.
3. D. Nettels, R. Müller-Siebert, Simone Ulzega, and Antoine Weis. Multiphoton processes in the Zeeman structure of atomic Cs trapped in solid helium. (Accepted for publication by Appl. Phys. B.)
4. D. Nettels, R. Müller-Siebert, and Antoine Weis. Relaxation mechanisms of multi-quantum coherences in the Zeeman structure of atomic Cs trapped in solid He. (Invited paper. Accepted for publication by Appl. Phys. B.)
5. D. Nettels, A. Hofer, P. Moroshkin, R. Müller-Siebert, Simone Ulzega, and Antoine Weis. Observation of apple- and dumbbell-shaped Cs*He_n exciplexes in solid He⁴. (To be submitted.)

Part I

Optical magnetic resonance tomography

Chapter 1

Diffusion of Cs atoms in Ne buffer gas measured by optical magnetic resonance tomography

D. Giel,² G. Hinz,² D. Nettels,^{1,2} and A. Weis^{1,2} ¹*Institut de Physique, Université de Fribourg, Chemin de Musée 3, CH-1700 Fribourg, Switzerland*
²*Institut für Angewandte Physik, Universität Bonn, Wegelerstr. 8, D-53115 Bonn, Germany*

published in Opt. Express **6** (13), 251 (2000)

Abstract: Optical magnetic resonance tomography uses optical pumping and the paramagnetic Faraday effect to image spin density distributions in optically thin media. In this paper we present an apparatus that allows to measure the distribution of spin-polarized Cs atoms, which we applied to study the diffusion of Cs in Ne buffer gas by time-resolved 2D-mapping of the evolution of an initial inhomogeneous spin distribution. The diffusion constant D_0 for Cs in a Ne buffer gas of 1013 mbar is determined as $0.20(1) \text{ cm}^2/\text{s}$.

1.1 Introduction

Nuclear magnetic resonance tomography is a well-known technique that allows the mapping of spin-densities, relaxation times and flow velocities in dense media by measuring the precession frequencies of nuclear magnetic moments in inhomogeneous magnetic fields. It is best known for its spectacular success in medical science. *Optical Magnetic Resonance Tomography* (OMRT) is a related technique which detects the precessing electronic magnetic moments of paramagnetic atoms manipulated through the interaction with light [1, 3, 4]. Besides producing a macroscopic polarization by optical pumping, light is also used to monitor the precession of the electron spins. In this work we have applied OMRT to study the diffusional motion of spin-polarized cesium atoms in neon buffer gas. In contrast to conventional techniques where low temperatures and/or high magnetic fields are needed to produce (small) population differences of the nuclear magnetic sublevels, optical pumping of cesium vapor with resonant laser radiation may yield population inversions close to 100%. Moreover, the precessing magnetization is detected via the

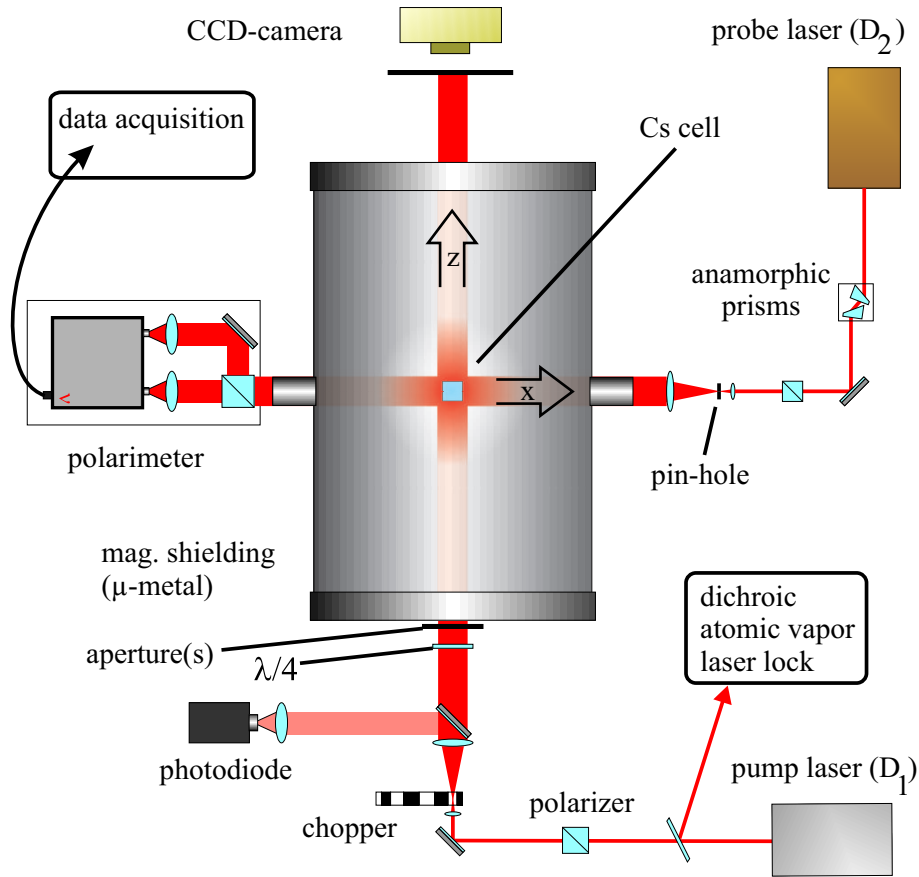


Figure 1.1: Experimental setup.

rotation of the polarization vector (paramagnetic rotation) of a near-resonant linearly polarized probe laser beam which traverses the medium perpendicular to the pumping radiation. To get information about the spatial spin distribution a small magnetic field gradient is superposed to the main magnetic field thus encoding the spatial spin distribution into a distribution of Larmor frequencies. Projection reconstruction is used to reconstruct the initial spin density distribution from frequency spectra obtained in gradients with different orientations. The diffusional motion can be monitored by varying the time interval between the spin preparation and the imaging process.

1.2 Experiment

The experiments were performed in a cubic quartz cell of 1 cm^3 filled with Ne buffer gas ($p=135$ mbar) and condensed Cs (Fig. 1.1). The cell is located in the center of a solenoid used to apply the main field and two saddle coil pairs as well as one anti-Helmholtz coil pair for the generation of the field gradients. Radio-frequency is applied by a pair of Helmholtz coils. The cell and all coils are surrounded by a 1.5 mm thick cylindrical μ -metal shield ($\varnothing=36$ cm, $l=60$ cm) to reduce stray fields. Optical pumping is done with the beam from a diode laser whose frequency is locked to the $F=4$ component of the Cs D_1 -line at 894 nm using a *dichroic atomic vapor lock* [5]. The pumping beam - expanded by means of a telescope - passes through a polarizer and a $\lambda/4$ -plate and finally traverses the cell parallel to the main magnetic field. The inhomogeneity and position of the beam are controlled by monitoring the light scattered from a screen by means

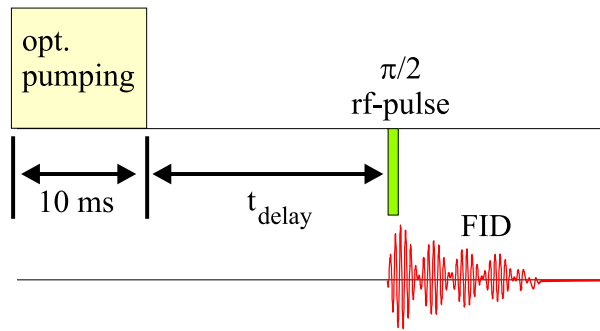


Figure 1.2: Timing sequence of the experiment.

of a CCD camera. The beam is chopped mechanically with a period of 20 ms.

After the pumping beam is blocked by the chopper the longitudinal magnetization M_z is transferred into a transverse magnetization $M_+ = M_x + iM_y$ by a radio-frequency $\pi/2$ -pulse, after which the transverse polarization starts to precess in the static field B_0 , producing a free induction decay (FID) of M_+ .

A second - free running - diode laser produces the linearly polarized probe beam which, after expansion to a diameter of 1.5 cm, intersects the pump beam at right angles within the cell. The probe laser is current-tuned to the frequency of maximum dispersion of the D_2 transition without any active stabilization. The power of the probe beam is less than $100 \mu\text{W}$ in order to minimize disturbing effects due to absorption of the probe beam. The paramagnetic rotation of the light polarization produced by the vapor magnetization is detected using an 'autobalanced' photodetector (New Focus, model Nirvana) and a polarizing beamsplitter cube orientated at 45° with respect to the incident polarization. The coherent transient signal (FID) is observed as the difference of the photocurrents of two photodiodes at the output ports of the polarizer.

In order to synchronize the radio-frequency pulses (provided by a waveform generator), the strength and orientation of the gradients and the detection of the FID (recorded by an ADC plug-in module), all devices are triggered by a multi-channel pulse generator and controlled by a personal computer. The pulse generator itself is triggered by the mechanical shutter.

After a delay time t_{delay} following the optical pumping pulse the imaging process is started through the application of the $\pi/2$ -rf-pulse (Fig.1.2). Gradient fields are switched on at the same time to encode the spin density. The FID is recorded and stored on hard disk for off-line processing. A single tomographic snapshot of the diffusion process is taken by recording 40 FID's with gradients of identical magnitude and different orientations in a plane perpendicular to \hat{B}_0 . A *projection reconstruction* (PR) algorithm is used to reconstruct the 2-dimensional spin density distribution [6]. For the tomography of our diffusion-limited gaseous Cs sample the PR algorithm is more suitable than a *Fourier imaging* algorithm.

The space-time evolution of the magnetization can be calculated by solving the diffusion equation including relaxation for the magnetization $M_z(\vec{x})$

$$\frac{\partial M_z}{\partial t} = D\nabla^2 M_z - K \cdot M_z \quad (1.1)$$

for a given initial distribution of magnetization. K is the rate of homogeneous depolarization due to collisions with buffer gas atoms and residual absorption of the probe beam. D is the diffusion constant at the actual buffer gas density. As collisions with the cell walls destroy the polarization, the boundary conditions of Eq. (1.1) are simply that the magnetization M_z vanishes at the cell walls. The solutions of Eq. (1.1) for a cubic cell can hence be expanded in terms of cosine functions with a spatial periodicity of $n_i \cdot \frac{a}{2}$ where a is the cell dimension and n_i are integers:

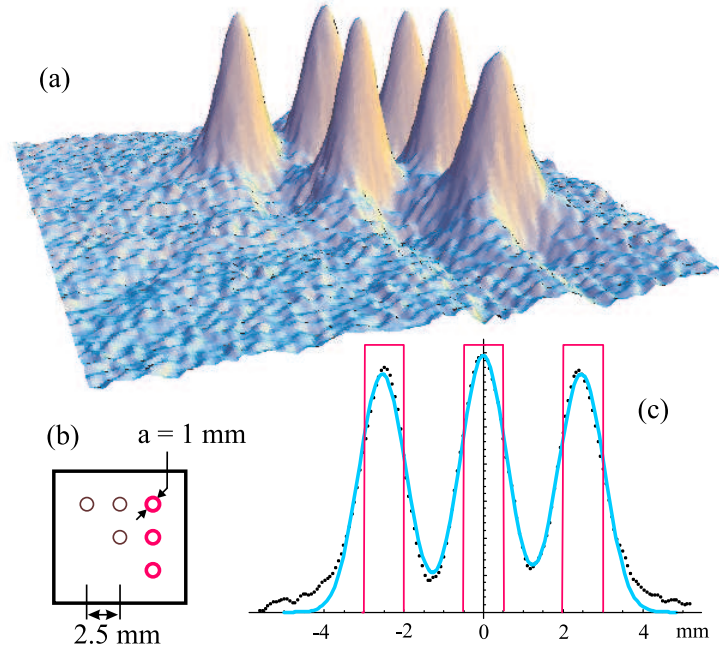


Figure 1.3: Tomographic picture (a) of an inhomogeneous polarization produced by a mask (b) inside the pump beam. (c) is a cut through distribution showing the Gaussian shapes (blue line) resulting from the diffusion of an initial cylindrical distribution (rectangles).

$$M_z = \sum_{l,m,n=1}^{\infty} c_{l,m,n} \cos(l\pi \frac{x}{a}) \cos(m\pi \frac{y}{a}) \cos(n\pi \frac{z}{a}) e^{-(\gamma_{l,m,n}+K)t} \quad (1.2)$$

These functions are commonly referred to as *diffusion modes*. Each three-dimensional mode is labeled by a triplet (l, m, n) of integers and decays exponentially with a time constant

$$T_{l,m,n} = 1/\gamma_{l,m,n} = \frac{a^2}{\pi \cdot D \cdot (l^2 + m^2 + n^2)}. \quad (1.3)$$

In order to simulate the diffusion process we expand the measured initial spin distribution into cubic diffusion modes. As the time development of each mode is known, this allows to compare measured and calculated distributions at later times and to determine the diffusion constant D . We determined the spatial resolution of the imaging process and calibrated the magnitude of the gradient fields by recording the magnetization generated by pumping the cell through a calibration mask inserted into the pump beam. Fig. 1.3 shows an example where the mask consisted of six circular apertures ($\varnothing=1 \text{ mm}$, 2.5 mm separation). The tomographic image of the created polarization pattern is amplitude coded. Each initial cylindrically shaped distribution of the magnetization is convoluted with a Gaussian distribution due to diffusion during the FID. From the widths of the peaks we determined the experimental resolution to be $360(20) \mu\text{m}$.

1.3 Discussion

In order to measure the diffusion of the spin polarized cesium atoms within the cell, we first prepare a spatially inhomogeneous distribution of spin polarization using a masking aperture of approximately 2 mm clear diameter centered in the pump beam. Stroboscopic pictures of the diffusion process are obtained by varying t_{delay} in steps of 0.5 ms from 0 to 10 ms after the

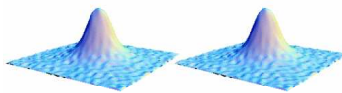


Figure 1.4: Experimental (left) and simulated (right) evolutions of a given initial experimental magnetization distribution (Animation, 1.1 MB). The frames are separated by $\Delta t_{\text{delay}}=0.5$ ms.

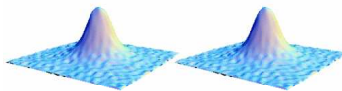


Figure 1.5: The same as Fig. 1.4 but with the distributions at each step of t_{delay} normalized to the same peak height to demonstrate the change of shape due to diffusion. (Animation, 1.4 MB)

pump pulse. The animation linked to Fig. 1.4 (left side) shows the measured evolution in a cell with a buffer gas pressure of 135 mbar. Cuts through the distribution are shown in Fig. 1.6. According to the model outlined above the higher order diffusion modes vanish quickly until only the lowest order mode remains visible; the distribution evolves from an initial Gaussian-shaped distribution to a pure cosine-shaped distribution (lowest order diffusion mode).

In order to extract a quantitative value of the diffusion coefficient D from the measured distributions we proceeded as follows: We first determined the width Δx_{FWHM} of each measured distribution. The results are shown as dots in Fig. 1.7. For an open cell (no boundaries) one would expect Δx_{FWHM} to vary according to

$$\Delta x_{\text{FWHM}}^2 = 2Dt. \quad (1.4)$$

The deviation of the experimental results from this simple law is due to the cell boundaries i.e. to the rapid damping of the higher order diffusion modes. We simulated the actual experimental situation by decomposing numerically the distribution at $t_{\text{delay}}=0$ into diffusion modes (Eq. (1.2)), calculating the relaxation of each mode according to Eq. (1.3), reassembling the relaxed modes and finally determining the widths of the relaxed distributions. The values thus obtained are shown as curved line in Fig. 1.7. Adjustment of the calculated widths was done by a χ^2 -minimizing procedure that varied the parameter D . Note that one of the main advantages of our method is the fact that the determination of x_{FWHM} depends only on D and is independent of K . We obtained a minimal χ^2 value for $D=1.73(4)$ cm^2/s from data recorded at $T=51(2)$ $^\circ\text{C}$. The straight line in Fig. 1.7 is given by Eq. (1.4) with this optimal value of D . The animations on the right hand sides of Figs. (1.4,1.5) show the simulated distributions after the fitting procedure.

It is customary to scale the diffusion constant D_0 to standard pressure ($p_0=1013$ mbar) and temperature ($T_0=20^\circ\text{C}$) via the relation

$$D = D_0 \frac{p_0}{p} \left(\frac{T}{T_0} \right)^{3/2}. \quad (1.5)$$

We determined the Ne buffer gas pressure p in our cell in an auxiliary experiment by measuring the pressure shift of the $F=3, M=0 \rightarrow F=4, M=0$ hyperfine clock transition of the ground state in an optical-microwave double resonance experiment. A small magnetic field ($5 \mu\text{T}$) was applied in order to lift the Zeeman degeneracy of the ground state sublevels and to isolate the 0-0 transition. The transition-frequency was found to be shifted by $62.0(2)$ kHz with respect to the clock frequency of 9.19263177 GHz. From the pressure shift measurements described in [8] we conclude that the buffer gas pressure in our cell at $T=51(2)$ $^\circ\text{C}$ is $p=135(5)$ mbar. This gives

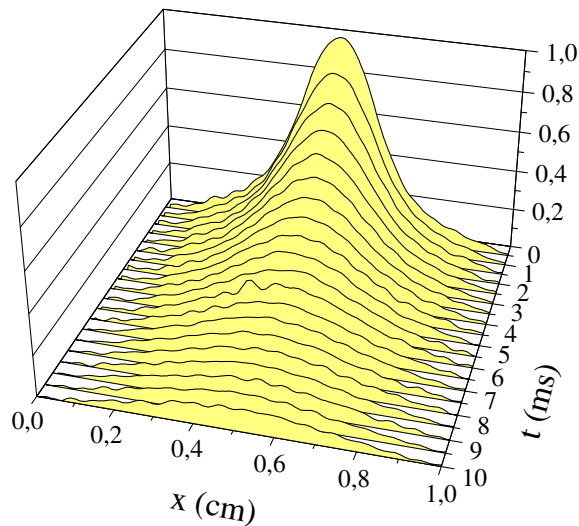


Figure 1.6: Time Evolution of cuts through the spin density distribution

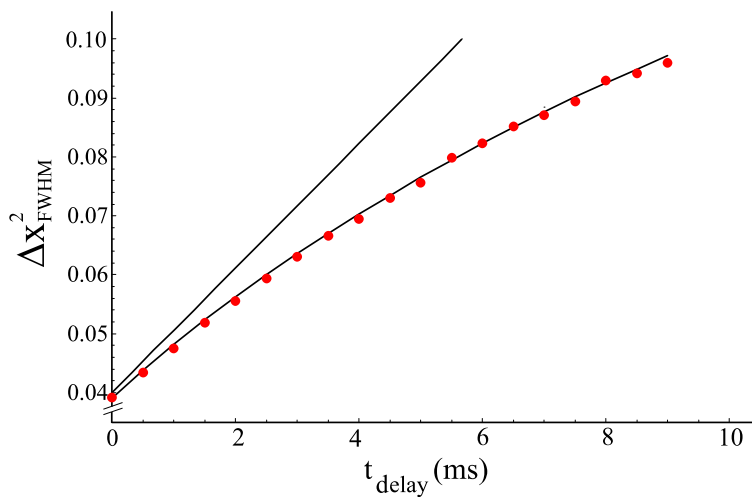


Figure 1.7: Time evolution of the widths Δx_{FWHM} of the magnetization distributions (dots). Solid line: Solution Eq. (1.1) with $D=1.73 \text{ cm}^2/\text{s}$. Straight line: Theoretical evolution without boundaries ('open' cell), $\Delta x_{\text{FWHM}}^2 = 2Dt$.

a reduced diffusion coefficient of

$$D_0 = 0.20(1)\text{cm}^2/\text{s}. \quad (1.6)$$

The literature shows a broad range of experimental values for the diffusion constant of cesium in neon buffer gas, ranging from $0.40\text{ cm}^2/\text{s}$ down to $D_0=0.10\text{ cm}^2/\text{s}$ (Measured values up to 1989 are tabulated in [9]). In most of these experiments, the diffusion constant is deduced from the measurement of the longitudinal relaxation time T_1 as a function of buffer gas pressure. Diffusion to the walls as well as depolarizing collisions cause the magnetization to vanish. In the analysis of this integral measurement there is a strong correlation between the parameters describing the diffusion and the depolarization and even small (depolarizing) admixtures of paramagnetic impurities to the buffer gas can influence the inferred diffusion constants significantly. The direct space- and time-resolved measurement of the diffusion constant in our experiment is not affected by depolarization processes due to impurities or depolarizing scattering of probe laser radiation.

1.4 Conclusion and outlook

We have developed a novel technique for the quantitative measurement of the diffusion constant of spin polarized alkali atoms in a noble gas. The technique allows to determine the diffusion constant D of Cs in Ne with a precision of 2%, while the reduced diffusion constant D_0 could be determined with precision of 4% only, due to the uncertainty of the buffer gas pressure. Compared to previously used techniques our method is insensitive to uncertainties in the relaxation times. Moreover the diffusion constant D - of dimension $(\text{length})^2/\text{time}$ - is easily calibrated, the length scale being determined by a calibrating mask and the time scale being given by the delay generating synthesizer used. In the future we plan to apply the technique presented here to samples of Cs atoms embedded in crystalline ^4He matrices [10] in order to study their spatial distribution. The strongly suppressed diffusion in these samples and the very long coherence times $T_2 > 300\text{ ms}$ should allow to achieve spatial resolutions in the micron range.

References

- [1] D. Nettels, “Optische Magnetresonanztomographie an spinpolarisiertem Cäsiumdampf,” Dipl. thesis Univ. Bonn (unpublished)(1998).
- [2] D. Giel, “Darstellung der Diffusion atomarer Spinpolarisation mit optischer Magnetresonanztomographie,” Dipl. thesis Univ. Bonn (unpublished)(2000).
- [3] J. Skalla, G. Wäckerle, M. Mehring and A. Pines, “Optical magnetic resonance imaging of vapor in low magnetic fields,” *Phys. Lett. A* **226**, 69-74 (1997).
- [4] K. Ishikawa et al., “Optical magnetic resonance imaging of laser-polarized Cs atoms,” *J. Opt. Soc Am. Bull.* **16**, 31-37 (1999).
- [5] K. L. Corwin, Z. T. Lu, C. F. Hand, R. J. Epstein and C. E. Wieman, “Frequency-stabilized diode laser with Zeeman shift in an atomic vapor,” *Appl. Opt.* **37**, 3295 (1998).
- [6] P. T. Callaghan, *Principles of Nuclear Magnetic Resonance Microscopy* (Oxford University Press, Oxford, 1991).
- [7] A. Corney, *Atomic and Laser Spectroscopy* (Oxford University Press, Oxford, 1977).
- [8] N. Beverini, F. Strumia and G. Rovera, “Buffer gas pressure shift in the $m_F=0 \rightarrow m_F=0$ ground state hyperfine line in Cs,” *Opt. Commun.* **37,6**, 394 (1981).
- [9] J. Vanier, C. Audoin, *The Quantum Physics of Atomic Frequency Standards* (Bristol, Hilger, 1989).
- [10] S. I. Karnorsky and A. Weis, “Optical and magneto-optical spectroscopy of point defects in condensed helium,” *Advances in Atomic, Molecular and Optical Physics*, **38**, 87 (1998).

Part II

Laser spectroscopy of cesium atoms trapped in solid helium

Chapter 2

Introduction

2.1 Historical overview

In 1991 S. Kanorsky and A. Weis proposed to search for a permanent electric dipole moment (edm) of atoms by using a sample of matrix-isolated paramagnetic atoms in superfluid helium. Because of the purely diamagnetic nature of helium, long electronic spin relaxation times of the sample atoms were expected. It was further known that condensed helium has an electric break-down voltage exceeding 100 kV/cm. These two characteristic properties were believed to allow for a competitive sensitivity compared to existing edm-experiments [1, 2]. In the following year first studies were made with Ba, Au and Cu atoms in superfluid helium by the group of A. Weis at the Max-Planck-Institut für Quantenoptik (MPQ) in the laboratory of T. W. Hänsch [1]. The atoms were sputtered by means of laser ablation from a solid target and detected by their laser-induced fluorescence. The pressure shift and broadening of the excitation and emission lines of barium in liquid helium were measured and quantitatively interpreted in the frame of the so-called spherical bubble model [3].

In 1993 atoms were implanted for the first time into solid helium by using the same laser-ablation technique [4, 5]. In the following years it was demonstrated that cesium atoms trapped in the bcc phase of solid helium can effectively be spin-polarized by means of optical pumping. Very long longitudinal spin relaxation times of 1 s were observed [6]. After the reduction of magnetic field inhomogeneities at the sample location magnetic resonance lines of less than 20 Hz width were obtained, allowing for a magnetometric sensitivity of $2.6 \text{ pT}/\sqrt{\text{Hz}}$ [7]. With these promising first results important steps toward an edm experiment were achieved.

In parallel it was realized that, besides the long-term objective of measuring an edm, helium crystals doped with foreign atoms were a unique system opening a research field for its own. Changes of various atomic properties induced by the weak electromagnetic interaction with the surrounding helium were observed and asked for explanations. Especially the different atomic properties measured in the bcc phase and in the hcp phase are until today in the main focus of interest. Such differences can be observed on optical [8], hyperfine [9] as well as in ground state Zeeman transitions [10]. Furthermore the optical pumping process for producing the spin polarization was studied in detail [11]

An important step towards an edm experiment was the simultaneous detection of Rb and Cs, which demonstrated the useability of rubidium as a co-magnetometer in edm experiments [12].

In the last five years our work concentrated on improving the magnetometric sensitivity and the general stability of the experimental setup. The detection system was renewed. An active temperature stabilization was installed. A suitable non-magnetic sealing technique, allowing the leakproof flanging of windows onto the helium crystal containing pressure cell was developed.

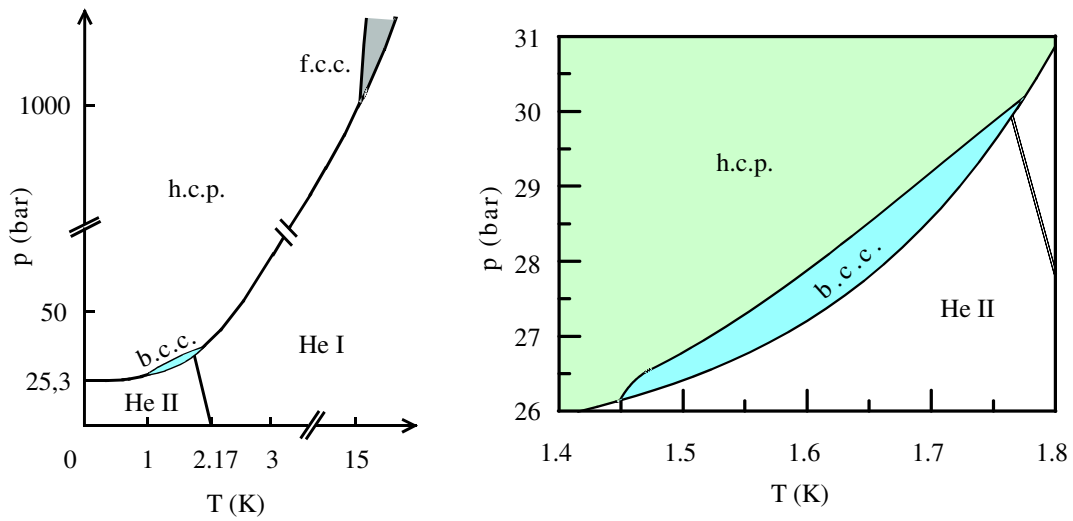


Figure 2.1: Phase diagrams of ${}^4\text{He}$. The right diagram represents the p - T region relevant for the experiment.

Magnetic field shields as well as superconductive magnetic field coils operating in persisting mode were constructed. Most of these and other improvements are described in [13]. Also a setup for applying strong electric fields inside the pressure cell was developed [9, 13, 14], which allows us the application of up to 30 kV/cm.

2.2 Solid He^4

2.2.1 Phase diagram of ${}^4\text{He}$

Fig. 2.1 shows the phase diagram of condensed helium. At saturated vapor pressure (svp) liquid helium remains superfluid down to the lowest temperatures. This unique feature is due to the weakness of the interatomic van der Waals attraction, which is comparable to the zero-point energy of the helium atoms. Owing to its light mass, helium has a large thermal de Broglie wavelength $\lambda_T = (h^2/2\pi mkT)$ at low temperatures ($\lambda_T = 8 \text{ \AA}$ at 1.6 K). Thus helium atoms can be localized well enough for forming a solid under pressure only.

Above 25 bar the (p - T)-diagram is dominated by a solid hexagonal close-packed (hcp) phase. Starting from 1000 bar there exists a face-centered cubic (fcc) phase. Between $T = 1.45$ - 1.78 K and $p = 26$ - 30 bar exists a small island in the phase diagram, where ${}^4\text{He}$ crystalize in body-centered cubic (bcc) phase. One distinguishes two liquid phases: the normal fluid component (He I) and the superfluid component (He II). The p - T region relevant for this experiment is shown in the right part of Fig. 2.1.

2.2.2 Structure of the bcc and hcp phases

As mentioned earlier the atomic properties of the impurity atom trapped to solid helium depend on the symmetry of the crystal structure. The primitive cells of the bcc and the hcp phase of solid He^4 are illustrated in Fig. 2.2. The bcc phase is isotropic whereas the hcp phase is of axial symmetry. The lattice constants were determined by means of inelastic-neutron scattering [15, 16]. The ratio $c/a = 1.638$ is very close to the value $c/a = \sqrt{8/3} = 1.633$ of an ideal hcp crystal of hard spheres.

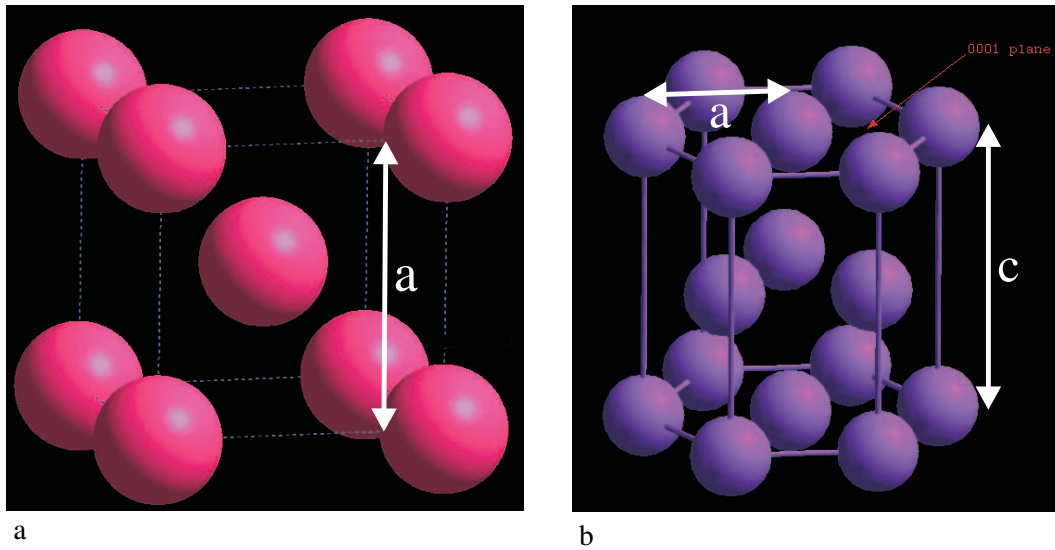


Figure 2.2: **a** Primitive cell of the bcc structure. The measured lattice constant is $a = 4.12 \text{ \AA}$ [15], ($T = 1.7 \text{ K}$, $p = 28.4 \text{ bar}$). **b** Primitive cell of the hcp structure. The measured lattice constant are $a = 3.67 \text{ \AA}$ and $c = 6.01 \text{ \AA}$ [16, 15], ($T = 1 \text{ K}$, $p = 26 \text{ bar}$).

2.2.3 He-He interaction

The interaction between two noble gas atoms can be modelled by a Lenard-Jones potential (Fig. 2.3):

$$V(r) = 4\epsilon \left[\left(\frac{\sigma}{r} \right)^{12} - \left(\frac{\sigma}{r} \right)^6 \right] \quad (2.1)$$

The first term represents the Pauli-repulsion, which is due to the closed shell configuration of the atoms. The second, attractive potential is of the van-der-Waals type, which is particularly weak for helium as the lightest noble gas atom. Helium is the element with the smallest polarizability ($\alpha = 0.123 \text{ cm}^3/\text{mol}$). The depth of the potential is 11.0 K and the potential crosses the abscissa at $\sigma = 2.6 \text{ \AA}$. [17]. The He-He potential is minimal at $r_0 = 2.9 \text{ \AA}$. The low boiling point of 4.2 K is due to the weak interatomic helium attraction.

2.2.4 Optical properties

Helium is transparent in the visible and in the IR-region. This is an important prerequisite for the optical spectroscopy as well as for the magnetic resonance spectroscopy of impurity atoms. The transition lines of helium are in the VUV-region. The transition from the 1^1S_0 ground state to the first excited state 2^1P_1 occurs at $\lambda = 58.4 \text{ nm}$. The refraction index n can be determined from the Clausius-Mosotti equation. For solid helium with a molar volume of $V_m = 21 \text{ cm}^3/\text{mol}$ one obtains

$$n = \sqrt{\bar{\epsilon}} = \sqrt{\frac{3 + 8\pi\alpha/V_m}{3 - 4\pi\alpha/V_m}} = 1.036, \quad (2.2)$$

where $\alpha = 0.123 \text{ cm}^3/\text{mol}$ is the polarizability. At the fluid-solid phase decreases the molar volume by approximately 10% and gives rise to a change of the refraction index by 0.3%. The growing of a crystal as well as the bcc-hcp transition can thus observed by eye.

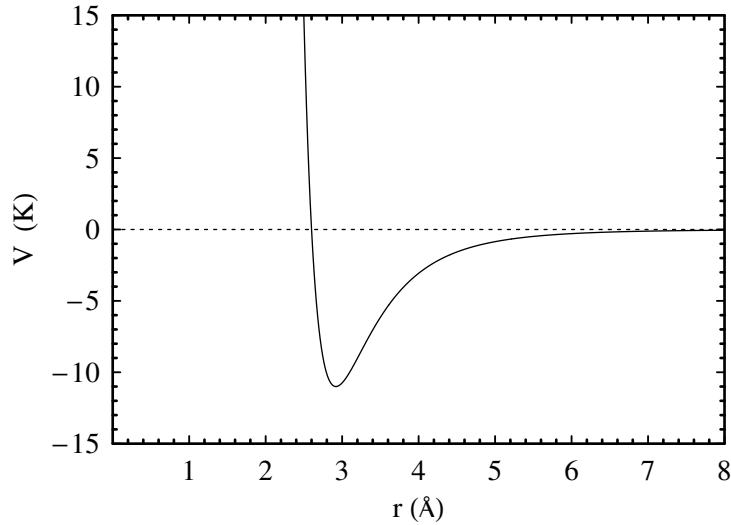


Figure 2.3: Lennard-Jones potential for He-He interaction. The depth of the potential minimum at $r_0 = 2.9 \text{ \AA}$ is 11 K.

The axial symmetry of the hcp phase induces optical birefringence. the difference between the ordinary and the extraordinary refraction indices is $\Delta n = |n_e - n_o| = 2.6 \cdot 10^{-6}$ at $\lambda = 633 \text{ nm}$ [18].

2.3 Setup and implantation technique

The experiments are performed in a cubic pressure cell made from copper which is immersed into the helium bath of an optical cryostat Fig. 2.4. Temperatures down to 1.4 K are reached by pumping on the he gas over the helium bath. The cryostat has optical access from three orthogonal directions. The pressure cell has a volume of 150 cm^3 . Its five quartz windows are fitted by sealing rings made from ultra-pure aluminium onto the cell.

A crystal is grown by supplying pressurized helium gas from an external pressure reservoir. A Cs metal target is situated at the bottom, inside the pressure cell. Helium atoms are sputtered from the target by means of frequency doubled Nd:YAG laser pulses (532 nm, $\sim 20 \text{ mJ}$), which are focussed by a height-adjustable lens ($f = 10 \text{ mm}$) onto the Cs target. At the same time the helium crystal melts locally and the cesium atoms diffuse into the molten region. By rising the lens the atoms can be brought to the center of the pressure cell. The crystal freezes again after the Nd:YAG laser is switched off. The sample region contains approximately 10^8 - 10^9 atoms per cubic centimeter. After the implantation process further low intensity pulses are applied every ten seconds. Their purpose is to dissociate Cs clusters, which form on a time scale of 10-100 s [8].

The atomic sample is irradiated by a resonant infrared laser beam. The induced fluorescence is collimated by a lens before it exits the cryostat.

Three pair of Helmholtz coils (outside the pressure cell) allow the applications of magnetic fields, whereas another set of three coil pairs inside the pressure cell allow the application of rf-fields.

The two magnetic shields shown in Fig 2.4 have been replaced in the mean time by a three layer shield surrounding the whole cryostat. Details of the setup are given in [13].

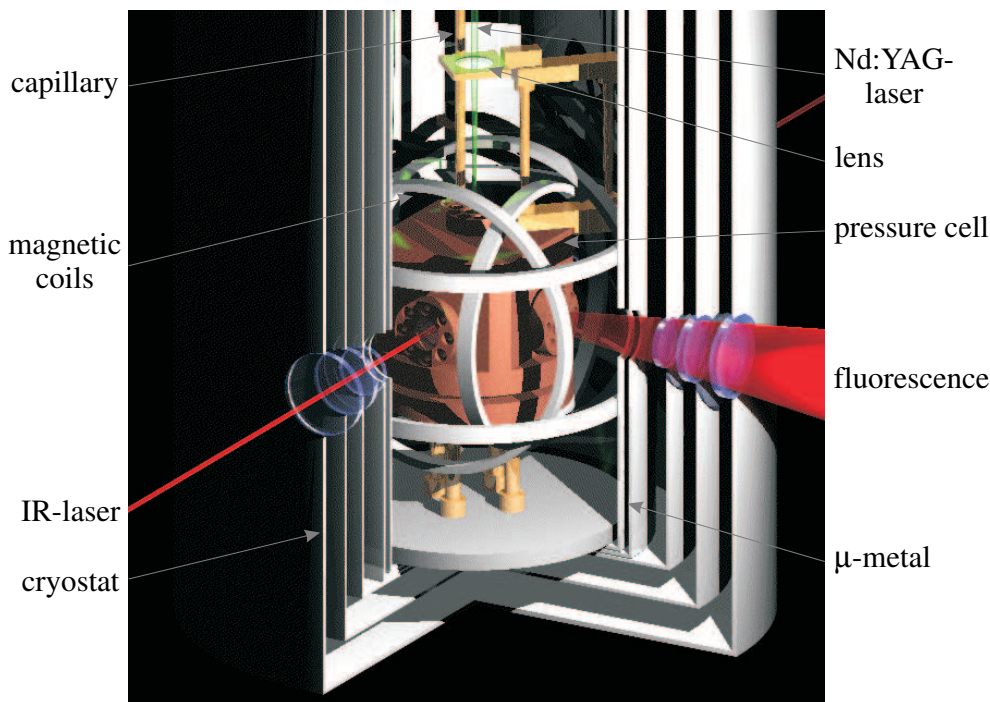


Figure 2.4: View into the cryostat.

2.4 The optical properties of Cs atoms in solid helium: The spherical bubble model

Solid helium has a very weak binding energy and it is highly compressible. As a consequence an impurity atom strongly disturbs the crystal structure in its vicinity. Matrix-isolated alkali atoms form bubble-like cavities due to the Pauli repulsion between the unpaired valence electron of the alkali atom and the closed-shell electronic configuration of helium. The size of the bubble is determined by the balance between the Pauli repulsion on the one side and the bubble surface tension and the pressure-volume work required for the bubble creation on the other side.

In the isotropic bcc phase the shape of the bubble is only determined by the symmetry of the impurity atom. The $6S_{1/2}$ state and the $6P_{1/2}$ of atomic cesium are spherically symmetric and are thus confined by spherical bubbles. The optical properties regarding the D_1 transition of Cs in solid helium can therefore be described in the frame of the so-called spherical bubble model, which was originally developed for the description of matrix-isolated excess electrons [19, 20]. A review and introduction to the application of this model to atomic impurities is given in [21], whereas a complete treatment can be found in [13].

The basic features of the optical spectra can be understood on the basis of the bubble evolution during the absorption-emission cycle of resonance radiation illustrated in Fig. 2.5. At the beginning the atom is in its $6S_{1/2}$ ground state, from where it is excited to the $6P_{1/2}$ state by absorbing a photon. Due to the Franck-Condon principle the shape of the cavity does not change during the absorption process, although the $6P_{1/2}$ wavefunction occupies more volume than the ground state wavefunction. As a consequence more energy is necessary to excite the atom leading to a blue shift of the excitation line (851 nm) with respect to the D_1 -transition line of free atomic Cs (894 nm). Moreover, due to zero-point oscillations of the ground state bubble radius, one observes a very strong homogeneous broadening of the line (≈ 10 nm FWHM).

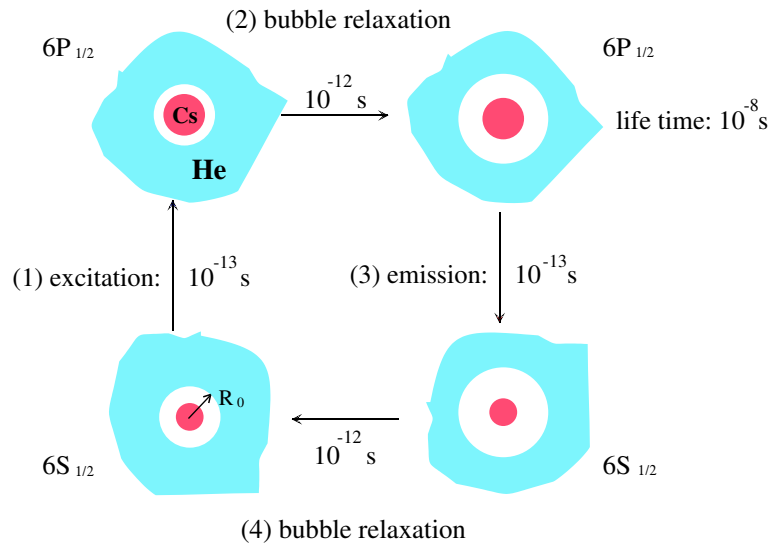


Figure 2.5: Schematic representation of a D_1 absorption-emission cycle of Cs trapped in solid helium.

Following the excitation the bubble shape relaxes by increasing its radius in order to minimize the total energy of the system. The spontaneous emission takes place in this relaxed bubble, which again does not change its shape during the decay. The emission line at 888 nm is due to the larger bubble radius, which is less disturbed than the excitation line. Again the emission line is broadened by radial bubble oscillations. Finally the bubble relaxes again and to its original shape. Typical time scales of the four processes of a complete absorption-emission cycle are given in the figure. The rate of the bubble relaxations was estimated from the speed of sound in solid helium.

The position and shapes of the excitation and emission lines depend on the pressure of the helium matrix. This is evident since the bubble radius becomes smaller with increasing pressure, whereas the helium density increases. The pressure dependence of the D_1 excitation line is shown in Fig. 2.6. Data taken in liquid He II [22], in the bcc phase and in the hcp phase of solid helium are represented [9]. One observes a general blue-shift of the line with increasing pressure. This is what one expects from the spherical bubble model. However, the jump at the liquid-bcc phase transition can only be partly understood from the discontinuous increase of the helium density at the phase transition [9]. Moreover, at the phase transition to hcp the excitation line is red-shifted by 2 nm although the helium density increases. This is in clear contradiction to the spherical bubble model. The effects are due to the specific structure differences of the phases, which are not included in the model. In the axially symmetric hcp phase the bubble shape is expected to be ellipsoidally deformed causing a perturbation of the electronic structure of the atom. The perturbation will be in lowest order of quadrupolar symmetry. By treating the problem in perturbation theory it becomes evident that the perturbed S ground state of cesium will have a D-state admixture [9]. Detailed calculations show that this D-state admixture may be responsible for the observed red-shift [23].

Until now only the D_1 line of Cs trapped in solid helium was discussed. The excitation and emission spectra of the D_2 line are more complicated than those of the D_1 line. In contrast to the $6P_{1/2}$ state the $6P_{3/2}$ is not of spherical symmetry, but has an apple-like shape with a nodal line defined by the quantization axis. Along this line helium atoms are attracted by the cesium core. This binding force allows the formation of Cs^*He_2 exciplexes, in which the two helium atoms are located at the two opposing hollows of the electronic configuration. In

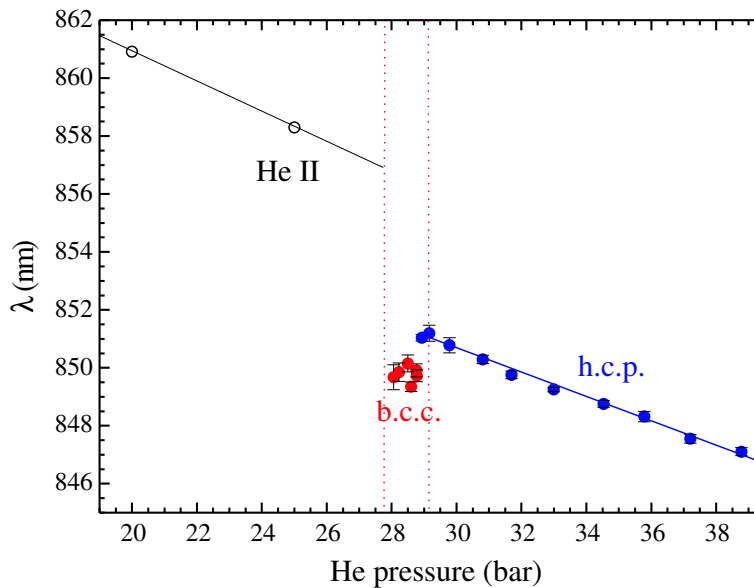


Figure 2.6: Shift of the D_1 excitation line of Cs atoms in the pressurized phases of condensed helium. The data measured in He II (open circles) are taken from [22]. The data taken in the bcc and hcp phases were measured by our group. The graph is taken from [9].

a more complicated process the $6P_{1/2}$ state can also lose its spherical symmetry and become dumbbell-shaped. Helium atoms will then be bound on a ring concentric with the waist of the dumbbell. These complexes are Cs^*He_n exciplexes with $n > 2$. The formation and the emission lines of these exciplexes are discussed in chapter 3.

2.5 Optical Pumping

Optical pumping is an effective technique to spin-polarize an atomic ensemble. It was invented by Brossel and Kastler [24]. The general idea is to transfer angular momentum from resonant circularly polarized light to the spin ensemble. The principle is illustrated in Fig. 2.7 for the D_1 transition of Cs in solid helium. Shown are the hyperfine Zeeman-levels of the $6S_{1/2}$ and the $6P_{1/2}$ state. Resonant circularly polarized σ_+ -light drives $\Delta M = +1$ transitions thereby increasing the magnetic quantum number M by one unit at each absorption of a light photon. Note that the hyperfine splitting of both ground and excited states are not resolved due to the large homogeneous width (≈ 10 nm) of the optical line. For the same reason the optical transition is not saturated by applying typical experimental light intensities of less than 1 mW/mm². Stimulated emission processes can hence be neglected. The excited atoms decay via spontaneous emission back to the ground state. With a repeated number of such absorption-emission cycles the Zeeman ground states with larger M values become more populated than those with smaller M values. Finally all atoms are "pumped" to the Zeeman level with maximal M , i.e., $M = 4$ in the $F = 4$ level. The population does not change anymore since this state does not couple to the circularly polarized light. It is therefore called a *dark state*.

Optical pumping of Cs atoms in solid helium was first observed by Weis et al. [25] and it was investigated in depth in [11]. The most important result of the latter study was that the pumping mechanism in solid helium is of the so called Kastler-type. One speaks of Kastler-pumping, or *repopulation pumping*, when the spin-polarization is preserved while the atom is in the excited state. The non-perturbation of the spin in the excited state is due to the spherical

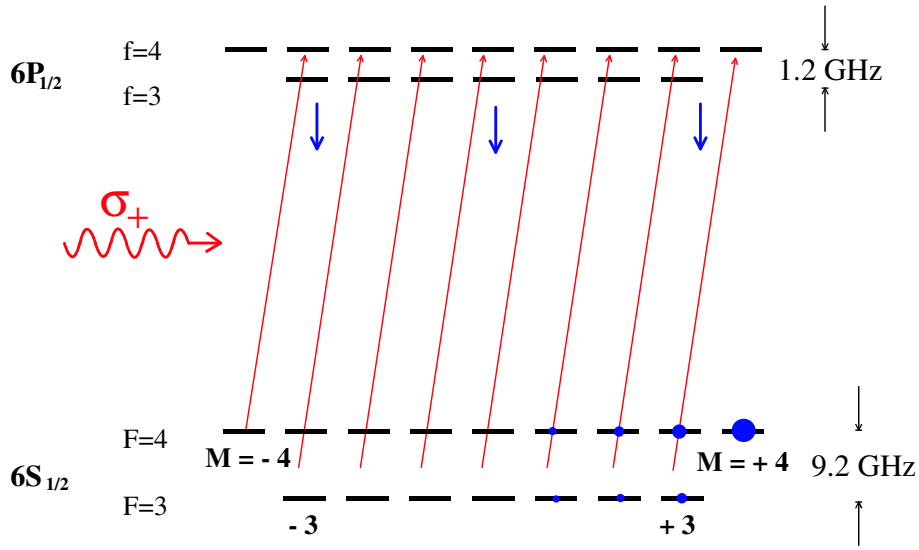


Figure 2.7: Hyperfine Zeeman levels of the Cs D₁ line. The hyperfine splitting can not be resolved optically owing to the large optical line width of the D₁ line in solid helium.

symmetry of the trapping site and the diamagnetic character of the helium crystal.

The preparation of spin-polarization by optical pumping is a necessary step for the observation of magnetic resonance transitions.

2.6 Optically detected magnetic resonance (ODMR)

Our standard method for detecting magnetic resonance transitions is the optically detected magnetic resonance (ODMR). In the simplest version of ODMR spectroscopy a constant magnetic field is applied parallel to the optical pumping beam. The atoms are pumped to a large extent towards the dark state, so that no or only a weak fluorescence signal is detected. By applying resonant rf-fields the spin-polarization, i.e., the relative Zeeman level populations, are altered. States with lower M become repopulated causing an increase of the fluorescence signal. ODMR is very sensitive owing to the high quantum efficiencies with which optical photons can be detect transitions induced by rf-photons.

Fig. 2.8 shows a typical ODMR signal taken in the bcc phase of solid helium. A magnetic field of $4.2 \mu\text{T}$ was applied while the radio frequency was scanned over a range of 100 Hz. The Zeeman resonances of the $F = 3$ and $F = 4$ ground state hyperfine levels are resolved. The existence of the weak $F = 3$ line indicates that the atoms are not completely pumped to the $|F = 4, 4\rangle$ dark state. The width of the $F = 4$ resonance of 11.7 Hz corresponds to a spin-coherence time of 269 ms. The narrow widths of the resonance lines are due to the isotropic character of the bcc phase. In the hcp phase the magnetic resonance lines are two to three orders of magnitude broader. Moreover, in the hcp phase resonances can be observed even in $B = 0$ as it can be seen in Fig. 2.9. The reason is again, as in the case of the optical spectra, a quadrupolar perturbation which in this case splits the Zeeman level quadratically according to $\omega_{F,M} \propto [F(F+1) - 3M^2]$ [9]. The peak positions in Fig. 2.9 are well explained in this model, whereas their relative intensities are not understood yet. The deformation of the bubble in the hcp phase can be deduced from the line splittings, i.e. from the strength of the perturbation. One gets a comparable result as from the red shift of the optical line in the hcp phase, discussed above [23].

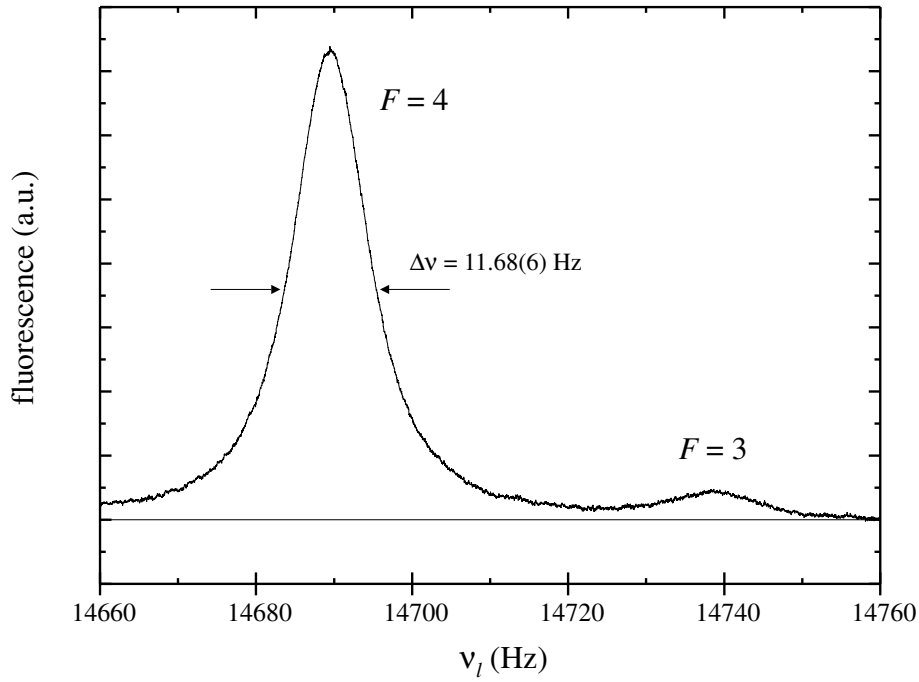


Figure 2.8: Typical ODMR signal taken in the bcc phase of solid helium ($T = 1.6$ K, $p = 27.6$ bar) in a field of $4.2 \mu\text{T}$. Magnetic resonances in the $F = 3$ and $F = 4$ hyperfine states are resolved. The measured width corresponds to a transverse relaxation time of $T_2 = 269$ ms. The graph is taken from [13].

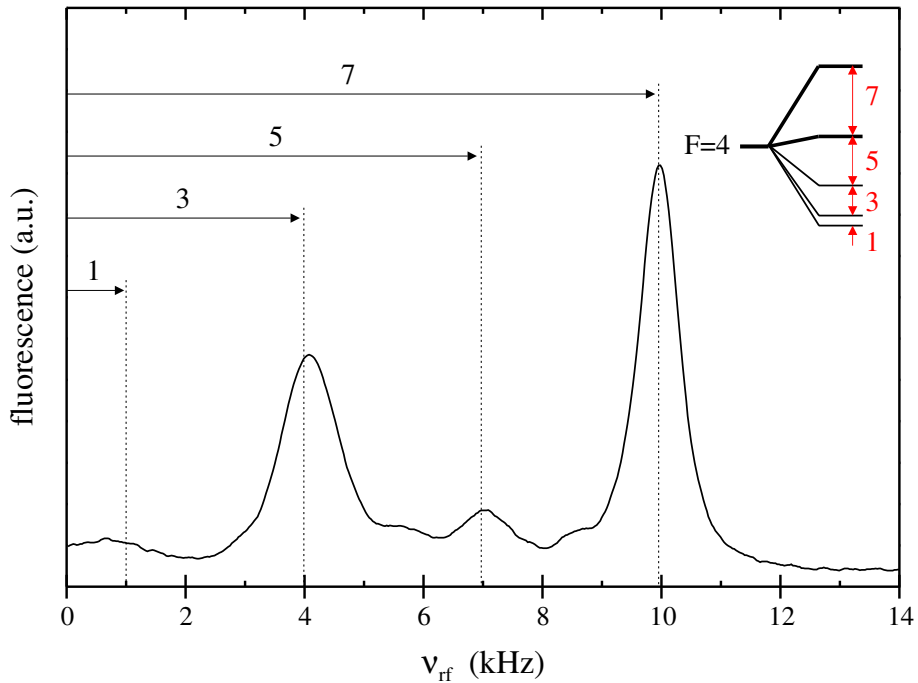


Figure 2.9: Zero magnetic field spectrum taken in the hcp phase of solid helium ($T = 1.53$ K, $p = 29.4$ bar). Due to the axial symmetry of the helium crystal the Zeeman states are perturbed by an interaction of quadrupolar symmetry: $\omega_{F,M} \propto [F(F+1) - 3M^2]$. The $|M|$ depending splitting of the Zeeman levels is illustrated.

References

- [1] M. Arndt, S. I. Kanorsky, A. Weis, and T. W. Hänsch. Can paramagnetic atoms in superfluid helium be used to search for permanent electric dipole moments? *Phys. Rev. Lett.*, 174:298, 1993.
- [2] A. Weis, S. I. Kanorsky, S. Lang, and T. W. Hänsch. Can atoms trapped in solid helium be used to search for physics beyond the standard model? In *Lecture Notes in Physics*. Springer Verlag, 1996.
- [3] S. I. Kanorsky, M. Arndt, R. Dziewior, A. Weis, and T. W. Hänsch. Pressure shift and broadening of the resonance line of barium atoms in liquid helium. *Phys. Rev. B*, 50(9):6296, 1994.
- [4] S. I. Kanorsky, M. Arndt, R. Dziewior, A. Weis, and T. W. Hänsch. Optical spectroscopy of atoms trapped in solid helium. *Phys. Rev. B*, 49(5):3645, 1994.
- [5] M. Arndt, R. Dziewior, S. Kanorsky, A. Weis, and T. W. Hnsch. Implantation and spectroscopy of metal atoms in solid helium. *Z. Phys. B*, 98(3):377–381, 1995.
- [6] M. Arndt, S. I. Kanorsky, A. Weis, and T. W. Hänsch. Long electronic spin relaxation times of Cs atoms in solid ^4He . *Phys. Rev. Lett.*, 74(8):1359, 1995.
- [7] S. I. Kanorsky, S. Lang, S. Lücke, S. B. Ross, T. W. Hänsch, and A. Weis. Millihertz magnetic resonance spectroscopy of Cs atoms in body-centered-cubic ^4He . *Phys. Rev. A*, 54(2):R1010, 1996.
- [8] Steffen Lang. *Optisch detektierte Magnetresonanz an Cäsium Atomen in festem ^4He* . Ph.D. thesis, Ludwig-Maximilians-Universität München, 1997.
- [9] Taro Eichler. *Magneto-optical Spectroscopy of Alkali Atoms in Helium Crystals*. Ph.D. thesis, Rheinische Friedrich-Wilhelms-Universität Bonn, 2000.
- [10] S. Kanorsky, S. Lang, T. Eichler, K. Winkler, and A. Weis. Quadrupolar deformations of atomic bubbles in solid ^4He . *Phys. Rev. Lett.*, 81(2):401, 1998.
- [11] S. Lang, S. I. Kanorsky, T. Eichler, R. Müller-Siebert, T. W. Hänsch, and A. Weis. Optical pumping of Cs atoms in solid ^4He . *Phys. Rev. A*, 60(5):3867, 1999.
- [12] Taro Eichler, R. Müller-Siebert, Daniel Nettels, S. I. Kanorsky, and A. Weis. Optical detection of nonradiating alkali atoms in solid helium. *Phys. Rev. Lett.*, 88(12):123002, 2002.
- [13] R. Müller-Siebert. *Optimierung und Charaktersierung eines Tieftemperatur-Spektrometers zur Untersuchung von magneto- und elektro-optischen Effekten an Alkaliatomen in He-Kristallen*. Ph.D. thesis, Universität Freiburg (Schweiz), 2002.
- [14] D. Nettels, R. Müller-Siebert, X. Huang, S. Ulzega, and A. Weis. Magnetic and electric properties of alkali atoms in solid helium. *Physica B*, 329:406, 2003.
- [15] E. B. Osgood, V. J. Minkiewicz, T. A. Kitchens, and G. Shirane. Inelastic-neutron scattering from bcc ^4He . *Phys. Rev. A*, 5(3):1537, 1972.
- [16] V. J. Minkiewicz, T. A. Kitchens, F. P. Lipschultz, R. Nathans, and G. Shirane. Phonon spectrum of hcp He^4 . *Rev. Mod. Phys.*, 174(1):267, 1968.

- [17] Henry R. Glyde. *Excitations in liquid and solid helium*. Clarendon Press - Oxford, 1994.
- [18] R. H. Crepeau, O. Heybey, D. M. Lee, and Stanley A. Strauss. Sound propagation in hcp solid helium crystals of known orientation. *Phys. Rev. A*, 3(3):1162, 1971.
- [19] Joshua Jortner, Neil R. Kestner, A. Rice, and M. H. Cohen. Study of properties of an excess electron in liquid helium. i. the nature of the electron-helium interactions. *J. Chem. Phys.*, 43(8):2614, 1965.
- [20] Kazuo Hiroike, Neil R. Kestner, Stuart A. Rice, and Joshua Jortner. Study of properties of an excess electron in liquid helium. ii. a refined description of configuration changes in the liquid. *J. Chem. Phys.*, 43(8):2625, 1965.
- [21] Serguei Kanorsky and Antoine Weis. Atoms in nano-cavities. In *Quantum optics of confined systems*. Kluwer Academic Publishers, 1995.
- [22] T. Kinoshita, K. Fukuda, Y. Takahashi, and T. Yabuzaki. Optical properties of impurity atoms in pressurized superfluid helium. *Z. Phys. B*, 98:387, 1995.
- [23] A. Weis. (private communication).
- [24] J. Brossel and A. Kastler. La detection de la resonance magnetique des niveaux excités - l'effet de dépolariation des radiations de résonance optique et de fluorescence. *C. R. Acad. Sci.*, 229(23):1213–1215, 1949.
- [25] A. Weis, S. I. Kanorsky, M. Arndt, and T. W. Hänsch. Spin physics in solid helium: experimental results and applications. *Z. Phys. B*, 98(3):359, 1995.

Chapter 3

Observation of apple- and dumbbell-shaped Cs^*He_n exciplexes in solid He^4

D. Nettels, A. Hofer, P. Moroshkin, R. Müller-Siebert, S. Ulzega, and A. Weis

Département de Physique, Université de Fribourg, Chemin du Musée 3, 1700 Fribourg, Switzerland

to be submitted

Abstract: We report the observation of several new spectral features in the fluorescence of cesium atoms implanted in the hcp phase of solid helium ($T = 1.5$ K, $p = 31.6$ bar) following laser excitation to the 6^2P states. Based on calculations of the emission spectra by using semiempirical Cs-He potential curves the newly discovered lines could be assigned to the decay of specific Cs^*He_n exciplexes. An intense line at 10520 cm^{-1} following D_2 excitation, is attributed to $\text{Cs}(\text{AII}_{3/2})\text{He}_2$ exciplexes, while a weaker emission at 10160 cm^{-1} following D_1 excitation is identified to originate from $\text{Cs}(\text{AII}_{1/2})\text{He}_2$. The most intense peak, observed at 7130 cm^{-1} following D_2 excitation, could not clearly be assigned. It originates from the decay of a Cs^*He_n exciplex with a well defined number n of helium atoms bound as a ring around the Cs atom. The calculations suggest $\text{Cs}(\text{AII}_{1/2})\text{He}_6$ to be the most probable candidate. The observations contradict the commonly accepted belief that Cs^*He_n exciplexes with $n > 2$ do not exist.

3.1 Introduction

Alkali atoms and helium atoms strongly repel each other by virtue of the Pauli principle. However, alkali atoms excited to the lowest lying P states can exert an attractive potential on helium atoms and lead to bound states (Cs^*He_n), known as exciplexes. In 1995 the formation of such

exciplexes was considered by Dupont-Roc [1] and Karnorsky et al. [2] as an explanation for the quenching of atomic fluorescence from light alkali atoms (Na, Li) embedded in solid or liquid He⁴. In the meantime (light and heavy) alkali-helium exciplexes have been observed in different environments, such as liquid helium and cold helium gas [3, 4], as well as on the surface of helium nanodroplets [5, 6, 7, 8]. Here we present the first observations of such exciplexes in a solid helium matrix.

The alkali-helium interaction at short interatomic distances is dominated by the spherically symmetric Pauli repulsion between the valence electron of the *S* ground state alkali atom and the closed electronic shell of the helium atom. If in contrast the alkali atom is in an excited *P* state helium atoms can be attracted, if they approach along a nodal line or a nodal plane of the electronic configuration. As Dupont-Roc has first pointed out the strength of the spin-orbit interaction in the *P* state plays a key role in this process. If it is weak compared to the Cs-He interaction, as in the case of sodium it can be neglected and the possible electronic configurations are the well known $P_{x,y,z}$ orbitals. Helium atoms are attracted along their nodal planes and can be bound as a ring around the waist of these orbitals. If on the other hand the spin-orbit interaction is strong, as for cesium, one has to consider the electron distributions of the L-S-coupled $P_{1/2}$ and $P_{3/2}$ states. The $P_{1/2}$ states are spherical, while the $P_{3/2}$ states have either apple-like (for $m_j = \pm 1/2$) or dumbbell-like (for $m_j = \pm 3/2$) shapes with a corresponding nodal line or nodal plane. Dupont-Roc concluded that only the $P_{3/2}$ state of cesium can bind helium atoms and that their maximal number n_{max} is restricted to two atoms, each being bound to one of the two opposing hollows of the apple like shape. This was supported by recent experimental evidence from a Japanese group [3], which observed Cs*He₁ and Cs*He₂ exciplexes from cesium in a cold helium gas and found no evidence for exciplex states with $n > 2$. However, the simple theory neglects that the shape of the electronic configuration changes adiabatically as helium atoms approach. As we will discuss below the spherical $P_{1/2}$ state changes to an apple like form if one helium atom has enough energy to overcome an initially repulsive potential barrier. The Cs*He₁ state then allows the binding of a second helium atom, which is attracted without barrier resulting in a Cs*He₂ complex. In the $P_{3/2}$ state the formation of the corresponding complex can be formed without having to overcome a potential barrier. If a further third atom overcomes a corresponding barrier the electronic configuration switches from apple-like to dumbbell-like shape and the binding of even more helium atoms becomes possible, up to a maximal number n_{max} of helium atoms, determined by the interatomic repulsion of the helium atoms located on a ring. All these processes have been observed experimentally in alkali atom, which are lighter than cesium. The maximal number of helium atoms was found to be $n_{max} = 4$ for K*He_n [9], and $n_{max} = 6$ for Rb*He_n [4]: However, as mentioned already, for Cs*He_n only $n = 1, 2$ was observed. Very detailed experimental and theoretical studies of the formation of rubidium and cesium exciplexes were recently published by the Kyoto group [3, 4]. In particular the authors discuss, based on dynamical and energetic considerations, why the formation of higher order Cs*He_n might be suppressed. They regard the formation of exciplexes as a sequential process, where one helium atom per time is bound to the complex, and show that already the formation of Cs*He₃ exciplexes is strongly suppressed.

The detection of exciplexes is usually performed by monitoring their emission spectrum after optical excitation. The emission line is red-shifted with respect to the excitation profile, and the shift increases with the number n of bound helium atoms. A different detection has been used in [9], where K*He_n molecules, detached from the surface of helium clusters were detected by means of mass-spectroscopy.

In earlier publications we have studied the excitation and fluorescence spectra of atomic cesium implanted into the bcc and hcp phases of solid helium [10, 11, 12]. It was found that the excitation at the D_1 transition ($6S_{1/2}$ - $6P_{1/2}$) results in atomic fluorescence at the same

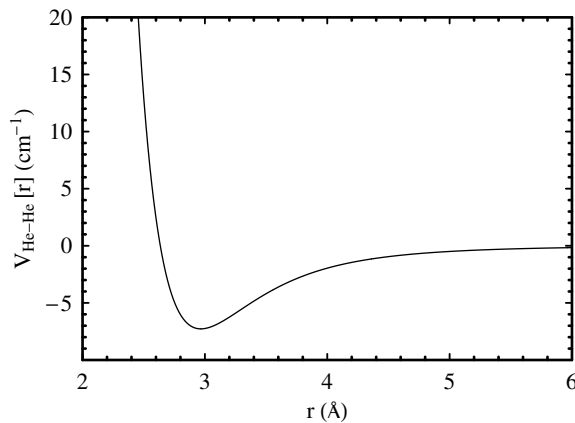


Figure 3.1: He-He interaction potential according to Beck [13].

transition, blue shifted (with respect to the free Cs atom) by the interaction with the helium matrix. At the same time, the excitation on the D_2 transition ($6S_{1/2}$ - $6P_{3/2}$) produced merely a weak fluorescence on the D_1 emission line, which indicates that the $6P_{3/2}$ atoms are partly quenched into the $6P_{1/2}$ state. Recently the extension of the spectral range of our detection system has allowed us to discover two new, intense emission lines at 7130 cm^{-1} and 10520 cm^{-1} . A very weak emission at 10160 cm^{-1} following D_1 excitation was also found. We attribute these emission lines to the formation and decay of Cs^*He_n exciplexes.

In this paper we present the results of experimental and theoretical investigations of the structure and emission spectra of Cs^*He_n exciplexes. Our analysis predicts quasi-bound states with $n = 3\dots 5$ and $n = 7$ helium atoms and a stable bound state with $n = 6$ atoms. For $n = 1, 2$ there exist both bound and quasi-bound states. While an apple-like Cs^*He_2 exciplex was unambiguously identified, the precise assignment of the number n_{max} of atoms bound in the observed dumbbell-shaped exciplex $\text{Cs}^*\text{He}_{n_{\text{max}}}$ requires a future more accurate theoretical consideration of the vibrational mode structure and of the effects of the surrounding helium matrix.

The article is organized as follows: in Sec. 3.2 we present the theoretical model used, Sec. 3.3 describes the experiments and results, and in Sec. 3.4 the numerical results are compared to the experimental data. The the main results are summarized in Sec. 3.5.

3.2 Theoretical calculation of the emission spectra

We calculated the emission spectra of decaying Cs^*He_n exciplexes with a treatment similar to the ones in [3, 4]. We consider only the influence of the n helium atoms that form the exciplex and neglect the influence of the bulk of the surrounding helium matrix. This is a good approximation as the emission spectra are mainly determined by the n bound helium atoms.

3.2.1 $\text{Cs}^*\text{-He}_n$ exciplex potentials

The interaction between one cesium atom and the n He atoms is described as the sum over adiabatic molecular two-body interaction potentials. We use the potentials between helium ground state atoms and alkali atoms in their ground and lower excited states calculated by Pascale [14]. For the $6S$ ground state the potential, denoted as $V_{\sigma}^{6s}(r)$, is radially symmetric.

For the 6P states the interaction is anisotropic and can be expressed by the operator

$$V^{6P}(\mathbf{r}) = V_{\sigma}^{6P}(r) + \left(\frac{\mathbf{L} \cdot \mathbf{r}}{\hbar r} \right)^2 [V_{\pi}^{6P}(r) - V_{\sigma}^{6P}(r)], \quad (3.1)$$

where $\mathbf{r} = \mathbf{r}(r, \theta, \varphi)$ denotes the position vector of a helium atom with respect to the cesium atom and \mathbf{L} is the electronic angular momentum operator of the cesium atom [1]. Stable exciplexes of the form Cs*He_{n=2} are formed by two helium atoms located on a common axis on opposite sides of the cesium atom. For Cs*He_{n>3} the helium atoms are distributed on a concentric ring around the alkali atom. The summation over the pair potentials can be expressed by the operator (for $n = 1, 2, \dots$)

$$V_n^{Cs-He}(r) = \sum_{i=1}^n V^{6P}(\mathbf{r}_i), \quad (3.2)$$

with $\mathbf{r}_i = \mathbf{r}(r, \theta = \pi/2, \varphi_i = i2\pi/n)$. In addition we include He-He interactions by summing over the corresponding potentials $V_{He-He}(|\mathbf{r}_i - \mathbf{r}_{i+1}|)$ between neighboring helium atoms. The He-He interaction is modelled by the semi-empirical potential given by Beck [13]:

$$V_{He-He}(r) = Ae^{-\alpha r - \beta r^6} - \frac{C}{(r^2 + a^2)^3} \left[1 + \frac{b + 3a^2}{r^2 + a^2} \right], \quad (3.3)$$

with $A = 3.213 \cdot 10^6 \text{ cm}^{-1}$, $C = 7004 \text{ cm}^{-1} \text{ \AA}^6$, $a = 0.675 \text{ \AA}$, $b = 2.709 \text{ \AA}^2$, $\alpha = 4.390 \text{ 1/\AA}$ and $\beta = 3.746 \cdot 10^{-4} \text{ 1/\AA}^6$. This potential is shown in Fig. 3.1. The distance between two neighboring helium atoms is a function of the cesium helium separation r and the number n of helium atoms. One has $|\mathbf{r}_i - \mathbf{r}_{i+1}| = 2r \sin(\pi/n)$. The summation over all helium pairs then gives

$$V_n^{He-He}(r) = nV_{He-He}(2r \sin(\pi/n)) \quad (3.4)$$

After including the alkali spin-orbit interaction the total interaction potential of the Cs*He_n system reads

$$V_{Cs^*He_n}(r) = V_n^{Cs-He}(r) + V_n^{He-He}(r) + 2/3\Delta \mathbf{L} \cdot \mathbf{S}, \quad (3.5)$$

where $\Delta = 554.0 \text{ cm}^{-1}$ is the fine-structure splitting of the free cesium 6P state and \mathbf{S} the electronic spin operator. $V_{Cs^*He_n}(r)$ is diagonalized algebraically. In Figs. 3.2 and 3.3 the resulting r -dependence of the eigenvalues are shown for Cs*He₂ and Cs*He₆ respectively. The same plots also show the ground state potentials given by $nV_{\sigma}^{6s}(r) + V_n^{He-He}(r)$. The potentials are labelled according to their electronic configuration as $X^2\Sigma_{1/2}$, $A^2\Pi_{1/2}$, $A^2\Pi_{3/2}$ and $B^2\Sigma_{1/2}$. The quantization axis is defined by the symmetry axis of the exciplexes, which is the internuclear axis of the cesium atom and the two helium atoms in the case of Cs*He_{n=1,2}, whereas for Cs*He_{n>3} it is the axis of the helium ring. Pictographs next to the curves show the variation of the cesium electronic density as the n helium atoms, indicated by two filled circles, approach the cesium atom. Note that the cuts through the electron orbitals are drawn to scale. For calculating the equi-probability lines in the pictographs we used radial wavefunctions of the cesium 6S and 6P states from a statistical Thomas-Fermi model of the atom following the procedure given by Gombás [15]. The lines indicate the rotational symmetry axis of the different configurations and have a length corresponding to 16 Å. The helium atoms are drawn with a diameter of 3.5 Å, which corresponds to the mean interatomic distance in the surrounding helium bulk.

From the adiabatic potentials of Fig. 3.2 and Fig. 3.3 one sees that the helium atoms, due to the Pauli principle, are repelled by the cesium valence electron. However in cases where

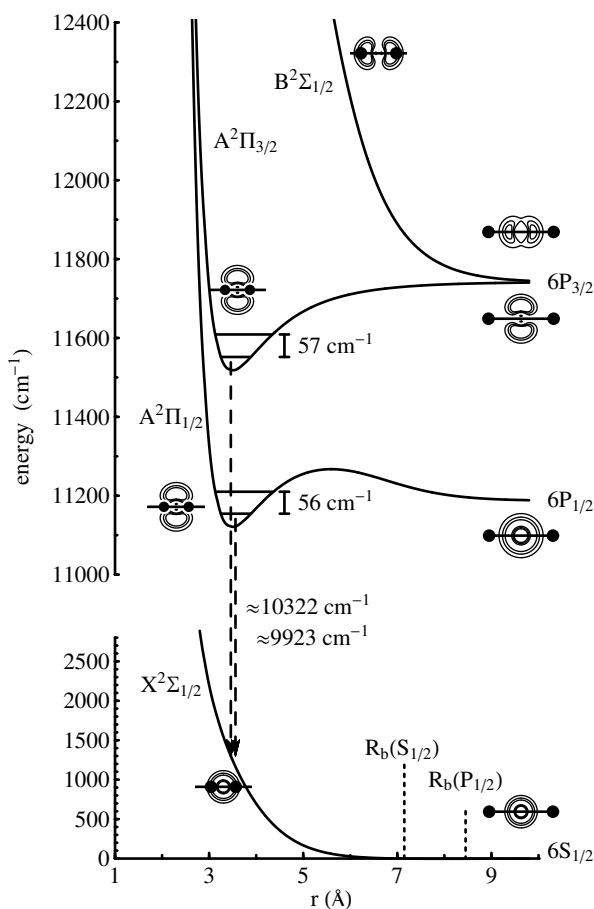


Figure 3.2: Adiabatic potentials of the Cs^*He_2 system, including the spin-orbit interaction. The two helium atoms are located at r and $-r$ on the quantization (rotational symmetry) axis, indicated in the pictographs by a solid line. The shape of the electronic density distribution of the cesium atom changes significantly as helium atoms (filled circles) approach. The $A^2\Pi_{1/2}$ potential well has only two vibrational levels. For the well of the $A^2\Pi_{3/2}$ state only the lowest two vibrational levels are shown. In both cases only the zero-point levels are populated at 1.5 K. The fluorescence transitions (dashed lines) are strongly red-shifted with respect to the D_1 and D_2 emission of the free cesium atom.

the atoms approach along a nodal line or on a nodal plane of the electron distribution they experience an attractive force until they are repelled by the cesium core. This definitely holds for the $\text{Cs}(A\Pi_{3/2})\text{He}_2$ exciplex. For $\text{Cs}(A\Pi_{1/2})\text{He}_2$ the situation is more complicated. When the two helium atoms are far away the electronic configuration is the one of the $6P_{1/2}$ state of the free cesium atom, which has a spherical symmetry and is hence, as the $6S_{1/2}$ ground state, repulsive for the helium atoms. However, when the helium atoms approach the cesium atom the electronic wave function of the latter is deformed and becomes apple-shaped. This new configuration now offers a binding potential minimum. The formation of this second configuration has a potential barrier of 79 cm^{-1} , which is much higher than the thermal energy. If, on the other hand, the two atoms do not approach simultaneously, but one after another, only the first atom has to pass the potential barrier in order to form the apple-like electronic configuration of a Cs^*He_1 structure, which is attractive for a second helium atom approaching from the opposite side.

A third helium atom approaching the $\text{Cs}(A\Pi_{1/2})\text{He}_2$ exciplex will be repelled. If it comes sufficiently close, the electronic configuration changes to a dumbbell shape, which has a binding minimum for the three helium atoms. Here, too, a potential barrier has to be overcome. The

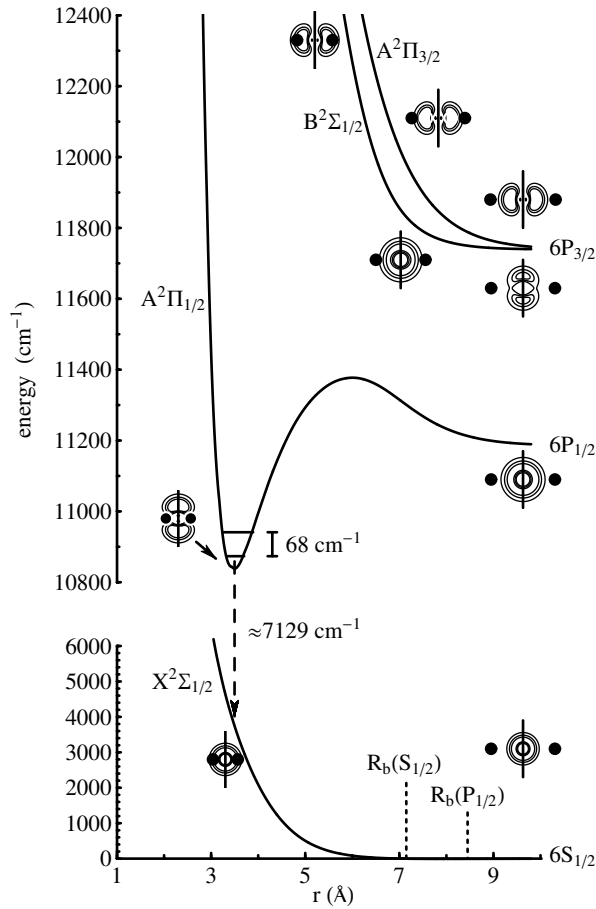


Figure 3.3: Adiabatic potentials of the Cs*He₆ system. The six helium atoms are located on a ring of radius r concentric with the symmetry axis. Only the $A^2\Pi_{1/2}$ potential has a binding attractive well.

three atoms are then bound and located on a ring concentric around the waist of the dumbbell. The Cs($A\Pi_{1/2}$)He₃ structure exerts a purely attractive potential on further helium atoms. With an increasing number of helium atoms on the ring the repulsive potential between these atoms increase, which puts a natural limit on the maximum number n_{\max} that can be accommodated. Only the $A\Pi_{1/2}$ state can bind more than two helium atoms as can be seen from Fig. 3.3.

We calculated the adiabatic potentials for all Cs*He_n systems up to $n = 9$. The n dependence of the potential depths $\epsilon_{\min}^{(n)}$ of the $A\Pi_{1/2}$ electronic states is represented in Fig. 3.4 by open circles. The values are given with respect to the dissociation limit, i.e. the energy of the $6P_{1/2}$ state of the free cesium atom. One observes that the minimum for $n = 3$ lies above the value for $n = 2$. For higher n the energy drops with increasing n . However as the distance between neighboring helium atoms becomes smaller their interatomic repulsion exceeds the attractive cesium helium interaction. The configuration with $n = 8$ has the deepest attractive potential. Also shown in Fig. 3.4 (open squares) are the heights of the potential barriers as a function of n . The barrier increases significantly when going from Cs*He₂ to Cs*He₃, but then has an almost constant level as n increases further. This reflects the fact discussed above that the binding of a third helium atom is accompanied by a change of the electronic configuration from apple-shaped to dumbbell-shaped.

Fig. 3.5 shows the radii of the potential minima as a function of n . Up to $n = 6$ the radii decrease slightly with an increasing number of helium atoms, due to the attractive He-He

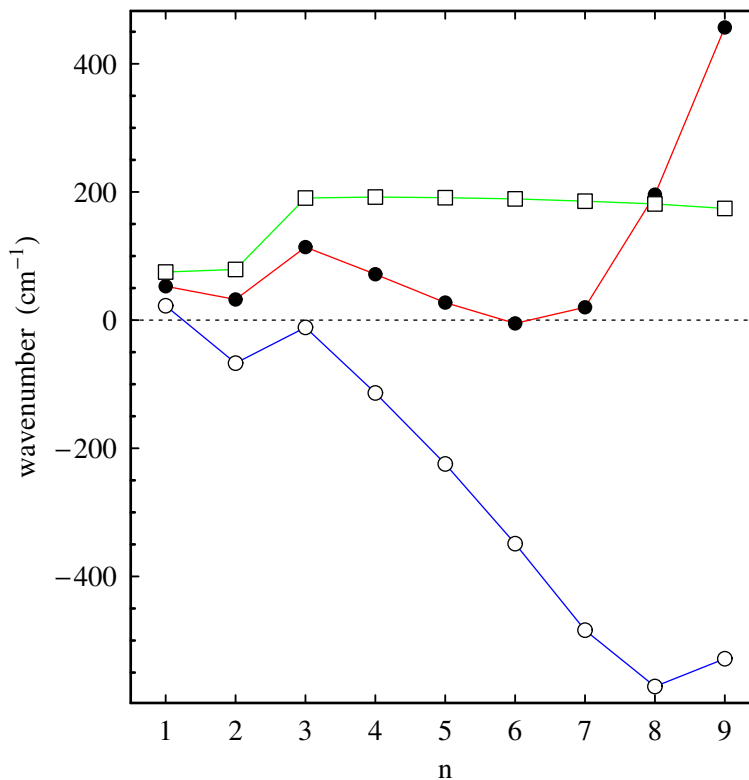


Figure 3.4: Energy dependences of the $\text{Cs}(6^2\Pi_{1/2})\text{He}_n$ exciplexes as a function of the number n of helium atoms. Shown are the minimal energies $\epsilon_{min}^{(n)}$ (open circle) of the potential wells, the barrier heights (open squares) and the total zero-point energies $\epsilon_0^{(n)}$ (filled circles). All energies are given with respect to the dissociation limit, i.e., the electronic energy of the $6P_{1/2}$ state. Corresponding points are joined by lines to guide the eye.

interaction. For $n > 6$ the radius increases rapidly due to the He-He repulsion.

3.2.2 Vibrational structure of the Cs^*He_n exciplexes

In order to determine the transition frequencies to the electronic ground state, the total energies of the bound states need to be calculated by including the energies of the vibrational modes of the exciplex system. Contributions from rotations can be neglected. We make the following simplifying assumptions. First, we treat the system as separable in the coordinates r_i, θ_i and φ_i of the individual helium atoms, which is a good approximation for sufficiently small oscillations around the equilibrium positions of the helium atoms. We further treat the mass of the cesium atom as infinite compared to the mass of the helium atoms. From the $3(n+1)$ degrees of freedom of the exciplex three are of translational nature and another three of rotational nature. The cesium atom can be considered as point particle, since its electronic structure changes adiabatically with the positions of the helium atoms, i.e., a rotation of the configuration of the helium atoms alone does not change the potential energy of the system.

For the radial vibration modes we limit the discussion to the symmetric (breathing) mode, in which all helium atoms oscillate radially in phase. The corresponding one-dimensional Schrödinger equation was solved numerically. The eigenenergies of the lowest two vibrational

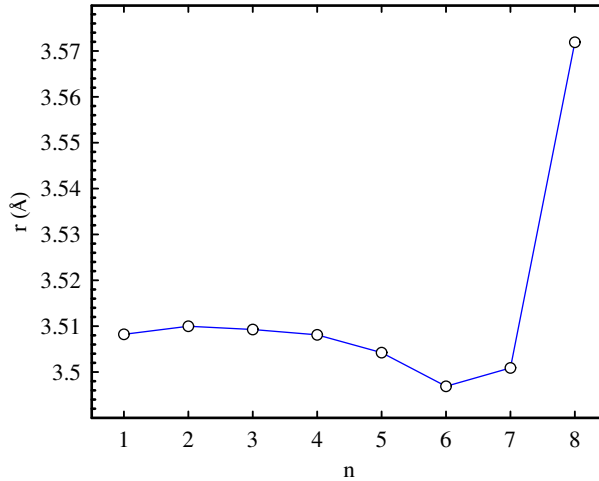


Figure 3.5: Radii of the potential minima for the Cs(A $\Pi_{1/2}$)He_n exciplexes as a function of the number n of helium atoms.

states ($v = 0, 1$) are indicated in Fig. 3.2 and Fig. 3.3 for the cases of Cs*He₂ and Cs*He₆. Note that they are separated by about 60-70 cm⁻¹, which corresponds to 80-100 K, so that in thermal equilibrium at the temperature of the experiments (1.5 K) the higher vibrational states are not populated and can be neglected. We denote the energy of the zero-point oscillation with respect to the potential minimum as $\epsilon_r^{(n)}$. Making the approximation that all other $n - 1$ radial modes have the same zero point energy the total radial oscillation energy becomes $n\epsilon_r^{(n)}$. We denote the wavefunction of the zero-point symmetrical mode by $\Psi_{sym}(r)$.

The diatomic molecule Cs*He₁ has only a single vibrational mode. For Cs*He₂ the modes of θ_i and φ_i vibrations correspond to the two bending modes of a linear triatomic molecule. Both modes have the same energy spectrum and in particular the same zero-point energies $\epsilon_\theta^{(2)}$ and $\epsilon_\varphi^{(2)}$.

For $n \geq 3$ we discuss the polar (θ) and azimuthal (φ) vibration modes separately. There exist $(n - 2)$ θ -modes, since two of the n degrees of freedom ($\varphi_{i=1,\dots,n}$) correspond to rotations around the x and the y axes, defined in standard way by $(\theta = \pi/2, \varphi = 0)$ and $(\theta = \pi/2, \varphi = \pi/2)$ respectively. We treat only the mode parameterized by $\mathbf{r}_i = \mathbf{r}(r_0, \theta = \pi/2 + \delta\theta, \varphi_i = i2\pi/n)$, where $\delta\theta$ is the oscillating angle and r_0 is the distance from the cesium atom where the potential energy is minimal. The zero point eigenenergy $\epsilon_\theta^{(n)}$ was found again by solving a one-dimensional Schrödinger equation with $V_n^{Cs-He}(\delta\theta) = \sum_{i=1}^n V^{6P}(\mathbf{r}_i)$ as potential energy operator. The total polar vibrational energy was then approximated by $(n - 2)\epsilon_\theta^{(n)}$.

There are $(n - 1)$ azimuthal vibration modes. Because of the axial symmetry of the Cs-He potential, only the He-He interactions contribute to the dynamics of the φ -modes. We estimated the energy spectrum of a single mode by making the simplifying assumption that $n - 1$ helium atoms rest at their equilibrium positions, while a single helium atom is allowed to oscillate between its two neighbors on the ring. The potential energy of this oscillation reads

$$V_n^{He-He}(\delta\varphi) = V_{He-He}(2r_0 \sin(\pi/n + \delta\varphi)) + V_{He-He}(2r_0 \sin(\pi/n - \delta\varphi)),$$

where $\delta\varphi$ denotes the oscillation angle. The total zero-point energy resulting from the correspondent Schrödinger equation is then approximately $(n - 1)\epsilon_\varphi^{(n)}$.

The overall zero-point energy, which takes all vibrational modes into account, is finally given by

$$\epsilon_0^{(n)} = n\epsilon_r^{(n)} + (n-1)\epsilon_\varphi^{(n)} + (n-2)\epsilon_\theta^{(n)}. \quad (3.6)$$

The total vibrational energy $\epsilon_0^{(n)}$ is represented as a function of n in Fig. 3.4 as filled circles and has a local minimum for $n = 2$. After the strong increase between $n = 2$ and $n = 3$ the zero-point energy drops slightly until a global minimum is reached for $n = 6$. For larger n the zero point energy of the azimuthal modes increases rapidly.

The results presented here are preliminary. The zero-point energy of the angular vibrational modes leads to centrifugal forces, which were not taken into account in our simplified treatment. This effect will enlarge the radius of the helium ring. However (quasi) bound states will exist only as long as the radius is smaller than the radius of the potential barrier of the radial potentials. The calculations indicate that exciplexes with $n \geq 8$, for which the estimated total zero-point energy exceeds the barrier energy, are unstable (Fig. 3.4). Cs($A\Pi_{1/2}$)He₇ seems to be the largest possible quasi-bound exciplex. Only the energy for $n = 6$ lies 6 cm⁻¹ below the dissociation limit and is hence stable.

The energetic structure of Cs*He_n exciplexes is quite different from Rb*He_n exciplexes, for which the zero-point energies for $n = 1$ to $n_{max} = 7$ are well below the dissociation limit [4]. This is a consequence of the smaller spin-orbit splitting ($\Delta = 237.6$ cm⁻¹) of rubidium compared to cesium ($\Delta = 554.0$ cm⁻¹). As for cesium the rubidium exciplex with $n = 6$ has a minimal energy, but the energy for the $n = 3$ exciplex is in the case of rubidium smaller than for $n = 2$. The minimal energy for $n = 6$ is the key theoretical argument that no rubidium exciplexes with $n > 6$ were observed [4]. All intermediate states ($n = 1\dots 5$) have been observed as transients in the formation of Rb*He₆.

The zero-point energies of the Cs($A\Pi_{3/2}$)He_{*n=1,2*} exciplexes are -80 cm⁻¹ and -139 cm⁻¹ respectively, and hence well below the dissociation limit. The exciplexes Cs($A\Pi_{3/2}$)He₁, Cs($A\Pi_{3/2}$)He₂ and Cs($A\Pi_{1/2}$)He₁ are the only ones previously observed.

3.2.3 The emission spectra

Emission spectra $I(\nu)$ are calculated in the Franck-Condon approximation by

$$I(\nu) \propto \nu^3 \left| \int \Psi(r, \nu) \Psi_{sym}(r) dr \right|^2, \quad (3.7)$$

where ν is the transition frequency and $\Psi(r, \nu)$ is the wave function of the Cs*He_n configuration in the electronic ground state $X\Sigma_{1/2}$. The integrals over the angular variables do not influence the shape of the emission lines, because of the radial symmetry of $\Psi(r, \nu)$. As mentioned above we consider only the wave function of the breathing mode oscillation of the exciplex and assume that the other radial vibration modes have similar wave functions as $\Psi_{sym}(r)$.

Fig. 3.6 shows the calculated emission lines of the Cs($A\Pi_{1/2}$)He_{*n*} exciplexes for $n = 1$ to $n = 7$ and of the Cs($A\Pi_{3/2}$)He_{*n*} exciplexes for $n = 1$ and 2. Only transitions from the vibrational ground states are considered. The red shift of the lines with increasing n is mainly due to the increasing repulsive energy of the ground state potential $nV_\sigma^{6s}(r) + V_n^{He-He}(r)$, while the corresponding broadening is due to the increase of the slope of this potential. The integral intensity of the lines drops with decreasing frequency ν , because of the ν^3 -dependence in 3.7. The asymmetry of the peaks originates from the asymmetric shape of the excited state wavefunction $\Psi_{sym}(r)$ and from the curvature of the ground state potential.

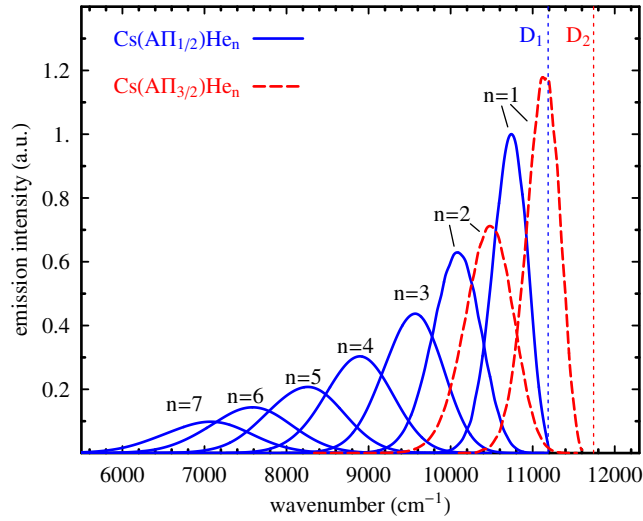


Figure 3.6: Calculated emission lines of the $\text{Cs}(\Pi_{1/2})\text{He}_n$ exciplexes for $n = 1$ to $n = 7$ (solid curves) and of $\text{Cs}(\Pi_{3/2})\text{He}_n$ exciplexes for $n = 1, 2$ (dashed curves). The lines are red-shifted and become broader with increasing number of helium atoms n . The dashed vertical lines indicate the positions of the free atomic D_1 and D_2 emission.

3.3 Experiment

3.3.1 Experimental setup

The experimental setup is illustrated in Fig. 3.7. The experiments were performed in a helium pressure cell immersed in superfluid helium cooled by pumping on the helium bath. Windows provide optical access from three orthogonal directions. A helium crystal is grown inside the pressure cell, by admitting pressurized helium gas from an external reservoir. The helium host matrix is then doped with cesium atoms by means of laser ablation with a pulsed frequency-doubled Nd:YAG-laser beam focussed onto a solid Cs target by a height-adjustable lens above the cell [10]. The temperature is actively stabilized to better than 10^{-5} K [16].

Two tunable light sources were alternatively used to excite the cesium atoms. For experiments with a fixed excitation wavelength we used a single mode cw Ti:AlO₃-laser (Microlase Optical Systems, MBR-110), which can be tuned in the range of 700-900 nm, and which is pumped by a diode pumped Nd:YVO₃ laser. The laser beam is brought to the experiment by means of a single mode, polarization preserving fiber. For recording spectra at variable wavelengths we used an optical parametric oscillator (OPO), (OPTA GmbH, BBO-355-vis/IR), pumped by the third harmonic (354 nm) of a Nd:YAG laser. The latter is pulsed with a repetition rate of 10 Hz. We used the idler beam of the OPO, whose frequency can be tuned over a wavelength range of 719 nm to 2444 nm by rotating the BBO-crystal in the resonator. This tuning process is computer controlled. The laser beam from either source is horizontally polarized and the direction of observation is along the light polarization, thereby minimizing the background from non-resonant scattered light.

The atomic fluorescence light from the sample volume (approx. 3 mm^3) is collimated by a lens in the cryostat and is detected by two alternatively used grating spectrometers. The first detection system is an imaging spectrograph (Oriel, MS257), in which the spectrally dispersed light is detected by means of a CCD camera (Andor, DV420-OE), sensitive from the visible up to 1050 nm. For the detection of longer wavelengths we used an optical spectrum analyzer (Ando Co. Ltd., AQ-6315A) which has a detection range of 350-1750 nm. Since the apparatus

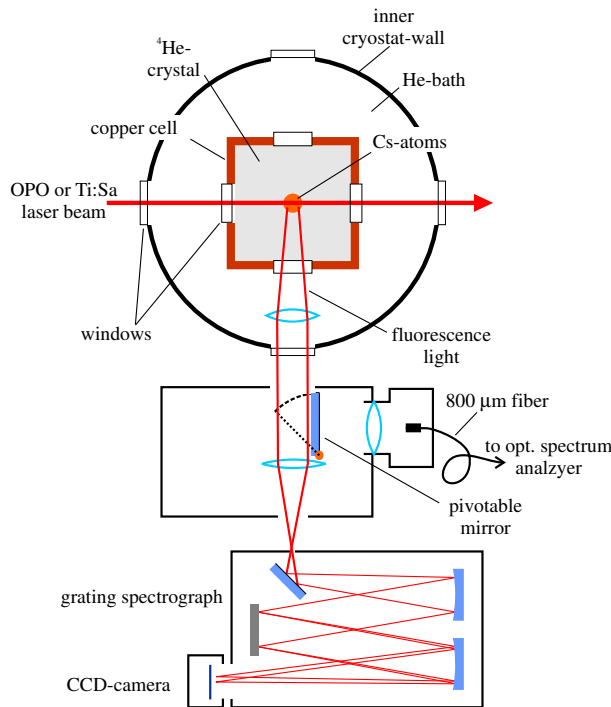


Figure 3.7: Section (top view, not to scale) through the helium containment part of the cryostat and schematic view of the detection optics. The isolation vacuum part and a liquid nitrogen shield are not shown.

has an optical fiber input, the fluorescence light was coupled into an 800 μ fiber. The use of this relatively thick fiber allows us to collect sufficient fluorescence light, but limits the spectral resolution of the device to 5 nm. Compared to the CCD device, which allow the parallel recording of data in a given wavelength range this system has the disadvantage that spectra have to be recorded by time-consuming serial sampling.

3.3.2 Observed emission spectra

All data presented in this section were taken in the hcp phase of solid He^4 at a temperature of $T = 1.5$ K and a pressure of $p = 31.6$ bar.

We first discuss measurements for which the OPO served as the excitation light source and the CCD grating spectrograph was used to record the atomic emission spectra. We scanned the frequency of the idler beam of the OPO in 42 steps of approx. 44 cm^{-1} over a spectral range of 11140 cm^{-1} to 12950 cm^{-1} . At each wave number the light intensity was adjusted to a fixed constant value and an emission spectrum consisting of 1024 data points was recorded with a 5 s exposure of the CCD chip. The actual data points are sums over the vertical image pixel columns of the CCD chip. The combined 42 emission spectra, building an array of 42×1024 data points, are represented as a contour plot in Fig. 3.3.2. The intensity of the recorded light is represented on a logarithmic scale encoded by grey tones as indicated by the legend. All spectra were corrected for the spectral sensitivity of the CCD detector. The representation of Fig. 3.3.2 allows to read off emission spectra (horizontal cuts through the plot) as well as excitation spectra (vertical cuts).

The main features of this two dimensional representation are labelled by **a** to **e**. The diagonal line (**a**) of slope one in Fig. 3.3.2 represents non-resonant scattered light of the OPO. The

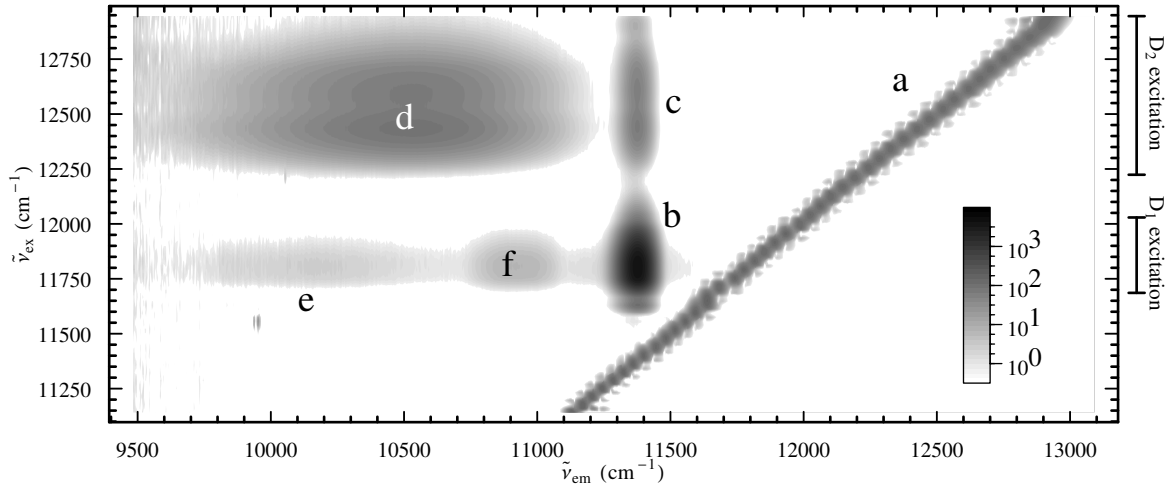


Figure 3.8: Measured fluorescence intensity as a function of the excitation and emission wave numbers ($\tilde{\nu}_{ex}$ and $\tilde{\nu}_{em}$). The strength of the fluorescence is logarithmically encoded as indicated by the gray scales legend in the bottom right corner of the plot. The main features of the diagram are: **a**: non-resonant scattered OPO light, **b**: D_1 emission of atomic cesium following D_1 excitation, **c**: D_1 emission of atomic cesium following D_2 excitation, **d**: emission of $\text{Cs}^*(A^2\Pi_{3/2})\text{He}_2$ exciplexes following D_2 excitation, **e**: emission of $\text{Cs}^*(A^2\Pi_{1/2})\text{He}_2$ exciplexes following D_1 excitation, **f**: an artefact of the CCD camera induced by the saturating peak intensity of **b**. The D_1 and D_2 excitation regions are indicated by bars next to the right ordinate. See the text for further details.

light originates most likely from scattering by cesium clusters located in the sample volume. One distinguishes the 42 different excitation wave numbers of the scan. Atomic emission can be observed at two distinct excitation wave number regions centered around 11800 cm^{-1} and 12500 cm^{-1} respectively, corresponding to the D_1 and D_2 lines of Cs in solid He at the given temperature and pressure. These regions are indicated by bars next to the right ordinate. The most intense peak (**b**) in the diagram represents the D_1 emission from the excited $6P_{1/2}$ state of atomic Cs after excitation on the same transition. The wavelengths of the excitation and emission lines differ as the two processes occur in bubbles of different sizes. The shifts of these lines as well as their asymmetric broadening were studied in detail in the past and are well explained in the frame of the spherical bubble model [2, 17]. The structure (**c**) corresponds to fluorescence from the $6P_{1/2}$ state following excitation of the $6P_{3/2}$ state (D_2 -excitation) indicating the existence of a transfer channel between these states. This process was observed before on Cs in superfluid helium [17] and the feature shown here is its first observation in a solid helium matrix.

The D_2 -excitation spectrum shows a double-peak structure (vertical cut trough feature **c** in Fig. 3.3.2). Such doubly shaped D_2 excitation spectra were also observed for cesium and rubidium in superfluid helium by Kinoshita et al. [18], who showed that the double peak reflects the lifting of m_J level degeneracy of the $6P_{3/2}$ state induced by quadrupolar bubble surface oscillations. The mechanism is analogue to the dynamical Jahn-Teller effect in solid state physics. The result presented here is the first observation of this phenomenon in solid helium.

The prominent feature labelled (**d**) in Fig. 3.3.2 shows a similar doubly shaped excitation structure, as it is also the result of a D_2 excitation. We attribute this broad and asymmetric peak to the emission of $\text{Cs}(A\Pi_{3/2})\text{He}_2$ exciplex, which had previously been observed by the Kyoto group in liquid helium and in cold helium vapor [3]. The faint structure (**e**) around 10160 cm^{-1} can be assigned to the emission of $\text{Cs}(A\Pi_{1/2})\text{He}_2$ exciplexes. The result shown here is the first

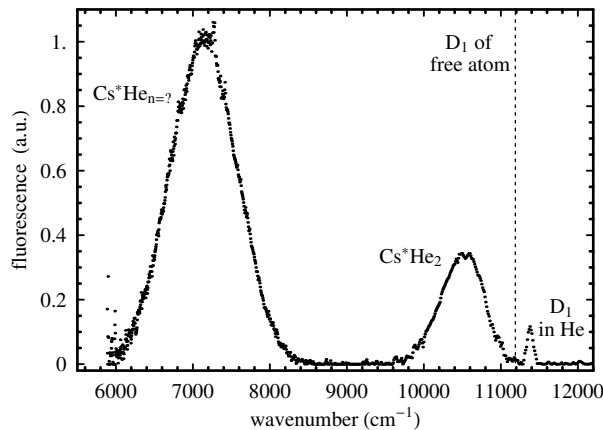


Figure 3.9: Emission spectrum of Cs in solid He⁴. The atoms were excited at 12450 cm⁻¹ to the 6P_{3/2} state of cesium (D₂-line). At 7130 cm⁻¹ we observed a new emission line, which we assign to the decay of Cs(AΠ_{1/2})He_n exciplexes, where *n* is in the range of 5...7. The peak at 10520 cm⁻¹ is identical to the structure **d** in Fig. 3.3.2, and can be unambiguously assigned to the decay of Cs(AΠ_{3/2})He₂. We also observed a weak D₁-emission at 11372 cm⁻¹ as in **c** of Fig. 3.3.2. This line is blue shifted by 191 cm⁻¹ with respect to the free atomic line at 11181 cm⁻¹.

observation of this exciplex, which was neither detected in superfluid helium nor in cold helium gas.

The feature denoted by **f** could be identified as a saturation effect of the CCD camera due to the intense emission peak of the D₁ transition (**b**). Strongly scattered laser light tuned to an arbitrary wavelength causes the same artefact, i.e., a "ghost" peak red shifted by approximately 480 cm⁻¹.

In order to extend the spectral region of the detection we used in a second experiment the Ti-sapphire laser in combination with the Ando optical spectrum analyzer. Fig. 3.9 shows a recorded emission spectrum of 1000 sample points over a wave number range of 6000 to 12000 cm⁻¹, when the Ti-sapphire laser, tuned to 12400 cm⁻¹, excited the cesium atoms to the 6P_{3/2} state. The extended spectral range allowed us the observation of a prominent new emission line at 7130 cm⁻¹, with a linewidth of 1010 cm⁻¹ (FWHM). The peak amplitude is almost three times stronger than the peak at 10520 cm⁻¹. The latter is identical to peak **d** in Fig. 3.3.2 (Cs(AΠ_{3/2})He₂ exciplex emission). This newly found intense emission line at 7130 cm⁻¹ is believed to originate from higher order (*n* > 2) dumbbell-shaped exciplexes (see Sec. 3.4), whereas the small peak at 11372 cm⁻¹ is the D₂ emission of atomic Cs, which corresponds to peak **c** in Fig. 3.3.2.

3.3.3 Pressure dependence of the Cs (6Π_{3/2})He₂ emission line

In yet another experiment we tuned the Ti-sapphire laser again to 12400 cm⁻¹ (D₂ excitation). Starting at *p* = 26.6 bar (bcc phase) the helium pressure in the cell was continuously increased by adding helium from the pressure reservoir. The process was sufficiently slow to keep the temperature at a constant value of 1.57 K. Every ten seconds an emission spectrum was recorded by the CCD camera (0.3 s exposure time). After 100 measurements the pressure was 36.8 bar (hcp phase). From each spectrum the position of the Cs(Π_{3/2})He₂ line was determined. The results are plotted in Fig. 3.10 as a function of helium pressure. The plot also shows two data points near *p* = 0 measured in liquid He II and in cold helium gas by Enomoto et al. [3]. The steep increase of the emission wave number at about 27.5 bar by about 300 cm⁻¹ marks

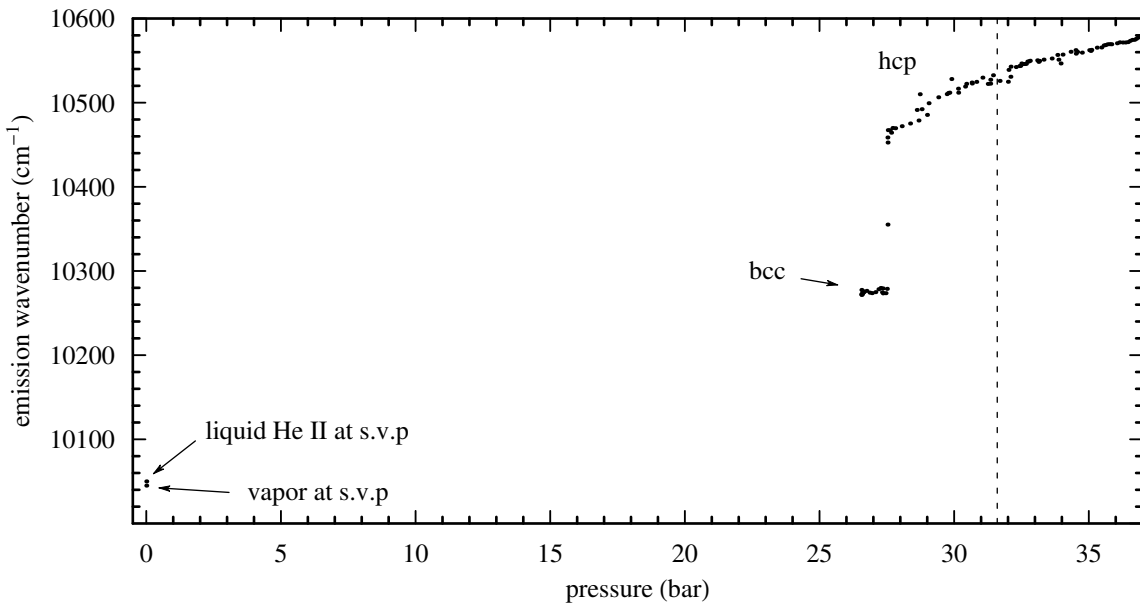


Figure 3.10: Pressure dependence of the $\text{Cs}(6\Pi_{3/2})\text{He}_2$ emission line. The two data points for liquid He II and cold helium vapor (denoted by arrows), measured at 1.6 K and 2.1 K respectively, are taken from [3]. Our data in solid helium were measured at 1.57 K. The dashed vertical line indicates the pressure of 31.6 bar at which the data of Fig. 3.3.2 and Fig. 3.9 were taken.

the phase transition to the hcp phase, in which the wave number increases further at a rate of approximately $10\text{ cm}^{-1}/\text{bar}$. When the data are plotted against the molar density of the helium matrix it can be seen that the jump of the line position at the bcc-hcp phase boundary is not a consequence of the corresponding jump in helium density only.

3.4 Discussion

Figure 3.11 shows again the measured emission spectra of Fig. 3.9 after D_2 excitation at 12450 cm^{-1} , together with theoretical emission spectra of the $\text{Cs}(A\Pi_{3/2})\text{He}_2$ and $\text{Cs}(A\Pi_{1/2})\text{He}_{n=6,7}$ exciplexes calculated according to the procedure discussed in section 3.2. Vertical scaling factors were used to adjust the amplitudes of each of the the calculated lines. In the subsequent paragraphs the assignment of the two measured peaks will be discussed separately.

3.4.1 Cs^*He_2

Let us consider first the peak at 10520 cm^{-1} of Fig. 3.11. There is an apparently excellent agreement between the measured line and the calculated emission line of $\text{Cs}(A\Pi_{3/2})\text{He}_2$ represented by a solid curve. However, this agreement is accidental as the pressure shift discussed in 3.3.3 was not taken into account. In fact the pressure of the bulk helium matrix does not appear as a parameter in our model, which considers the decay of free exciplexes only. The fact that we observe a pressure dependence of the line positions is a clear indication that He matrix influences the exciplex lines. Moreover a pronounced jump in line positions is observed, when going from the bcc to the hcp phase of the matrix, which suggest that not only the atomic bubble, but also its symmetry (isotropic in the case of the bcc phase and uniaxial in the case of the hcp phase) have an influence on the detailed structure of the exciplex emission profiles.

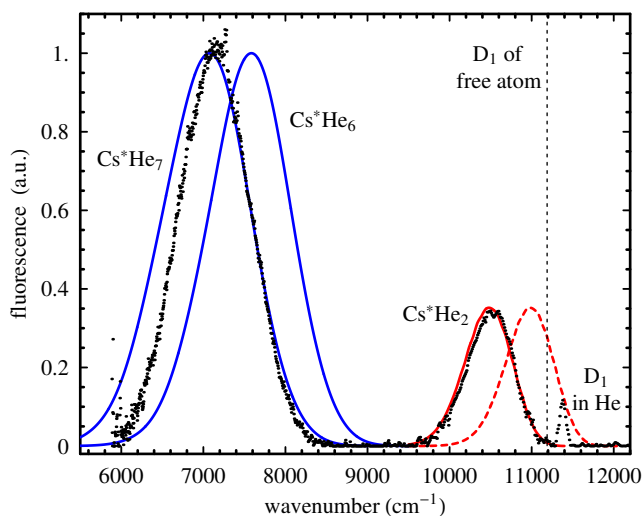


Figure 3.11: The emission spectra of Fig. 3.9 compared with the calculated emission lines for $\text{Cs}(\text{A}\Pi_{3/2})\text{He}_2$ and for $\text{Cs}(\text{A}\Pi_{1/2})\text{He}_n$ with $n = 6$ and 7 . Note that the apparent good agreement of the calculated $\text{Cs}(\text{A}\Pi_{3/2})\text{He}_2$ line (solid curve) with the measured peak is accidental since the influence of the helium matrix onto the emission lines was not taken into account. The pressure dependence measurements (Fig. 3.10) show that at $p = 31.65$ bar the emission line is blue shifted by about 500 cm^{-1} (dashed line) with respect to the low pressure gas value.

From Fig. 3.10 it can be seen that the emission line at $p = 31.6$ bar is blue shifted by about 500 cm^{-1} with respect to the corresponding line in low-pressure helium vapor at 2.1 K . When shifting the calculated line by this amount we obtain the line shown as dashed curve in Fig. 3.11, which does of course disagree with the experimental data. However, the calculated Cs^*He_1 spectra of Enomoto et al. also show a blue shift with respect to their data recorded in cold helium gas [3]. The deviations are between 50 cm^{-1} and 125 cm^{-1} . We may thus speculate, together with the authors of [3], that the discrepancies may be due to a lack of precision in the Cs-He pair potentials. We assume that the discrepancies increase with the number of bound helium atoms.

While the absolute positions are not well reproduced by the calculation the shape and width of the measured line agrees well with the calculated emission line of the $\text{Cs}(\text{A}\Pi_{3/2})\text{He}_2$ exciplex. If one tentatively assigns the observed line to the emission of $\text{Cs}(\text{A}\Pi_{3/2})\text{He}_1$ exciplexes, the calculation yields a line which is narrower and whose position shows an even bigger discrepancy. Another candidate for the observed line would be the $\text{Cs}(\text{A}\Pi_{1/2})\text{He}_2$ exciplex (Fig. 3.2). Its calculated emission line, corrected for the 500 cm^{-1} pressure shift, is 10550 cm^{-1} , which would be in good agreement with the measured line. However, it is unlikely that the formation of $\text{Cs}(\text{A}\Pi_{1/2})\text{He}_2$ exciplexes should be favored in comparison to $\text{Cs}(\text{A}\Pi_{3/2})\text{He}_2$ exciplexes after excitation of the cesium atoms to the $6\text{P}_{3/2}$ state. As mentioned at the end of section 3.2.2, the $\text{Cs}(\text{A}\Pi_{3/2})\text{He}_2$ exciplexes are relatively stable complexes, with an energy well below the dissociation limit and their radial adiabatic potentials have no barrier as the one for the $\text{A}\Pi_{1/2}$ configurations.

Further support for the above assignment comes from the weak line at 10160 cm^{-1} (feature **e** in Fig. 3.3.2) observed following D_1 excitation. The emission peak is red-shifted by 360 cm^{-1} relative to the measured line (feature **d** in Fig. 3.3.2) at 10520 cm^{-1} of Fig. 3.11. The experimental red shift agrees well with the calculated energy difference (395 cm^{-1}) of the $\text{Cs}(\text{A}\Pi_{3/2})\text{He}_2$ and $\text{Cs}(\text{A}\Pi_{1/2})\text{He}_2$ exciplexes (Fig 3.2).

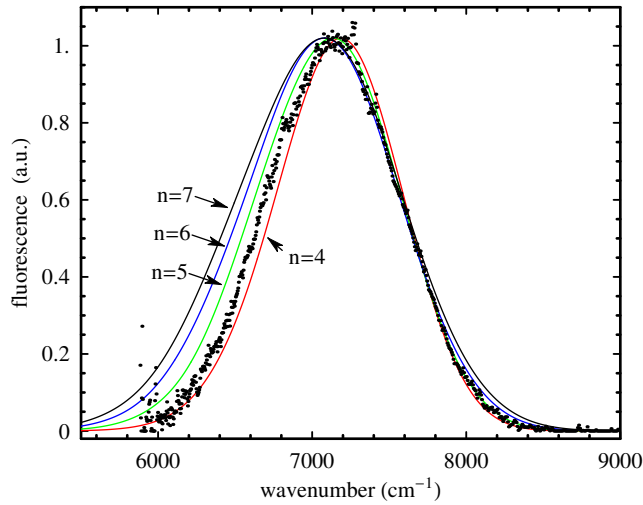


Figure 3.12: Comparison of the line shapes of calculated Cs*He_n emission peaks for $n = 4 \dots 7$ with measured data. The calculated lines were shifted in position so that their right edges coincide approximately with the right edge of the measured peak. The experimental resolution was approximately 25 cm^{-1} .

The relatively weak intensity of the Cs(A $\Pi_{1/2}$)He₂ emission indicates that the formation of these exciplexes is strongly suppressed. This can be explained by the potential barrier of the adiabatic potential (Fig. 3.2) of that state following D_1 excitation. According to the Franck-Condon approximation the radius of the helium bubble ($R_b \approx 7 \text{ \AA}$) does not change during the excitation process to the 6P_{1/2} state. At the ground state bubble radius the excited state potential is repulsive and according to the spherical bubble model the bubble relaxes by increasing its radius to a value of approximately 8.5 \AA . The main decay channel of the P_{1/2} state is via the strong D_1 emission line (feature **b** in Fig. 3.3.2), which is red-shifted with respect to the excitation line. Nonetheless, there is a small probability that a helium atom might tunnel through the potential barrier to form a quasibound Cs*He₁ exciplex with an apple-like shape. As discussed above a second helium atom can then instantly be bound without having to overcome a potential barrier so that a stable Cs*He₂ exciplex is formed.

3.4.2 Cs*He_{n_{max}}

The correct assignment of the measured peak at 7130 cm^{-1} in Fig. 3.11 is a more subtle task. It is clear that the line originates from a Cs(A $\Pi_{1/2}$)He _{$n > 2$} exciplex, in which the helium atoms form a ring in the nodal plane of the Cs atom. It is very likely that this line also shifts with helium pressure. As we have not yet measured the pressure dependence of this line position we cannot apply the pressure correction as for Cs*He₂. With present knowledge we even cannot predict whether the shift is to the blue or to the red because of the different symmetries of the apple-shaped and dumbbell-shaped structures of the two species. Moreover, as the ring-shaped exciplexes contain a larger number of helium atoms any imprecision of the initial pair potentials will be amplified. As a consequence the positions of the higher order Cs*He_n cannot be predicted with a sufficient accuracy to allow an unambiguous assignment of the measured line.

Rather than comparing line positions one can also compare the shapes of calculated and measured emission lines. This is done in Fig. 3.12, where calculated emission spectra of the Cs*He_{4,5,6,7} exciplexes are plotted together with the experimental line. The calculated spectra were scaled and shifted so that the amplitudes and the blue edges of the experimental and

theoretical spectra coincide. One observes that the experimental spectrum lies in between the calculated peaks for $n = 4$ and $n = 5$, whereas the peaks for $n = 6$ and $n = 7$ are definitely broader. However, the widths of the calculated lines are very sensitive to the slope of the $X\Sigma_{1/2}$ ground state potential, so that a lack of precision of the latter will make the assignment of the measured line ambiguous.

An important conclusion can nonetheless be drawn from this comparison. The overall good agreement between calculated and measured lineshapes indicates that the line at 7130 cm^{-1} originates from the decay of an exciplex with a specific number n of bound helium atoms and that it is not a superposition of lines from exciplexes with different values of n . Such superpositions were observed in the case of Rb^*He_n exciplexes in cold He^4 vapor [4]. When decreasing the temperature from 100 K down to 2 K Rb-He exciplexes of increasing n up to $n_{max} = 6$ were observed and identified by these authors. From 100 K down to 40 K mainly Rb^*He_1 was observed, whereas below 5 K only the emission of Rb^*He_6 was detectable. At intermediate temperatures the spectral signal was a superposition of the emission of several neighboring orders, a feature, which allowed the unambiguous assignment of n by simple counting.

The theoretical considerations of Sec. 3.2.2 suggest that the observed peak at 7130 cm^{-1} originates from decaying Cs^*He_6 complexes, as these exciplexes only were found to be stable. The equilibrium radius of the helium ring in that case is approximately 3.5 \AA , and the interatomic He-He interaction was found to be attractive at this radius. Rubidium can bind $n_{max} = 6$ helium atoms on a ring of radius 3.25 \AA [4], and there is no reason to assume that cesium should bind only $n = 4$ or 5 atoms.

However regarding the uncertainties of our calculated spectra no final answer can be given which Cs^*He_n exciplex was observed at 7130 cm^{-1} . Our best guess is Cs^*He_6 at the time being.

3.4.3 Formation of $\text{Cs}^*\text{He}_{n_{max}}$ in solid helium

Cs^*He_n exciplexes with $n > 2$ have not been observed previously, neither in cold helium vapor nor in liquid helium at saturated vapor pressure. Hirano et al. discuss on the basis of Cs^*He_2 -He potential energy surfaces that there is no stable Cs^*He_3 configuration. They therefore conclude that exciplexes with more than $n_{max} = 2$ do not exist, since they regard the formation of exciplexes as a sequential process ($\text{Cs}^* \rightarrow \text{Cs}^*\text{He}_1 \rightarrow \dots \rightarrow \text{Cs}^*\text{He}_{n_{max}}$). However, our experimental results show unambiguously that in the hcp phase of solid helium $\text{Cs}(\text{A}\Pi_{1/2})\text{He}_n$ exciplexes with $n > 2$ are formed, when the atoms are excited to the $6\text{P}_{3/2}$ state of cesium. From the relative integrated observed line intensities (divided by the ν^3 dependence of the transition probabilities) one can conclude that this complex has even the highest steady-state population.

The details of the formation process are not yet understood, considering that the exciplex evolves asymptotically to the $P_{1/2}$ state as $r \rightarrow \infty$ of the free Cs atom, while its formation proceeds via excitation of the $P_{3/2}$ state. The mechanism of the transfer channel from the $\text{A}\Pi_{3/2}$ electronic state to the $\text{A}\Pi_{1/2}$ state is not clear. We can however speculate that due to the solid state density of the surrounding helium, which is many orders of magnitude larger than in He vapor experiments so that the formation does not proceed via sequential capturing of helium atoms.

We can nonetheless ascertain that the formation is such that the $\text{Cs}(\text{A}\Pi_{1/2})\text{He}_{n_{max}}$ structure is formed so rapidly that there is no measurable population in any of the transient intermediate configurations with $3 < n < n_{max}$.

3.5 Summary and outlook

We have performed a study of laser induced fluorescence of cesium atoms trapped in the hcp phase of a helium crystal. The spectral range of both absorption and emission wavelengths was significantly enlarged with respect to previous studies. In addition to the well-studied fluorescence following D_1 excitation we observed a number of new spectral features. We have observed for the first time a weak emission on the D_1 transition following excitation on the D_2 line. As observed before in superfluid helium the corresponding absorption line has a double-peaked structure, due to the dynamic Jahn-Teller effect. In addition we have observed three spectral features, which are broader and partly more intense than the pure atomic lines. We believe that these lines are formed by the emission from two types of specific Cs^*He_n exciplex structures, viz. an apple-shaped complex with two helium atoms bound to the Cs atom and a dumbbell-shaped complex, in which a ring of helium atoms is bound to the nodal plane of the Cs wave function. These assignments are supported by model calculations, which allow us to obtain the corresponding emission spectra. In the case of the ring structure the number of bound atoms cannot be determined unambiguously, but the calculations suggest $n = 6$ as the most likely number of bound atoms. The theoretical treatment is approximative in the sense that it considers only the bound atoms, while neglecting the effect of nearby atoms of the surrounding helium matrix. The matrix affects both the line positions and widths, as evidenced by the experimental observation of a pressure dependence of these two parameters. Ongoing work is supposed to shine more light on this problem, by including spherical and deformed bubbles into the calculation.

On the experimental side we are currently setting up a spectrometer, which extends the previously accessible spectral range towards the red with an improved resolution, so that we can perform a pressure dependent study of the ring-shaped exciplexes.

Acknowledgments

We like to thank J. Pascale for sending us his numerical Cs-He pair potentials. This work was supported by a grant of the Schweizerischer Nationalfonds.

References

- [1] J. Dupont-Roc. Excited p-state of alkali atoms in liquid helium. *Z. Phys. B: Condens. Matter*, 98(3):383–386, 1995.
- [2] S. Kanorsky, A. Weis, M. Arndt, R. Dzierwior, and T. W. Hnsch. Pressure shift of atomic resonance lines in liquid and solid helium. *Z. Phys. B*, 98(3):371–376, 1995.
- [3] K. Enomoto, K. Hirano, M. Kumakura, Y. Takahashi, and T. Yabuzaki. Emission spectra of cs-he excimers in cold helium gas. *Phys. Rev. A*, 66(4):042505, 2002.
- [4] K. Hirano, K. Enomoto, M. Kumakura, Y. Takahashi, and T. Yabuzaki. Emission spectra of rb*he_n exciplexes in a cold ⁴he gas. *Phys. Rev. A*, 68(1):012722, 2003.
- [5] F. Stienkemeier, J. Higgins, C. Callegari, S. I. Kanorsky, W. E. Ernst, and G. Scoles. Spectroscopy of alkali atoms (Li, Na, K) attached to large helium clusters. *Z. Phys. D*, 38(3):253–263, 1996.
- [6] J. Reho, J. Higgins, C. Callegari, K. K. Lehmann, and G. Scoles. Alkali-helium exciplex formation on the surface of helium nanodroplets. I. dispersed emission spectroscopy. *J. Chem. Phys.*, 113(21):9686–9693, 2000.
- [7] J. Reho, J. Higgins, K. K. Lehmann, and G. Scoles. Alkali-helium exciplex formation on the surface of helium nanodroplets. II. a time-resolved study. *J. Chem. Phys.*, 113(21):9694–9701, 2000.
- [8] F. R. Bruhl, R. A. Trasca, and W. E. Ernst. Rb-He exciplex formation on helium nanodroplets. *J. Chem. Phys.*, 115(22):10220–10224, 2000.
- [9] F. Stienkemeier C.P. Schulz, P. Claas. Formation of K*He exciplexes on the surface of helium nanodroplets studied in real time. *Phys. Rev. Lett.*, 87(15):153401, 2001.
- [10] S. I. Kanorsky, M. Arndt, R. Dzierwior, A. Weis, and T. W. Hänsh. Optical spectroscopy of atoms trapped in solid helium. *Phys. Rev. B*, 49(5):3645, 1994.
- [11] Taro Eichler. *Magneto-optical Spectroscopy of Alkali Atoms in Helium Crystals*. Ph.D. thesis, Rheinische Friedrich-Wilhelms-Universität Bonn, 2000.
- [12] R. Müller-Siebert. *Optimierung und Charaktersierung eines Tieftemperatur-Spektrometers zur Untersuchung von magneto- und elektro-optischen Effekten an Alkaliatomen in He-Kristallen*. Ph.D. thesis, Universität Freiburg (Schweiz), 2002.
- [13] D. E. Beck. A new interatomic potential function for helium. *Molecular Physics*, 14(4):311, 1968.
- [14] J. Pascale. Use of l-dependent pseudopotential in the study of alkali-metal-atom-He systems. the adiabatic molecular potential. *Phys. Rev. A*, 28(2):632, 1983.
- [15] Paul Gombás. *Pseudopotentiale*. Springer-Verlag - Wien - New York, 1967.
- [16] R. Müller-Siebert, D. Nettels, and Antoine Weis. To be submitted.
- [17] T. Kinoshita, K. Fukuda, Y. Takahashi, and T. Yabuzaki. Optical properties of alkali-metal atoms in pressurized liquid helium. *Phys. Rev. A*, 52(4):2707, 1995.

- [18] T. Kinoshita, K. Fukuda, and T. Yabuzaki. Doubly shaped D_2 excitation spectra of Cs and Rb atoms in superfluid helium due to a quadrupole bubble surface oscillation. *Phys. Rev. B*, 54(9):6600–6607, 1996.

Chapter 4

Multiphoton processes in the Zeeman structure of atomic Cs trapped in solid helium

D. Nettels, R. Müller-Siebert, S. Ulzega , and A.Weis

Département de Physique, Université de Fribourg, Chemin du Musée 3, 1700 Fribourg, Switzerland

accepted for publication by *Appl. Phys. B*

Abstract: We report on magnetic resonance experiments with optical detection performed on cesium atoms trapped in a crystalline ^4He matrix. Multi-photon transitions, i.e. processes in which several radio-frequency photons are absorbed simultaneously in a given hyperfine Zeeman multiplet of the ground state were the central topic of these studies. The long relaxation times of spin coherences of Cs in solid He allow to spectrally resolve such transitions in fields as low as 1 mT. We have observed all allowed multi-photon transitions up to the $\Delta M = 8$ transition in the $F = 4$ -state. We compare the experimental spectra with theoretical spectra obtained from numerical solutions of the Liouville equation including optical pumping and the interaction with the static and oscillating fields. Multi-photon transitions may find application in magnetometry, suppress systematic effects in edm experiments and may allow the study of relaxation phenomena in doped He crystals. The demonstration of these features is still hindered by inhomogeneous line broadening.

4.1 Introduction

Since the pioneering work of Kastler and Brossel in 1949 [1] double resonance experiments, which combine magnetic resonance spectroscopy with resonant optical preparation and detection have found a large range of applications, to mention only optically pumped magnetometers

and the search for permanent electric dipole moments (edm) of atoms. This double resonance technique is also known as optically detected magnetic resonance (ODMR). In this work we have investigated multi-photon effects in double resonance spectroscopy, i.e., processes, in which several radio-frequency (r.f.) photons are absorbed simultaneously. We report on the first observation of such processes in atoms trapped in a solid helium matrix. This unique sample is well suited for the study of such processes, as the trapped atoms have long relaxation times, so that the multi-photon lines are already well split in a relatively modest magnetic field of 1 mT.

The present study is motivated by the perspective that multi-photon spectra may allow to measure line shifts induced by external perturbations with an increased sensitivity. Obvious applications are magnetometry, sublevel Stark spectroscopy and edm experiments. As shown at the end of the paper specific multi-photon transitions allow furthermore to suppress a commonly encountered systematic effect in edm-experiments.

The detailed structure of multi-photon spectra depends on the nature of the relaxation processes of the involved multi-quantum coherences. From high precision experimental spectra it is thus, in principle, possible to identify the underlying relaxation mechanisms. This is particularly interesting for a better understanding of the symmetries and dynamics which govern the spin relaxation of guest atoms in quantum crystals. So far there is only very restricted knowledge on this topic. The control of field inhomogeneities is a major issue in this type of multi-photon spectroscopy. Model calculations, which include field inhomogeneities yield a good description of the observed spectra.

4.1.1 Akali-doped helium crystals

Since a number of years we have performed ODMR experiments on alkali atoms trapped in helium crystals. This unique sample has some outstanding properties due to the quantum nature of the host crystal. A main feature is the very high degree of spherical symmetry of the local trapping sites of the embedded impurity atoms (atomic bubbles), which is a consequence of the Pauli principle and the high elasticity of the isotropic helium quantum solid. The non-magnetic nature of the host matrix atoms and their isotropic distribution around the defect atoms ensure that alkali spins are only very weakly perturbed, which is reflected by longitudinal spin relaxation times $T_1 = 1/\gamma_1$ of $\langle J_z \rangle$ on the order of 1 second [2] and by the observation of very narrow magnetic resonance lines [3]. Although the helium matrix strongly broadens and shifts optical absorption and emission lines [4], the sample can be polarized by optical pumping [5], which makes this unusual sample well suited for high resolution ODMR studies.

4.1.2 Multi-photon transitions

In most applications ODMR experiments deal with processes in which individual r.f. photons interact with adjacent sublevels $|F, M\rangle$ and $|F, M \pm 1\rangle$ according to the selection rules for magnetic dipole transitions. We limit our discussion to transitions between sublevels $|F, M\rangle$ in an isolated hyperfine level. When the intensity of the r.f. field, characterized by the Rabi frequency Ω describing the strength of the spin-field coupling becomes very large nonlinear processes in which several r.f. photons are absorbed simultaneously by the system get a sizable probability. One distinguishes two classes of such processes which appear at different values of Ω .

When Ω becomes comparable to the Larmor frequency ω_L , the rotating wave approximation (r.w.a.) loses its validity and one can observe $\Delta M = \pm 1$ transitions involving the simultaneous absorption of several r.f. quanta [6]. In this paper we focus, however, on another class of multi-photon transitions, namely processes, in which transitions between sublevels whose magnetic quantum numbers differ by $\Delta M = \pm N$ are driven by the simultaneous absorption of N radio-frequency quanta. Resonances involving $N = 1, 2, \dots$ photons appear in sequential order as

the Rabi frequency Ω is increased. These processes set on when Ω becomes comparable to the coherence relaxation rate γ_2 of the coupled levels. As in general $\gamma_2 \ll \omega_L$ this second class of phenomena appears for smaller intensities than the first class.

Multi-photon transitions of the second type were analyzed theoretically in [7, 8, 9] using an algebraic approach. The first experimental observations of such processes involving two- and three-photons in the r.f. spectra of O₂ and K were performed by Kusch 50 years ago [10] and in Cs in 1957 by Skalinsky [11]. Numerical calculations for K, Li and Cs [12, 13] and experimental studies for K were performed by Alexandrov and coworkers [14] using an ODMR technique. Xu et al. [15] have given an interpretation of multi-photon transitions in terms of atomic multipole moments, to describe experiments in the time-domain on rubidium and cesium atoms in the vapor phase using r.f. pulse sequences. Several references to the role of multi-quantum transitions in NMR studies are also given by these authors.

4.2 Multi-photon transitions

4.2.1 Basics

In a small magnetic field B_0 an isolated hyperfine multiplet of total spin F splits into a series of $2F + 1$ magnetic sublevels which can be labelled by their zero-field quantum numbers $|F, M\rangle$. As we restrict our discussion to the ground state hyperfine level F of cesium the notation $|F, M\rangle$ is a short-hand writing for $|6^2S_{1/2}; F, M\rangle$. The frequency difference of adjacent levels is $\omega_{M+1, M} = \omega_{M+1} - \omega_M = \omega_L$, where $\omega_L = \gamma B_0 = g_F \mu_B B_0 / \hbar$ is the Larmor frequency of the level characterized by the Landé-factor g_F . Radio-frequency transitions between these levels obey the magnetic dipole transition rules $\Delta M = \pm 1$, so that a circularly polarized r.f. field of a given handedness can excite $2F$ individual transitions, provided that the coupled states have non-zero population differences. In a weak magnetic field (linear Zeeman effect) all the transition frequencies $\omega_{M+1, M}$ are identical and the magnetic resonance spectrum consists of a superposition of $2F$ unresolved resonance lines centered at the same resonance frequency ω_L .

In order to resolve these $2F$ lines one needs an interaction, which yields a level shift, which is nonlinear in M . The Breit-Rabi interaction is one way to realize this condition. The lowest order correction of the linear Zeeman effect due to the hyperfine interaction can be parameterized as

$$\omega_M = \omega_{hfs}^F + \gamma M B_0 + (\alpha + \beta M^2) B_0^2, \quad (4.1)$$

where ω_{hfs}^F is the hyperfine frequency shift of the given hyperfine level F , α and β are constants depending on the specific state. As a consequence the one-photon resonance frequencies no longer overlap and the magnetic resonance spectrum consists of $2F$ equidistant lines (Fig. 4.1, $N = 1$). A similar pattern of lines is also obtained in the linear Zeeman regime when an additional interaction yielding level shifts proportional to M^2 is present, such as a perturbation with quadrupolar symmetry, as, e.g., the quadratic Stark effect related to the tensor polarizability. In addition to processes in which a single r.f. photon is absorbed, processes in which N identical r.f. photons are absorbed simultaneously are possible. For an r.f. field of a given handedness the selection rules for such processes require $\Delta M = \pm N$, where the sign is determined by the sign of the corresponding population difference. The resonance frequency of a $\Delta M = N$ -photon transition starting from a level M is given by

$$\frac{\omega_{M+N} - \omega_M}{N} = \gamma B_0 + \beta B_0^2 (2M + N). \quad (4.2)$$

For instance, for $N = 2$ there are $2F - 1$ distinct such transitions (Fig. 4.1, $N = 2$). Their resonance frequencies are centered exactly in the middle of the intervals separating adjacent one-photon lines (Fig. 4.2). As these transitions are higher order processes their onset can only be

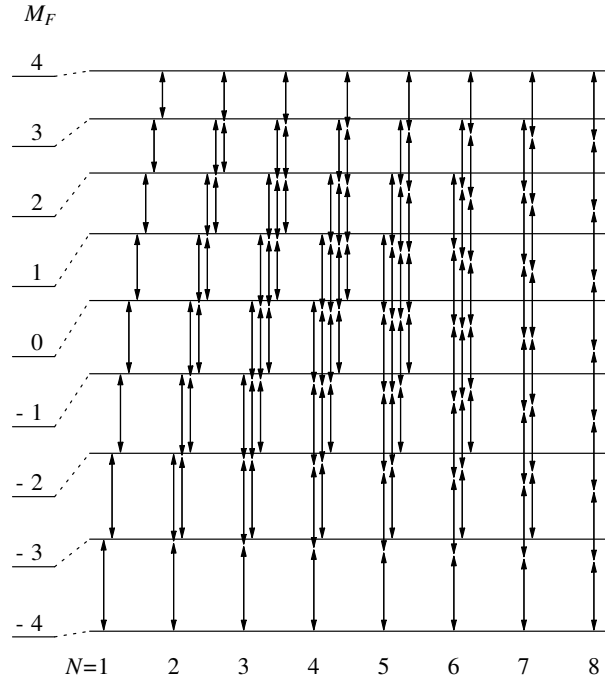


Figure 4.1: Level scheme of the ground-state $F = 4$ hyperfine Zeeman multiplet. The linear (left) and quadratic (right) Zeeman splittings are shown separately. Arrows indicate the $(2F + 1 - N)$ N -photon transitions, where $2F + 1$ is the number of magnetic substates.

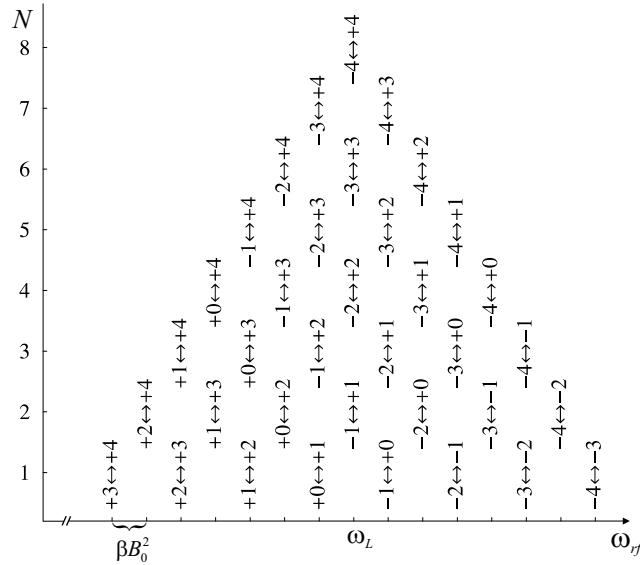


Figure 4.2: Frequency distribution of the multi-photon resonance frequencies for the $N = 1 \dots 8$ -photon transitions $M \leftrightarrow M + N$ of a $F = 4$ system. The positions of the resonances are given by Eq. 4.2 with $\beta < 0$ as for Cs.

observed at larger r.f. intensities. At still higher r.f. intensities the magnetic resonance spectrum will show the appearance of $2F - 2$ three-photon transitions whose resonance frequencies will coincide again with the one-photon resonances. The further increase of the r.f. intensity will show increasingly higher orders until finally a single ($N = 2F$)-photon line appears, which corresponds

to the $\Delta M = 2F$ transition coupling the states $|F, M = +F\rangle$ and $|F, M = -F\rangle$. All even order resonances occur at a given set of equidistant frequencies, while the odd order resonances are also degenerate among themselves, but at a shifted set of frequencies (Fig. 4.2). It is to be noted that a given generation of N -photon lines appears on a power-broadened background of lower order ($N' < N$) resonance lines.

In the following we will restrict the discussion to the ground state of ^{133}Cs whose hyperfine structure consists of two levels with $F = 3$ and $F = 4$ respectively. Fig. 4.2 illustrates the positions of the allowed multi-photon lines for the $F = 4$ state of cesium.

4.2.2 Resonance frequencies in the ground state of ^{133}Cs trapped in the b.c.c. phase of solid ^4He

The hyperfine structure of the $6S_{1/2}$ -ground state of ^{133}Cs ($I = 7/2$) in a field B_0 is described by the hamiltonian

$$H_0 = A \mathbf{I} \cdot \mathbf{J} + g_J \mu_B J_z B_0 - g_I \mu_B I_z B_0, \quad (4.3)$$

where $A = A(6S_{1/2})$ is the hyperfine coupling constant of the ground state, g_J and g_I are the electronic and nuclear g-factors respectively and μ_B is the Bohr magneton. The corresponding eigenvectors are $|(F_{\pm}), M\rangle$. The brackets around $F_{\pm} = I \pm J = 3, 4$ indicate that F is not a good quantum number in presence of the magnetic field, but that it may still serve as a state label. The solutions of this eigenvalue problem, known as the Breit-Rabi formula [16], were used for the numerical calculation discussed in section 4.2.4. After expanding the energy eigenvalues up to second order in B_0 one gets for the parameters in Eq. 4.1 of the states F_{\pm}

$$\begin{aligned} \omega_{hfs}^{\pm} &= \frac{-1 \pm 8 A}{4 \hbar}, \\ \alpha_{\pm} &= -16 \beta_{\pm}, \\ \beta_{\pm} &= \mp \frac{(g_J + g_I)^2 \mu_B^2}{256 \hbar A}. \end{aligned}$$

Inserting the vacuum values for A and the g-factors of the ^{133}Cs ground state gives $\beta = 2\pi 1.336 \text{ kHz/mT}^2$. However, the hyperfine constant A of Cs implanted in the b.c.c. phase of solid ^4He is blue shifted due to the compression of the $6S_{1/2}$ wave function by the He matrix [17]. At $T = 1.507 \text{ K}$ and $p = 26.67 \text{ bar}$ it is increased by 2.136(1)% with respect to its vacuum value. This yields $\beta = 2\pi 1.308 \text{ kHz/mT}^2$. The latter value has to be used in the model calculations, in order to reproduce the positions of the experimentally observed lines.

The field dependence of the resonance frequencies of the single quantum magnetic dipole transitions is shown in Fig. 4.3. For better visualization the resonance frequency $\Delta\nu_{ref}$ of the $|(4), 3\rangle \rightarrow |(4), 4\rangle$ transition was subtracted. In very low fields (linear Zeeman regime) the resonance frequencies split into two groups of lines, where the frequencies are degenerate within each group. The two groups correspond to $F = 3$ and $F = 4$ respectively, whose g_F -factors

$$g_{F_{\pm}} = \pm \frac{1}{8} g_J - \frac{8 \mp 1}{8} g_I$$

differ because of nuclear magnetism. The g-factors of Cs in the b.c.c. phase of solid helium were shown previously to coincide with the ones of the free atom at a level of at least 10^{-4} [18]. In larger fields this degeneracy is lifted by the quadratic Zeeman effect thus producing the line pattern necessary for the observation of resolved multi-photon-transitions. In the $F = 4$ state there will thus be in general 8 one-photon lines, 7 two-photon lines, 6 three-photon lines, up to a single eight-photon line connecting the states $|(4), -4\rangle$ and $|(4), +4\rangle$. As mentioned before, the observability of these lines depends on the existence of suitable population differences.

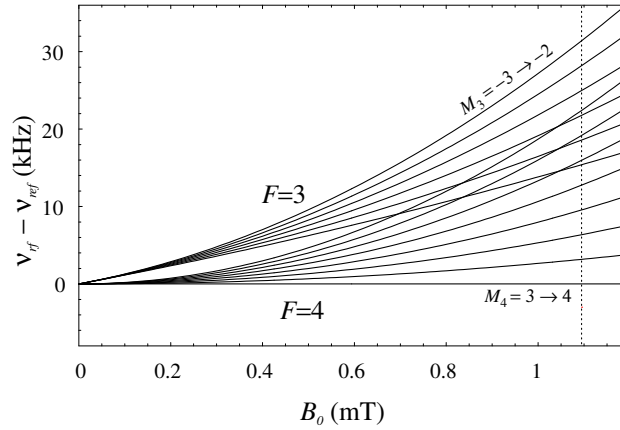


Figure 4.3: Resonance frequencies $\Delta\nu_{(F_{\pm}),M,M+1}$ of the $|(F_{\pm}), M\rangle \rightarrow |(F_{\pm}), M+1\rangle$ transitions in the ground state of Cs. The resonance frequency $\Delta\nu_{ref} = \Delta\nu_{(4),3,4}$ is subtracted in order to visualize the lifting of degeneracies due to the nuclear magnetism and the quadratic Zeeman effect. $\Delta\nu_{ref}(\text{MHz}) \approx 3.5 B_0(\text{mT})$. The dotted line indicates the field at which the experiments were performed.

4.2.3 Optical Detection

So far we have discussed merely the magnetic resonance proper, without addressing its experimental detection. In our experiments a circularly polarized laser beam resonant with the Cs D_1 -transition was used for this purpose. The interaction with the laser beam is used to prepare the necessary population differences in the magnetic sublevels by optical pumping. At the same time the scattering rate of the laser radiation depends on the degree of spin polarization of the medium. As the magnetic resonance transitions affect this polarization the fluorescence rate is a convenient monitor of the magnetic resonance process. This is the very essence of ODMR. Optical pumping and magnetic resonance of Cs in solid helium was studied extensively by Lang et al. [5].

The D_1 -absorption line of Cs in the b.c.c. phase of ^4He is shifted from its vacuum value at 894 nm to approximately 850 nm in solid ^4He , whereas the emission line is shifted to 888 nm. The homogeneous width of the absorption line is 11 nm [19], which exceeds the hyperfine splittings in both the ground and excited states by several orders of magnitude, so that the hyperfine structures of the states are not resolved in the optical spectra. Because of this large homogeneous width the intensity of the optical field (typically 10 mW/cm^2) is too low to induce stimulated emission.

4.2.4 Numerical calculations

We have calculated the multi-photon ODMR spectra of Cs by numerically solving the steady-state Liouville equation for the density matrix ρ describing the 16 sublevels of the $6S_{1/2}$ ground state hyperfine structure. The rate of change of the matrix elements of ρ is governed by their interaction with the (static and oscillating) magnetic fields, the interaction with the circularly polarized light field inducing optical pumping and by spin coherence relaxation processes. The calculations were performed in the $|(F), M\rangle$ basis in which H_0 of Eq. 4.3 is diagonal. Since the two hyperfine levels are well separated in energy, it is justified to neglect all matrix elements which couple states of different F -values. This reduces the number of coupled equations to be solved to 130.

The calculation assumes optical pumping of the atoms with circularly polarized D_1 reso-

nance radiation in a longitudinal external magnetic field B_0 . Since the pumping process is non-saturating the excited state coherences and populations can be eliminated adiabatically. The optical pumping mechanism is parameterized by the pump rate γ_p defined in [5]. The radio-frequency field, linearly polarized perpendicular to B_0 , is assumed to interact with the ground state magnetic moments in the rotating wave approximation. Our calculation is similar to the treatment given before by Pazgalev and Alexandrov [13]. However we have corrected for their simplifying assumption that the Rabi frequencies of the magnetic dipole transitions are independent of the magnetic quantum numbers M . Here we have used relative r.f. transition amplitudes as given by Racah algebra. In the calculations we have furthermore assumed that the ground state populations relax with a common rate γ_1 towards a thermal equilibrium distribution determined by the Boltzmann factor $\exp(-h\Delta\nu_{hfs}/k_B T) \approx 0.75$, where $\Delta\nu_{hfs} \approx 9.39\text{MHz}$ is the hyperfine splitting in the ground state of Cs in b.c.c. He, and $T \approx 1.5\text{ K}$ typically. The mathematical treatment of the optical pumping process is such that the perturbation of the coherences due to the interaction with the light field is properly taken into account. Details of these calculations will be published elsewhere [20].

The numerical steady-state solutions of the Liouville equations then yield the populations $p_{F,M}$ of the 16 ground state sublevels and the fluorescence signal can be obtained by calculating the absorption of circularly polarized light by this population distribution.

4.3 Experiment

4.3.1 The experimental set-up

The experimental set-up (Fig. 4.4) is similar to the one described in [5]. The experiments were performed in a helium pressure cell immersed in superfluid helium cooled by pumping on the helium bath. Five quartz windows, flanged onto the cell using aluminum sealing rings, provide optical access from three orthogonal directions. A helium crystal is grown inside the pressure cell, by admitting pressurized helium gas from an external reservoir. The helium host matrix is then doped with cesium atoms by means of laser ablation with a pulsed frequency-doubled Nd:YAG-laser beam focussed onto a solid Cs target by a height-adjustable lens above the cell. The bath and cell temperatures are measured by germanium resistors located inside and outside of the pressure cell. A novel feature of the setup is an active temperature stabilization of the He crystal by a feed-back loop that regulates the pump speed via a motor-driven valve. A stability on the order of 10^{-5} K over intervals of 100 seconds could be realized in this way [21].

The cesium atoms are excited on the D_1 transition ($6S_{1/2} \rightarrow 6P_{1/2}$) at 850 nm with a beam from a temperature and current stabilized single-mode extended cavity diode laser. The absorption is monitored by detecting fluorescence light at 888 nm using a cooled, biased avalanche-photodiode. An interference filter (FWHM of 9 nm) suppresses scattered laser light by four orders of magnitude. The pressure cell is surrounded by three orthogonal pairs of Helmholtz coils to apply the static magnetic field and to compensate residual fields. Another set of three Helmholtz coils inside the pressure cell is used to apply the r.f. fields. Three layers of μ -metal surround the cryostat and suppress laboratory magnetic fields by more than three orders of magnitude.

4.3.2 Experimental results

Data were taken in the body-centered cubic (b.c.c.) phase of solid ^4He at a temperature of 1.507 K and a pressure of 26.67 bar in a field B_0 of 1.0947 mT.

Magnetic resonance spectra were recorded by detecting fluorescence while scanning the frequency of the r.f. field over the multiphoton resonances of the $F = 3$ and $F = 4$ multiplets.

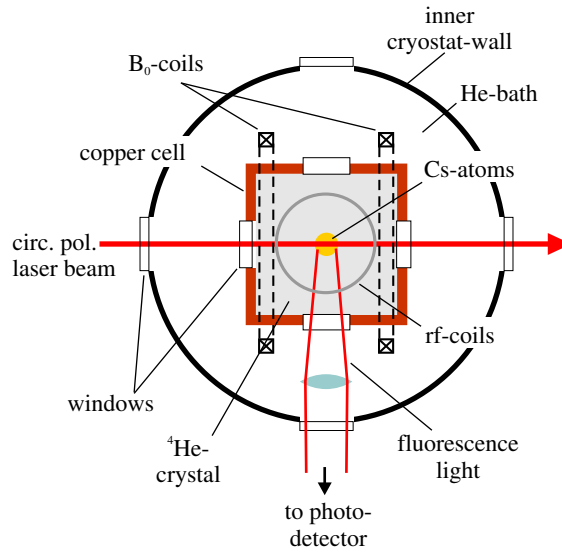


Figure 4.4: Section (top view, not to scale) through the helium containment part of the cryostat. The isolation vacuum part and a liquid nitrogen shield are not shown.

Distortions of the spectral line shapes were minimized by choosing scan speeds of 20 seconds per scan. The frequency sweeps were centered at 3830.1 kHz with a span of 50 kHz. The results are shown in Fig. 4.6 a. As a typical example a detailed view of the spectrum with the lowest r.f. power (bottom curve of Fig. 4.6) is presented in Fig. 4.5. Here the amplitude of the r.f. field was approximately $B_{rf} \approx 45$ nT. The strongest line in the spectrum is the power-broadened $|(4), 4\rangle \rightarrow |(4), 3\rangle$ one-photon transition, while the third resonance from the left is the $|(4), 3\rangle \rightarrow |(4), 2\rangle$ one-photon transition. The resonance in between these two lines marks the onset of the $|(4), 4\rangle \rightarrow |(4), 2\rangle$ two-photon transition. Fig. 4.6 shows the evolution of this spectrum as the r.f. power is increased. As anticipated above the evolution of the spectra obeys the following repetitive pattern: saturation and broadening of the N -photon resonances and simultaneous onset of the $N+1$ -photon lines. In the top spectrum the 8-photon transition connecting the states $|(4), 4\rangle$ and $|(4), -4\rangle$ alone is visible, superposed on the broad background from the 35 unresolved power-broadened $N=1..7$ resonances. For better readability successive spectra in Fig. 4.6 were each offset vertically by 0.1. The dimensionless units on the ordinate axis represent the normalized change of the fluorescence induced by the r.f. interaction with respect to the fluorescence observed in absence of that interaction. This representation allows the comparison of experimental and theoretical spectra on an absolute scale.

The spectra displayed in Fig. 4.6 represent background-corrected data. In the raw data the multiphoton peaks are superposed on a monotonous decreasing fluorescence background signal, which is due to the loss of atoms by the recombination of implanted Cs atoms with clusters and other Cs atoms during the r.f. sweep. The time scale of this process is on the order of tens of seconds as described in [5]. In order to dissociate these clusters we apply before each r.f. frequency sweep a weak pulse of Nd:YAG-laser radiation focused into the Cs doped volume. This background signal was recorded in separate runs, in which no r.f. field was applied to the sample. An appropriate model function was used to fit the shape of this background signal and the raw data were subsequently divided by this fitted background curve. This procedure did not only remove the background, but it also served to renormalize the ODMR spectra proper, thus correcting for an apparent signal decrease towards increasing r.f. frequencies due to the time dependent loss of atoms.

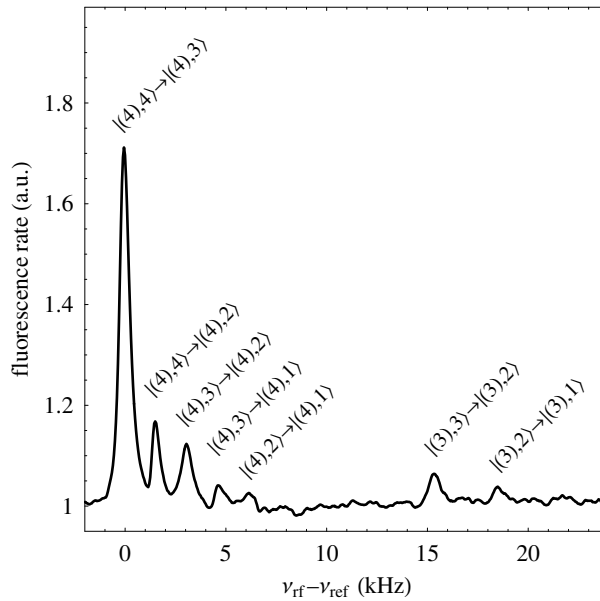


Figure 4.5: Detailed view of the bottom spectrum of Fig. 4.6. See text.

Under strong pumping ($\gamma_p \gg \gamma_1$) with perfect circular polarization all atoms would be pumped to the dark $|4, 4\rangle$ state, which does not couple to the light field. The magnetic resonance spectra involving N photons would then consist of the $|4, 4\rangle \rightarrow |4, 4 - N\rangle$ transitions only. However, due to the finite laser power, to ground state relaxation processes and to imperfections of the light polarization (before reaching the atoms the laser beam traverses four optical windows, some of which have a pronounced stress induced birefringence) also lower M -states as well as states of the $F = 3$ multiplet are populated. In all multi-photon spectra the $|4, 4\rangle \rightarrow |4, 4 - N\rangle$ lines represent nonetheless the dominant spectral features in comparison to the adjacent $|4, 3\rangle \rightarrow |4, 3 - N\rangle$ and $|4, 2\rangle \rightarrow |4, 2 - N\rangle$ lines.

4.3.3 Comparison with calculations

In Fig. 4.7 we show the results of the numerical calculations according to the procedure discussed in section 4.2.4. Several parameters, viz. B_0 , B_{rf} , γ_1 , the optical pumping rate γ_p , and a parameter characterizing the degree of circular polarization of the laser beam enter these calculations. Three of the parameters (γ_1 , γ_p and the degree of circular polarization) could be deduced from earlier experiments. The longitudinal spin relaxation rate γ_1 was measured to be $\gamma_1 = 0.9 \text{ s}^{-1}$ [5]. B_0 cannot be measured with sufficient accuracy using standard magnetometers under cryogenic conditions. By fitting Lorentzians to the multi-photon spectra we therefore inferred B_0 from the line positions in accordance with the Breit-Rabi formula taking the perturbation of the hyperfine constant by the helium matrix into account. As our model neglects the transverse spin relaxation γ_2 the line widths are determined by r.f. power broadening and optical pumping. The calculation uses the same relative r.f. field amplitudes B_{rf} as those used in the experiment. However, a precise absolute calibration of B_{rf} inside the pressure cell was not possible and the calibration constant was empirically determined by a qualitative fit of the calculated spectra to the experimental ones.

The overall structure of the ODMR spectra is well reproduced by the calculations, even on an absolute scale. However, the widths of the calculated multi-photon resonances at their

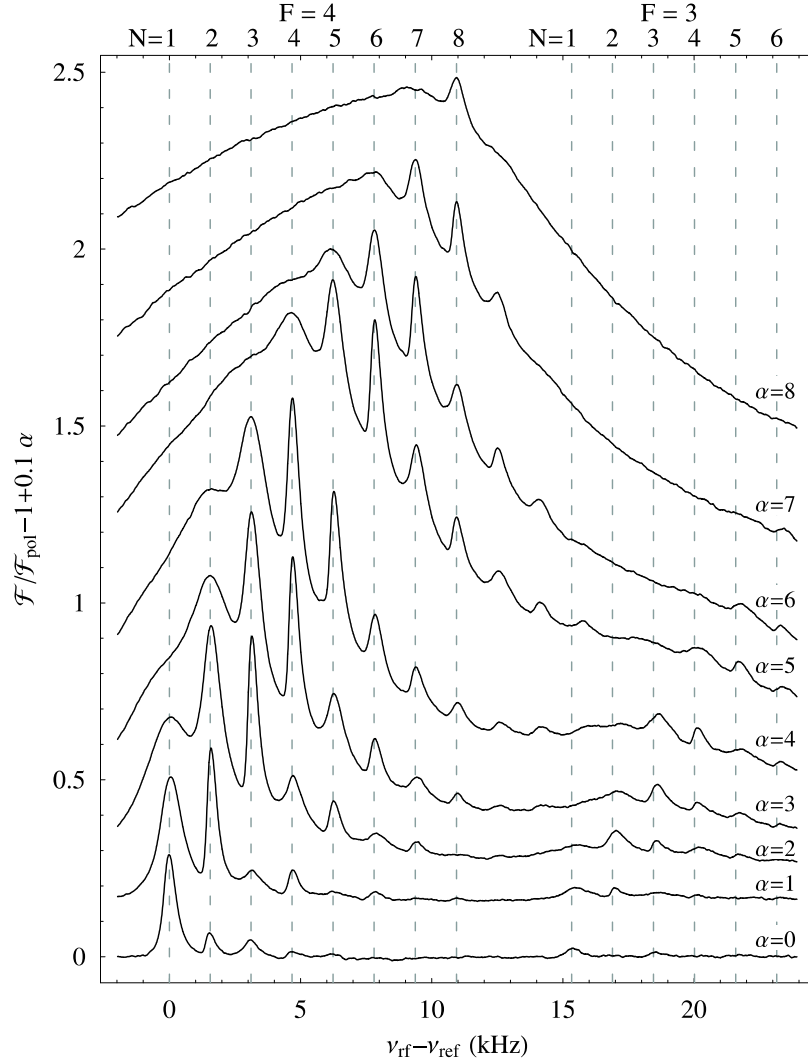


Figure 4.6: Background corrected (see text) measured multiphoton resonance spectra in a field B_0 of 1.0947 mT. The origin of the frequency axis corresponds to the frequency of the $|4, 4\rangle \rightarrow |4, 3\rangle$ one-photon transition ($\nu_{\text{ref}} = 3818.78$ kHz). The corresponding relative r.f. field amplitudes for the subsequent spectra were (bottom to top) 1:3:8:16:23:46:65:91:129. Dashed lines indicate the positions of the N -photon resonances $|4, 4\rangle \rightarrow |4, 4 - N\rangle$ and $|3, 3\rangle \rightarrow |3, 3 - N\rangle$ respectively. Each spectrum is the average over five individual scans. Successive curves are labeled by α and offset from the preceding one by 0.1.

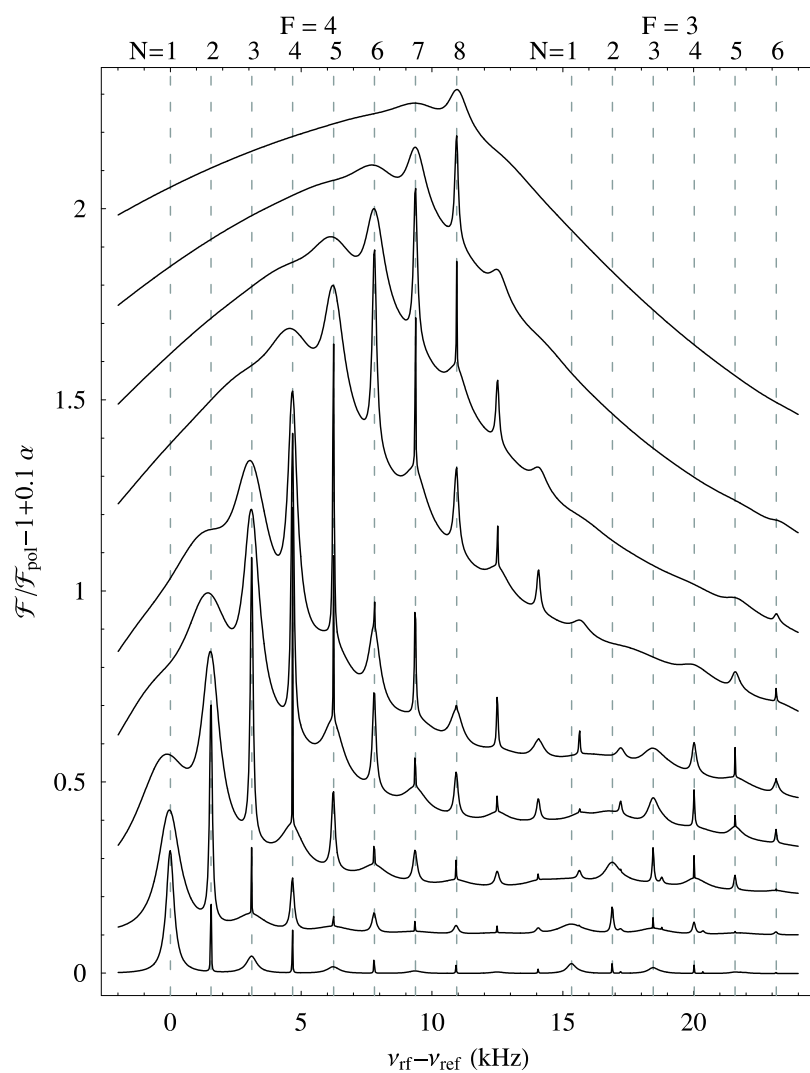


Figure 4.7: Calculated multiphoton resonances yielded by solving the steady-state Liouville equation for the density matrix ρ describing the 16 sublevels of the $6S_{1/2}$ ground state hyperfine structure as discussed in section 4.2.4. Details are given in the text.

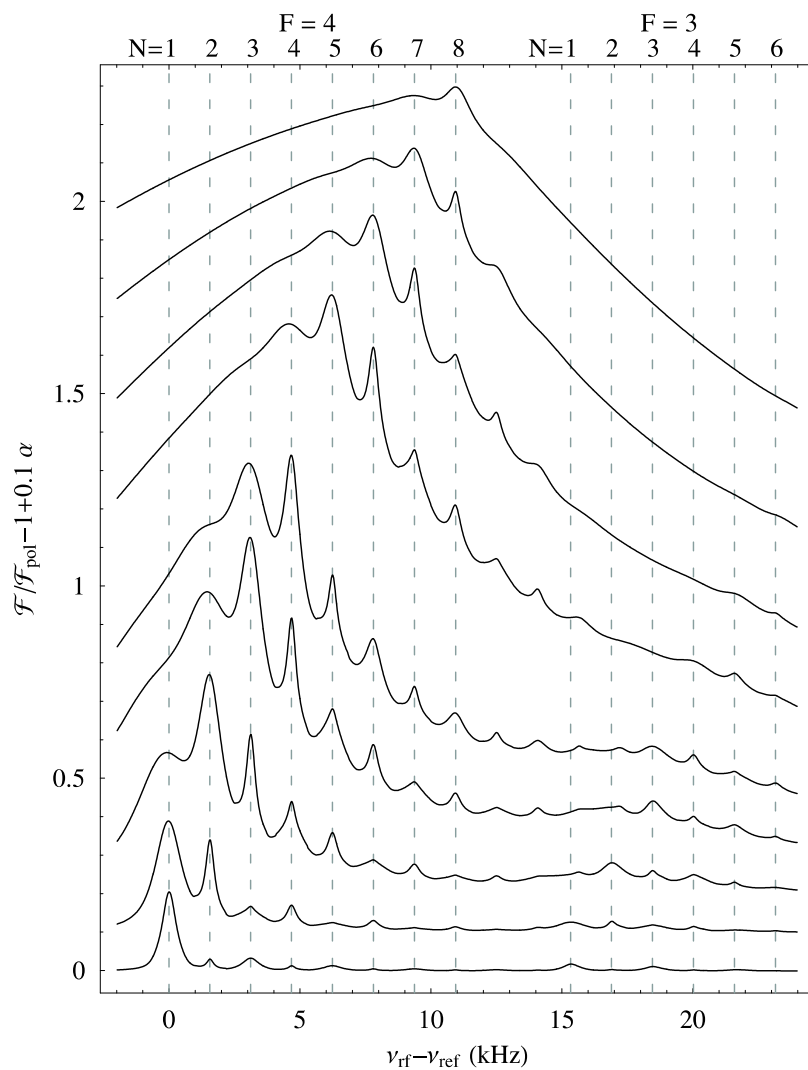


Figure 4.8: The calculated spectra of Fig. 4.7 convoluted with a Gaussian distribution of 300 Hz width. By this the effect of technical broadening due to magnetic field inhomogeneities and instabilities has been taken into account.

onset (no r.f. power broadening) are much smaller than the corresponding experimental widths. The model calculation has no further free parameter, which can be used for a better matching of the experimental and theoretical spectra. We note nonetheless that lines, whose widths are predominantly determined by r.f. power broadening, such as the 8 photon-line on the top spectrum or the 7-photon lines on the second spectrum are well reproduced by the calculation.

The experimental linewidths are determined by several mechanisms, such as the finite sweep time, field inhomogeneities and field fluctuations. The sweep rate of the radio frequency scan should be sufficiently low in order to assure that the level populations at all times are as close as possible to their equilibrium distribution. However, the drop of the atomic signal mentioned above puts some constraints on acceptable scan speeds, and a scan duration of 20 s was chosen as a trade-off between these conditions. The finite scan time does not only cause a line-broadening but also a sweep-direction dependent asymmetry of the line shapes, faintly visible in Fig. 4.5.

The recording of stable and narrow multi-photon spectra puts severe constraint on the homogeneity of the magnetic field B_0 . In very slow scans over a single resonance we observed minimal linewidths of approximately 300 Hz. These can be explained by a field inhomogeneity $\Delta B_0/B_0$ over the sample volume on the order of 10^{-4} . Although model calculations of the field distribution produced by the Helmholtz coils used predict a relative homogeneity of better than 10^{-6} over the sample volume – yielding minimal linewidths of 4 Hz – this homogeneity may be reduced due to distortions induced by distant ferromagnetic components and/or superconducting indium sealing rings.

Besides field inhomogeneities field fluctuations can also contribute to the linewidth and require a current stability of better than 10^{-4} . Although we used superconducting wires for the Helmholtz coils that generated the B_0 field, the coils were connected to a stabilized current source during the experiments. In future experiments we plan to use superconducting coils with a self-sustained supercurrent. The superswitch for this application is currently under construction. With this improvement contributions to the resonance linewidths from current noise and instabilities will be significantly reduced.

In order to take the effects from inhomogeneities and field fluctuations into account, we have convoluted the theoretical spectra of Fig. 4.7 with a Gaussian distribution of field values with a width of 86 nT, corresponding to a frequency distribution of 300 Hz. The resulting spectra are shown in Fig. 4.8. This last series of spectra gives a satisfactory description of the experimental data.

4.4 Use of multi-photon transitions

One of the key motivations for the present study is the perspective that multi-photon lines might lead to an increased magnetometric sensitivity in ODMR spectroscopy. On one hand the linewidth of an N -photon resonance is N -times smaller than the linewidth of a single photon transition provided the corresponding coherences relax at the same rate. However, as the details of the relaxation mechanisms are not yet known, no quantitative theoretical prediction can be made at this point. From an experimental point of view no statement about improved sensitivity can be made yet because of the present problems with abnormal linewidths.

Once the technical problems are overcome the spectra are expected to reveal their intrinsic linewidths. Their description will then require the inclusion of realistic relaxation mechanisms in the calculations. In its simplest version the relaxation of the spin coherences could be modelled as isotropic, and can be described by a single transverse relaxation rate γ_2 . However, very little is known so far about the mechanisms governing the longitudinal and transverse spin relaxation of cesium in b.c.c. He. It has been speculated [22] that a coupling of the atomic spins to quadrupolar bubble shape oscillations might be responsible for the long, but nonetheless finite longitudinal

relaxation times [5]. However, no proof of that assumption has been given so far. A more realistic relaxation model would have to include anisotropic relaxation processes as the one just mentioned using the approach developed, e.g., by Happer [23, 24]. Multi-photon processes, in which coherences of different orders, i.e. transverse atomic multipole moments of different ranks can be spectrally isolated may prove to be a powerful tool for testing different relaxation models, once the technical difficulties are overcome. This may open the way to a deeper understanding of the mechanisms and the symmetries governing the interaction of alkali spins with the helium matrix. Efforts towards improving the measurements and towards extending the calculations by comparing different relaxation models is currently in progress and will be the subject of a forthcoming publication [20].

Another interesting aspect of the use of particular multi-photon transitions concerns the experimental search for permanent electric dipole moments (EDM) in atoms. An EDM violates the discrete symmetries of parity and time reversal. The experimental signature of an EDM is a shift of a magnetic resonance transition proportional to the strength of an external static electric field. The techniques used in various ongoing experiments are variants of magnetic resonance spectroscopy, and the sensitivity of a given experiment to EDMs can be expressed in terms of its magnetometric sensitivity [25]. Besides the expected statistical advantage of multi-photon transitions some specific transitions may also be very useful for the suppression of a serious systematic effect in EDM experiments.

The resonance energy of a one-photon transition $|F, M\rangle \rightarrow |F, M-1\rangle$ of an atom exposed to parallel/antiparallel magnetic and electric fields B, \mathcal{E}_\pm is given by

$$\hbar\omega_M^\pm = g_F\mu_B B_0 + g_F d \mathcal{E}_\pm + 3\alpha_2 \mathcal{E}_\pm^2 (2M-1),$$

where α_2 is the electric tensor polarizability, which characterizes the second order Stark splitting of the hyperfine states $|F, M\rangle$ via

$$\Delta E(FM) = \alpha_2 \mathcal{E}_\pm^2 [3M^2 - F(F+1)] \quad (4.4)$$

The EDM d is experimentally determined by comparing the resonance frequencies ω_M^\pm in electric fields \mathcal{E}_\pm of opposite polarities

$$\begin{aligned} \hbar\Delta\omega_M &= \hbar(\omega_M^+ - \omega_M^-) \\ &= g_F d (\mathcal{E}_+ - \mathcal{E}_-) + 3\alpha_2 (2M-1) (\mathcal{E}_+^2 - \mathcal{E}_-^2). \end{aligned}$$

In a perfect experiment the reversal is perfect, i.e. $\mathcal{E}_+ = -\mathcal{E}_-$ and

$$\hbar\Delta\omega_M = 2g_F d |\mathcal{E}|.$$

In practice, however, the field reversal may not be perfect. If we parameterize the imperfection as $\mathcal{E}_\pm = \pm|\mathcal{E}| + \Delta\mathcal{E}$, the resonance shift becomes

$$\hbar\Delta\omega_M = 2g_F d |\mathcal{E}| + 12\alpha_2 |\mathcal{E}| \Delta\mathcal{E} (2M-1).$$

However, this systematic effect connected with imperfect field reversals does not arise in multi-photon transitions coupling the states $|F, M\rangle$ and $|F, -M\rangle$. From the quadratic M -dependence of the tensor Stark shift (Eq. 4.4) one sees that the latter does not influence the resonance frequencies, so that the systematic effect discussed above becomes obsolete. In the Cs $F=4$ state the $|F, M=4\rangle \rightarrow |F, M=-4\rangle$ transition thus combines an anticipated high sensitivity with the independence of systematic quadratic Stark shifts.

We stress that the outlined features of multi-photon spectroscopy are not specifically connected with the sample used here, but that they can be applied as well to experiments in vapors, beams or other atomic samples.

4.5 Summary

We have shown that transitions involving the simultaneous absorption of multiple r.f. photons can be observed in cesium atoms implanted in solid helium and that the spectra are well reproduced by a theoretical model taking field inhomogeneities and fluctuations into account.

Multi-photon spectra may be well suited to shine more light on the mechanisms governing the relaxation of spin coherences of alkalis in condensed helium matrices. We have also outlined the possible statistical and systematic advantages for using multi-photon transitions in EDM-experiments.

Acknowledgments

This work was supported by a grant of the Schweizerischer Nationalfonds.

References

- [1] J. Brossel and A. Kastler. La detection de la resonance magnetique des niveaux excités - l'effet de dépolariation des radiations de résonance optique et de fluorescence. *C. R. Acad. Sci.*, 229(23):1213–1215, 1949.
- [2] M. Arndt, S. I. Kanorsky, A. Weis, and T. W. Hänsch. Long electronic spin relaxation times of Cs atoms in solid ^4He . *Phys. Rev. Lett.*, 74(8):1359, 1995.
- [3] S. I. Kanorsky, S. Lang, S. Lücke, S. B. Ross, T. W. Hänsch, and A. Weis. Millihertz magnetic resonance spectroscopy of Cs atoms in body-centered-cubic ^4He . *Phys. Rev. A*, 54(2):R1010, 1996.
- [4] S. I. Kanorsky, M. Arndt, R. Dziewior, A. Weis, and T. W. Hänsch. Optical spectroscopy of atoms trapped in solid helium. *Phys. Rev. B*, 49(5):3645, 1994.
- [5] S. Lang, S. I. Kanorsky, T. Eichler, R. Müller-Siebert, T. W. Hänsch, and A. Weis. Optical pumping of Cs atoms in solid ^4He . *Phys. Rev. A*, 60(5):3867, 1999.
- [6] J. M. Winter. Étude théorique et expérimentale des transitions a plusieurs quanta entre les sous-niveaux Zeeman d'un atome. *Ann. Phys. (Paris)*, 1959.
- [7] M. N. Hack. Multiple quantum transitions of a system of coupled angular momenta. *Rev. Mod. Phys.*, 104(12):1, 1956.
- [8] H. Salwen. Resonance transitions in molecular beam experiments. I. general theory of transitions in a rotating magnetic field. *Rev. Mod. Phys.*, 99(4):1274–1286, 1955.
- [9] J. Hermann and S. Swain. Resonance lineshapes in multi-level atomic systems. *J. Phys. B*, 10(10):1815–1833, 1977.
- [10] P. Kusch. Some observations of double-quantum and triple-quantum transitions. *Rev. Mod. Phys.*, 93(5):1022–1025, 1954.
- [11] T. Skalinsy. Orientation optique des atomes dans la vapeur saturante de caesium. *C. R. Acad. Sci.*, 245(22):1908–1911, 1957.
- [12] A. S. Pazgalev and E. B. Alexandrov. Exact solution of the problem of resonance in a multilevel system in a rotating electromagnetic field. *Optics and Spectroscopy*, 80(4):473–478, 1996.
- [13] A. S. Pazgalev and E. B. Alexandrov. Exact solution of the problem of multi-quantum resonances in Zeeman structure of ^{133}Cs and ^6Li atoms. *Optics and Spectroscopy*, 86(1):6–10, 1999.
- [14] A. S. Pazgalev, E. B. Alexandrov, and J. L. Raston. Observation of four-quantum resonance in the Zeeman structure of the ground-state of ^{39}K . *Optics and Spectroscopy*, 82(1):10–15, 1997.
- [15] J. D. Xu, G. Wäckerle, and M. Mehring. Multiple-quantum spin coherences in the ground state of alkali atomic vapor. *Phys. Rev. A*, 55(1):206–213, 1997.
- [16] G. Breit and I.I. Rabi. *Rev. Mod. Phys.*, 38:2082, 1931.

- [17] S. Lang, S. I. Kanorsky, M. Arndt, S. B. Ross, T. W. Hänsch, and A. Weis. The hyperfine structure of Cs atoms in the b.c.c. phase of solid ^4He . *Europhysics Letters*, 30(4):233, 1995.
- [18] Taro Eichler, R. Müller-Siebert, Daniel Nettels, S. I. Kanorsky, and A. Weis. Optical detection of nonradiating alkali atoms in solid helium. *Phys. Rev. Lett.*, 88(12):123002, 2002.
- [19] Taro Eichler. *Magneto-optical Spectroscopy of Alkali Atoms in Helium Crystals*. Ph.D. thesis, Rheinische Friedrich-Wilhelms-Universität Bonn, 2000.
- [20] D. Nettels, R. Müller-Siebert, and Antoine Weis. Relaxation mechanisms of multi-quantum coherences in the Zeeman structure of atomic Cs trapped in solid He. Invited paper, accepted for publication in *Appl. Phys. B*.
- [21] R. Müller-Siebert, D. Nettels, and Antoine Weis. To be submitted.
- [22] Serguei Kanorsky and Antoine Weis. Optical and magneto-optical spectroscopy of point defects in condensed helium. In *Advances in Atomic, Molecular, and Optical Physics*, volume 38, pages 87–119. Academic Press, 1997.
- [23] William Happer. Multipole relaxation times of a weak perturbing spin system. *Phys. Rev. B*, 1(5):2203–2207, 1970.
- [24] William Happer. Optical pumping. 44(2):169–249, 1972.
- [25] Antoine Weis. In *Electron Theory and Quantum Electrodynamics: 100 years later*. Plenum Press, New York, 1997.

Chapter 5

Relaxation mechanisms of multi-quantum coherences in the Zeeman structure of atomic Cs trapped in solid He

D. Nettels, R. Müller-Siebert, and A. Weis

Département de Physique, Université de Fribourg, Chemin du Musée 3, 1700 Fribourg, Switzerland

accepted for publication by *Appl. Phys. B*
(invited paper)

Abstract: We have extended our previous work on near-degenerate magnetic resonance transitions in alkali ground states involving the simultaneous absorption of multiple radio-frequency quanta. New experimental results with an improved spectral resolution were obtained with cesium atoms trapped in the cubic phase of a helium crystal. The main objective of the paper is a theoretical study of the influence of stochastic perturbations of given multipole orders on the various multi-photon coherences. Algebraic and numerical results for perturbations of both dipolar and quadrupolar symmetry are presented. The present experimental resolution does not yet allow us to distinguish between these two most likely relaxation mechanisms. Nonetheless, the experimental spectra are very well described when allowing in the calculations for a magnetic field inhomogeneity of $2 \cdot 10^{-5}$.

PACS 76.70.Hb; 32.80.Wr; 32.30.Dx; 32.60.+i

5.1 Introduction

In a recent paper we reported on the observation of magnetic resonance transitions involving the simultaneous absorption of N radio frequency (r.f.) photons between Zeeman split hyperfine sublevels $|F, M\rangle$ and $|F, M + N\rangle$ in the $6S_{1/2}$ ground state of Cs implanted in the body-centered cubic (b.c.c.) phase of solid He^4 [1]. Such transitions are of multiple interest regarding applications and fundamental investigations. Under the simplest model assumption that all multi-quantum coherences have the same relaxation rate, one expects the N -photon transitions to have a resonance linewidth which is N -times smaller than the width of usual one-photon transition. Therefore multi-photon transitions have the potential to increase the spectroscopic sensitivity in magnetic resonance experiments. We showed furthermore [1] that some specific transitions allow to suppress a serious systematic effect connected with quadratic Stark shifts in experiments searching for permanent electric dipole moments. Finally we suggested [1] that multiphoton spectra might be a useful tool for the better understanding of the mechanisms, which govern the relaxation of the ground state spin polarization of the cesium atoms due to their interactions with lattice vibrations of the surrounding He matrix.

The theoretical investigation of the influence of different relaxation processes on the multi-photon spectra and the comparison with improved experimental data are the main topic of the present paper. In our previous work [1] only relaxation based on optical pumping was taken into account, similar to the calculations of Pazgalev and Alexandrov [2]. In this work we have significantly extended the treatment of the relaxation processes using generalized ground state master equations describing the evolution of the atomic ground state populations and coherences in the density matrix formalism under the influence of static and oscillating magnetic fields, optical pumping and various relaxation processes.

The optical absorption and emission lines of Cesium atoms embedded in the body-centered cubic (b.c.c.) phase of solid He^4 are strongly broadened and shifted by the helium matrix [3]. As a consequence of the very high degree of spherical symmetry of the local trapping sites of the impurity atoms (atomic bubbles) the sample can nonetheless be efficiently polarized by optical pumping [4]. The non-magnetic nature of the host matrix atoms and their isotropic distribution around the defect atoms ensure that the alkali spins are only very weakly perturbed, which is reflected by longitudinal spin relaxation times $T_1 = 1/\gamma_1$ of $\langle J_z \rangle$ on the order of 1 second [5] and by very narrow magnetic resonance lines [6]. For a static distribution of the helium atoms around the cesium atoms one would expect quasi-infinite relaxation times. The very long, but nonetheless finite longitudinal and transverse spin coherence times are most probably due to fluctuations of the bubble interface boundary. So far no detailed investigations of the mechanisms by which such fluctuations couple to the Cs spins were performed. In the present paper we calculate the effect of dipolar and quadrupolar shape oscillations on the relaxation of multi-photon coherences and show explicitly that these spectra have the potential to discriminate between the two processes.

Our previously measured magnetic resonance lines were strongly broadened due to magnetic field inhomogeneities and current instabilities. This broadening severely hinders the study of the intrinsic relaxation mechanisms. In the meantime we have improved the experimental apparatus by suppressing some of these technical noise sources. We present new experimental data showing an increased spectroscopic resolution. As before the measurements were done using the technique of optically detected magnetic resonance (ODMR), in which resonant optical interactions are used both to build up spin polarization in the sample and to detect radio-frequency induced transitions between the magnetic sublevels via their effect on the optical properties of the alkali sample. Unfortunately the observed widths of the experimental spectra are still inhomogeneously broadened and do not yet allow to draw a conclusion regarding the actual relaxation mechanism.

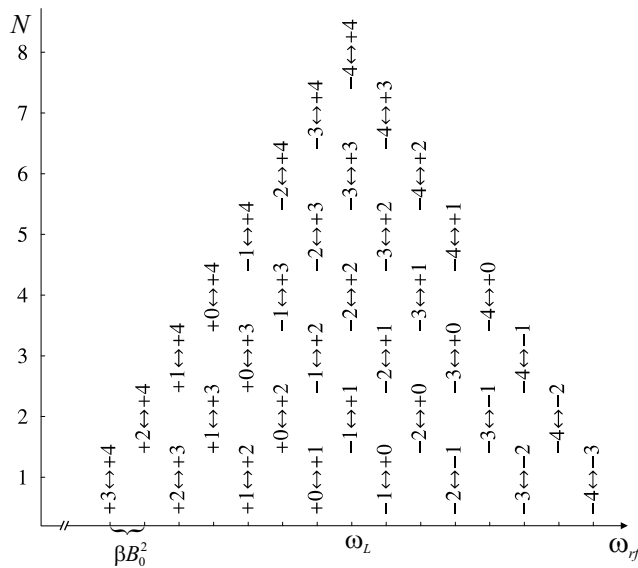


Figure 5.1: Resonance frequencies of the multi-photon transitions involving $N = 1 \dots 8$ -photons coupling states M and $M + N$ in a spin $F = 4$ system. The line positions are given by Eq. 5.1 with $\beta < 0$ as for Cs.

Nonetheless the spectra can be very well reproduced by allowing for a small field inhomogeneity in the calculations.

5.2 Simple theory of multi-photon transitions

5.2.1 Multi-photon transition between substates of a hyperfine level F in a magnetic field

A detailed introduction to the structure of Zeeman-split multi-photon transitions was presented in [1]. Here we just recall the main features. In a weak magnetic field B_0 (linear Zeeman effect) all single $\Delta M = 1$ photon transitions between adjacent levels $|F, M\rangle$ and $|F, M+1\rangle$ of an isolated hyperfine multiplet F have the same transition frequency $\omega_L = \gamma B_0 = g_F \mu_B B_0 / \hbar$. In stronger magnetic fields the combined hyperfine and Zeeman interactions lead to level shifts which are nonlinear in B_0 and M (Breit-Rabi diagram). The lowest order correction terms to the linear Zeeman effect are quadratic in M and can be parameterized as

$$\omega_M = \omega_{hfs} + \gamma M B_0 + (\alpha + \beta M^2) B_0^2,$$

where ω_{hfs} is the hyperfine frequency shift of the given hyperfine level F , and α and β are constants depending on the specific state. As a consequence of the non-equidistant level spacing processes in which N identical r.f.-photons are simultaneously absorbed can be spectrally resolved. The resonance frequency of an N -photon transition starting from level M is given by

$$\frac{\omega_{M+N} - \omega_M}{N} = \gamma B_0 + \beta B_0^2 (2M + N). \quad (5.1)$$

There are $2F$ distinct transitions involving the absorption of a single photon transitions, $2F - 1$ two photon transitions \dots , up to a single transition involving the absorption of $N = 2F$ photons. The resonance energies of all possible multi-photon transitions are represented in Fig. 5.1 for the hyperfine level $F = 4$. The higher order multiphoton lines appear successively in the magnetic resonance spectra as the r.f. intensity is increased.

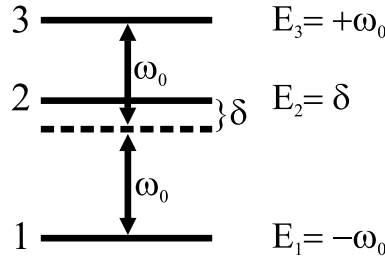


Figure 5.2: Three-level system: level 2 is detuned by δ from the average energy spacing $\omega_0 = \frac{1}{2}(E_3 - E_1)$ of levels 1 and 2.

5.2.2 Lineshapes of multi-quantum transitions

The simplest system which allows the observation of multi-quantum transitions is the $F = 1$ three level system shown in Fig. 5.2. Multi-photon transitions in that system were treated by Salwen [7, 8] and Hermann and Swain [7, 8]. In both references relaxation processes were not taken into account and r.f. power broadening was the only mechanism which determined the resonance line shapes. Under the assumption that the resonance lines are spectrally well resolved the lineshapes of the multi-quantum transitions can then be approximated by simple Lorentzians. We have extended the calculations of these authors by explicitly adding relaxation terms for the different multi-photon coherences.

The interaction with a r.f.-field with frequency ω_{rf} is described in the rotating wave approximation by the time independent Hamiltonian

$$H = \hbar \begin{pmatrix} \Delta & \Omega_{12} & 0 \\ \Omega_{12}^* & \delta & \Omega_{23} \\ 0 & \Omega_{23}^* & -\Delta \end{pmatrix},$$

where $\Delta = \omega_{rf} - \omega_0$. δ is the displacement of the intermediate state. For simplicity we assume that the Rabi frequencies $\Omega_{12} = \Omega_{23} \equiv \Omega = \Omega^*$. Making the additional assumptions that the populations of all states relax with a common rate γ_1 against a steady state population and that the $\Delta M = 1$ -coherences ρ_{12} and ρ_{23} relax with γ_2 and that the $\Delta M = 2$ -coherence ρ_{13} relaxes with γ_3 , we obtain the following approximative expressions for the lineshapes of the transitions 1-2 and 1-3:

$$P_{12}(\Delta_1) = \frac{2 \frac{\gamma_2}{\gamma_1} \Omega^2}{\Delta_1^2 + \gamma_2^2 + 4 \frac{\gamma_2}{\gamma_1} \Omega^2}$$

$$P_{13}(\Delta_2) = \frac{2 \frac{\gamma_3}{\gamma_1} \frac{\Omega^2}{2} \frac{\Omega^2}{\delta}}{\Delta_2^2 + \frac{\gamma_3^2}{2} + 4 \frac{\gamma_3}{\gamma_1} \frac{\Omega^2}{2} \frac{\Omega^2}{\delta}},$$

where Δ_1 and Δ_2 are the detunings from the one-photon and two-photon transition frequencies respectively.

In a next step we have extended the calculation to spin systems with arbitrary values of F in which N -photon transitions occur connecting states $|F, M\rangle$ and $|F, M + N\rangle$. For the sake of simplicity we assume that the intermediate states $|F, M + k\rangle$ with $(k = 2, \dots, N - 1)$ are all displaced by the same amount δ from the value $\omega_M + k\omega_0^{(N)}$, where $\omega_0^{(N)} = (\omega_{M+N} - \omega_M)/N$. Again we set all $\Omega_{ij} = \Omega$ and get

$$P_{M, M+N} = \frac{2 \frac{\gamma_{N+1}}{\gamma_1} \frac{\Omega^2}{N} \frac{\Omega^{2(N-1)}}{\delta}}{\Delta_N^2 + \frac{\gamma_{N+1}^2}{N} + 4 \frac{\gamma_{N+1}}{\gamma_1} \frac{\Omega^2}{N} \frac{\Omega^{2(N+1)}}{\delta}}, \quad (5.2)$$

where Δ_N is the detuning from the N -photon resonance and γ_{N+1} is the relaxation rate of the coherence between the states $|M\rangle$ and $|M+N\rangle$.

Although in our experiments the condition (spectral isolation of the N -photon resonance lines) for the validity of Eq. 5.2 is not completely fulfilled, it is nonetheless instructive to use the simple Lorentzian lineshapes of (5.2) for a first qualitative comparison of the multi-photon lines with the single-photon lines. Our particular interest lies in the possible achievable gain in spectroscopic sensitivity. This sensitivity is determined by the accuracy with which the center of a given resonance line can be determined experimentally at a given experimental noise level, and is proportional to the steepness of the resonance, i.e., the maximal slope $|dP/d\Delta|$ of the resonance lineshape $P(\Delta)$. The steepness is proportional to the ratio $R_N = P(\Delta = 0)/\Delta\omega_{FWHM}$ of the resonant signal amplitude and its width. For the Lorentzians of Eq. 5.2 the resonant transition probability $P(0)$ of an N -photon transition reaches a maximum value of

$$R_N^{\max} = \frac{1}{6\sqrt{3}} \frac{N}{\gamma_{N+1}} \quad (5.3)$$

at the optimal r.f. amplitude given in terms of the corresponding Rabi frequency by

$$\Omega = \Omega_{opt} \equiv \delta \left(\frac{\gamma_1 \gamma_{N+1}}{2\delta^2} \right)^{\frac{1}{2N}}, \quad (5.4)$$

The corresponding transition probabilities $P_{M,M+N}(\Delta_N = 0, \Omega = \Omega_{opt})$ are found to have the same constant value of $1/3$ independent of N and the widths of the Lorentzians are found to vary with N as

$$\Delta\omega_{FWHM} = 2\sqrt{3} \frac{\gamma_{N+1}}{N},$$

so that the widths alone determine the N -dependence of the steepness. The validity of the used approximations requires that the relaxation rates γ_i are much smaller than δ . Hence Ω has to be increased according to Eq. 5.4 in order to observe the higher order multi-photon resonances. The relative change of the sensitivity of an N -photon resonance compared to a single photon resonance is thus given according to (5.3) by

$$G_N \equiv \frac{R_N^{\max}}{R_{N=1}^{\max}} = \frac{\gamma_2}{\gamma_{N+1}} N. \quad (5.5)$$

For the simplest case, treated in our previous paper, in which all multi-photon relaxation rates $\gamma_2, \gamma_3, \dots, \gamma_{N+1}$ are equal, one thus obtains an increased sensitivity, which is directly proportional to the number of involved photons. However, in the more realistic case, in which the rates γ_N differ this simple scaling law no longer holds. It is one of the goals of this paper to determine how the relaxation rates γ_N of multi-quantum coherences and hence the anticipated improvement of the spectroscopic sensitivity G_N depend on the nature and symmetry of different relaxation mechanisms.

5.3 Numerical Calculation of the ODMR signal

5.3.1 Optically detected magnetic resonance

In the experiments the magnetic resonances addressed in the previous paragraph were observed using a double resonance technique. A circularly polarized laser beam resonant with the Cs D_1 -transition was used to prepare the necessary population differences in the magnetic sublevels by optical pumping. As the scattering rate of the laser radiation depends on the degree of spin

polarization of the medium, any change of the latter due to a magnetic resonance transition can be detected by monitoring the fluorescence light intensity. This technique is known as optically detect magnetic resonance (ODMR).

We have calculated the multi-photon ODMR spectra of Cs by numerically solving the steady-state Liouville equation for the density matrix ρ describing the 16 sublevels of the $6S_{1/2}$ ground state hyperfine structure ($F = 3, 4$). The rate of change $\dot{\rho}$ of the density matrix is governed by the interaction with the (static and oscillating) magnetic fields, the optical pumping interaction with the resonant circularly polarized laser beam and the sublevel population and coherence relaxation processes:

$$\dot{\rho} = (\dot{\rho})_{mag} + (\dot{\rho})_{op} + (\dot{\rho})_{rel}. \quad (5.6)$$

Steady-state solutions were obtained by setting $\dot{\rho} = 0$. In the following we discuss the three terms of Eq. 5.6 in detail.

5.3.2 Magnetic interaction

The Liouville equation is solved in the $|F_{\pm}, M\rangle$ basis in which the Hamiltonian

$$H_0 = A \mathbf{I} \cdot \mathbf{J} + g_J \mu_B J_z B_0 - g_I \mu_B I_z B_0,$$

describing the hyperfine and static Zeeman interactions is diagonal. The brackets around F_{\pm} in $|F_{\pm}, M\rangle$ indicate that F is not a good quantum number in presence of the magnetic field; F_{\pm} are merely used as convenient state labels. Since the two hyperfine levels are well separated in energy, it is justified to neglect all matrix elements of the radio frequency interaction operator which couple states of different F -values. The corresponding coherences in the density matrix ρ will also be ignored, so that the density matrix of the ground state has the form

$$\rho = \begin{pmatrix} \rho_{F_-} & 0 \\ 0 & \rho_{F_+} \end{pmatrix},$$

where $\rho_{F_{\pm}}$ are sub-matrices restricted to the eigenspaces of F_{\pm} spanned by the states $|F_{\pm}, M\rangle$. The interaction operator of the atoms with the r.f.-field $B_1(t) = B_1 \cos \omega t$ oscillating along the x -direction is

$$\begin{aligned} V(t) &= (g_J \mu_B J_x B_1 - g_I \mu_B I_x B_1) \cos \omega_{rf} t \\ &= 2V_0 \cos \omega_{rf} t. \end{aligned} \quad (5.7)$$

In the rotating field approximation the Liouville equations for ρ_{F_-} and ρ_{F_+} are

$$i\hbar(\dot{\rho}_{F_{\pm}})_{mag} = [H_{\pm}, \rho_{F_{\pm}}]$$

with the time-independent Hamiltonian

$$H_{\pm} = H_0 \mp \hbar\omega_{rf} F_z + V_0,$$

where all operators are restricted to the corresponding $|F_{\pm}, M\rangle$ spaces. The different signs in front of the second term reflect the facts that we have chosen ω_{rf} to be positive and that the g -factors of the two hyperfine levels have opposite signs.

5.3.3 Optical pumping and detection signal

A detailed discussion of optical pumping processes of Cs atoms in solid ^4He can be found in [4]. In that paper optical pumping was calculated using rate equations for the ground state populations. Here we generalize this approach by the simultaneous treatment of optical pumping and ground state coherence evolution under the action of the magnetic fields. The destruction of these coherences by the absorptive interaction with the optical radiation then contributes to the broadening of the magnetic resonance lines. In the experiment the laser beam traverses several cryostat windows, some of which show stress-induced birefringence. As a consequence the beam interacting with the sample is not 100% circularly polarized. We take this into account by allowing the light field \mathbf{E} to be elliptically polarized

$$\begin{aligned}\mathbf{E} &= \frac{E_0}{\sqrt{2}} \begin{pmatrix} \cos \omega t \\ \sin \omega t + \varphi \end{pmatrix} = \frac{E_0}{\sqrt{2}} \begin{pmatrix} 1 \\ ie^{-i\varphi} \end{pmatrix} \frac{e^{-i\omega t}}{2} + c.c. \\ &= \frac{1}{2} \mathcal{E} e^{-i\omega t} + c.c.,\end{aligned}\quad (5.8)$$

where $c.c.$ denotes the complex conjugate, ω is the light frequency and E_0 is the amplitude of the electric field. The two components of the vectors correspond to the x - and y -directions, respectively. The degree of circular polarization of this optical field is $|\cos(\varphi)|$ and the light is 100% left-circularly polarized for $\varphi = 0$.

The interaction between the radiation field \mathbf{E} and the atoms is given by

$$V_{AL} = -\mathbf{E} \cdot \mathbf{d}, \quad (5.9)$$

where \mathbf{d} is the electric dipole operator. Because of the large homogeneous linewidth (10 nm) of the D_1 -transition of Cs in solid He and the relatively low laser intensities used, excited state populations and stimulated emission processes can be omitted. As a consequence the atomic evolution under the influence of optical pumping can be described by pure ground state equations only [9]. A further consequence of the large optical linewidth is the fact that all four hyperfine transitions of the D_1 -transition are excited simultaneously. We further note that, as shown earlier [3, 4], the creation of spin polarization in Cs trapped in b.c.c. He proceeds via repopulation pumping in which the spin-polarization in the excited state is preserved during the optical absorption-emission cycle. We define the operator $D = D_{ge} + D_{eg}$, with

$$D_{eg} = \frac{-1}{2\hbar} P_e \mathcal{E} \cdot \mathbf{d} P_g \quad \text{and} \quad D_{ge} = D_{eg}^\dagger,$$

where $P_g = \sum_\mu |\mu\rangle\langle\mu|$ and $P_e = \sum_m |m\rangle\langle m|$ are projection operators onto ground and excited states respectively. The sums \sum_μ and \sum_m extend over all magnetic substates of the $6S_{1/2}$ ground state and the $6P_{1/2}$ excited state. It is shown in the appendix that the rate of change of the ground state density matrix elements under the influence of resonant optical pumping is governed by

$$\begin{aligned}(\dot{\rho})_{op} &= -\frac{2}{\gamma} [D_{ge} D_{eg}, \rho] \\ &\quad + \frac{3}{\gamma} \sum_{q=-1}^1 (C_{-q}^1)_{ge} D_{eg} \rho D_{ge} (C_q^1)_{eg},\end{aligned}\quad (5.10)$$

where $C_q^1 = \sqrt{4\pi/3} Y_{1q}$ is the spherical unity operator and γ the homogenous optical linewidth. The two terms in (5.10) describe depopulation and repopulation pumping respectively. By

applying the Wigner-Eckart theorem to the matrix elements of \mathbf{d} one sees that the elements of (5.10) are proportional to the pump rate γ_p , defined as

$$\gamma_p = \frac{E_0^2}{\hbar^2 \gamma} |\langle 6S_{1/2} || d || 6P_{1/2} \rangle|^2.$$

In the experiment fluorescence of the Cs atoms is detected and the fluorescence rate \mathcal{F} is (s. appendix) given by

$$\mathcal{F} = \mathcal{F}(\rho) = \frac{4}{\gamma} \text{tr}(D_{eg} \rho D_{ge}) \quad (5.11)$$

We note that \mathcal{F} is proportional to γ_p . Alternatively, \mathcal{F} can be expressed as

$$\mathcal{F} = \mathcal{F}_{\text{unpol}} (1 - P_z \cos \varphi),$$

where $P_z = 2 \langle J_z \rangle$ is the spin polarization and $\mathcal{F}_{\text{unpol}}$ is the fluorescence rate of the unpolarized atomic ensemble [4] in thermal equilibrium. Optical pumping produces a spin polarization $P_z^{\text{max}} = 2 \langle J_z \rangle_{\text{max}}$ which depends on the light intensity with a corresponding minimum in fluorescence \mathcal{F}_{pol} . The magnetic resonance process alters P_z in a resonant way, which is reflected by a corresponding resonant change in the fluorescence rate \mathcal{F} .

5.3.4 Relaxation

As mentioned in the introduction the electronic spin polarization of alkali atoms embedded in the b.c.c. phase of solid helium reaches values on the order of 1 second. This is a consequence of the spherical symmetry of the local trapping site (spherical bubble) and the non-magnetic properties of the host matrix atoms, as helium has neither an electronic nor a nuclear magnetic moment. The most likely mechanism responsible for the perturbation of the alkali spins are helium lattice vibrations, and more specifically shape fluctuations of the bubble interface boundary. The atoms of the first solvation shell undergo oscillations around their equilibrium positions and the fluctuating shape of the interface (described by the bubble radius $R(\theta, \phi)$) formed by these atoms may be decomposed into spherical harmonics $Y_{k,q}$ as

$$R(\theta, \phi, t) = R_0 + \sum_{k,q} a_{k,q}(t) Y_{k,q}(\theta, \phi),$$

where the coefficients $a_{k,q}(t)$ describe the time dependent fluctuations of a given multipole shape. Without such fluctuations the bubble shape is spherical $R(\theta, \phi, t) = R_0$ and the alkali ground state preserves its S-state character. The bubble shape fluctuations deform the electronic wave function of the alkali atom, which, in quantum mechanical terms corresponds to an L-mixing interaction. This admixture of higher orbital momentum states, together with spin-orbit and hyperfine interactions in the cesium atom then constitutes a mechanism by which the helium matrix atoms can couple to the alkali spins. For a spin perturbing interaction of a defined multipolarity k the perturbation $H_{fl}(t)$ between the bubble shape and the alkali spins can then be written as [10]

$$H_{fl}(t) = \sum_{q=-k}^k (-1)^q F_{-q}^k(t) T_q^k(S, I), \quad (5.12)$$

where the $T_q^k(S, I)$ are spherical tensor operators acting in the combined electronic (S) and nuclear spin (I) spaces that describe atomic properties. The coefficients $F_q^k(t)$ are determined by the amplitudes $a_{k,q}(t)$ of the bubble oscillations and describe the induced fields coupling to the atom.

The lowest order multipole oscillation is the monopole (or breathing mode) oscillation described by $a_{0,0}(t)$. Because of its scalar nature it will not affect spin coherences nor level populations. However, as shown previously [11], it does affect magnetic hyperfine transitions $\langle F = 4, M | \mu | F = 3, M \rangle$ and hence broadens the corresponding resonance via a modulation of the Fermi contact term of the ground state hyperfine interaction. The next multipole oscillation is the dipole oscillation ($k = 1$). A small (compared to the bubble radius) amplitude dipole deformation of the bubble is equivalent to an small amplitude displacement of the atom from its equilibrium position inside a spherical bubble. We will restrict the discussion in the following to dipole ($k = 1$) and quadrupole ($k = 2$) shape oscillations. The bubble-spin interaction can have an electric and/or a magnetic character. As the atoms have no static electric vector property the $k = 1$ dipole oscillations the perturbation operator in this case will be dominated by the coupling of induced fluctuating magnetic fields $F_q^1(t) \propto B_q(t)$ to the atomic magnetic moment $T_q^1(S, I) \propto \mu_q = (-g_s S_q + g_I I_q) \frac{\mu_B}{\hbar}$. As $g_I \ll g_s$ contributions from the nuclear moment will be neglected in the calculations, so that the tensor components $T_q^1(S)$ act in electronic spin space only. In the case of quadrupolar shape oscillations, on the other hand, the second rank tensors $T_q^2(S, I)$ can not couple to the electronic angular momentum, as the Wigner-Eckart theorem implies that $\langle J = 1/2 || T^2 || J = 1/2 \rangle = 0$ so that the $k = 2$ interaction operators $T_q^2(I)$ act in nuclear spin space only. Here the simplest interaction will be the coupling of fluctuating electric field gradients, described by $F_q^2(t)$ to the components of the electric quadrupole moment of the Cs nucleus, described by $T_q^2(I)$.

The ability of $H_{fl}(t)$ to drive ground state transitions and/or to dephase spin coherences is determined by the magnitude of the power spectral density $J(\omega)$ of the fluctuating field components $F_q^k(t)$ in the vicinity of the relevant atomic transition frequency. $J(\omega)$ can be calculated according to the Wiener-Khinchine theorem as the Fourier cosine transform of the autocorrelation function $g(\tau)$ of $F_q^k(t)$ [12]. We assume that the fluctuations are isotropic and have an exponentially decaying autocorrelation function

$$g(\tau) \equiv \langle F_q^k(t) F_{q'}^k(t + \tau)^* \rangle_t = \delta_{q,q'} \frac{(-1)^q f^2}{2k + 1} e^{-|\tau|/\tau_c},$$

where τ_c is the correlation time and f is the root mean square amplitude of the fluctuation. The power spectrum is then proportional to

$$J(\omega) \propto \frac{\tau_c}{1 + \omega^2 \tau_c^2}.$$

Under the assumption that in the case under discussion the fluctuations are determined by He lattice vibrations, $1/\tau_c$ will be on the order of the Debye frequency (10^{11} s^{-1}) in the b.c.c. phase of solid helium [13]. In this case $\omega \ll 1/\tau_c$ holds for both hyperfine (GHz) and Zeeman transitions (kHz) in the $6S_{1/2}$ ground state. As a consequence $J(\omega)$ is approximately constant for all these transitions (white noise regime). This assumption is well confirmed by our earlier observation that the longitudinal electronic spin relaxation rate γ_1 has a constant value of approximately 1 s^{-1} for Larmor frequencies ranging from 70 Hz to 4 MHz [5, 14]. The existence of additional noise sources, as, e.g. acoustic vibrations with considerably longer correlation times for which $\omega \tau_c \gg 1$ in the range of investigated frequencies can not be ruled out a priori. As the power density of these fluctuating fields $J(\omega) \rightarrow 0$ they are not able to drive sublevel transitions (population transfers), but contribute nonetheless to spin dephasing [10]. Because of the above mentioned independence of γ_1 on ω the case of ω being comparable to the fluctuation rate $1/\tau_c$ can be ruled out, so that in the following we will treat the problem for the two extreme cases $\omega \ll 1/\tau_c$ and $\omega \gg 1/\tau_c$ only.

In order to obtain an expression for the relaxation term $(\dot{\rho})_{rel}$ of the Liouville equation we have treated the relaxation mechanism as a Markovian process following the methods described,

e.g., in [12, 15, 16]. We present only the main formulas without discussing details. In the secular approximation $(\dot{\rho})_{rel}$ can be written in a compact operator form (see Ch. VIII, Eq. 42 in [12]) as

$$(\dot{\rho})_{rel} = -\frac{1}{2\hbar^2} \sum_{q,p} (-1)^q J(\omega_p^q) \left[(T_{-q,p}^k, [T_{q,p}^k, \rho]) \right], \quad (5.13)$$

where the operators $T_{q,p}^k$ are defined as expansion coefficients of the time dependence of the T_q^k according to

$$e^{iH_0 t/\hbar} T_q^k e^{-iH_0 t/\hbar} = \sum_p T_{q,p}^k e^{i\omega_p^q t}$$

in the interaction picture. In the special case of non equidistant Zeeman levels $|(F), M\rangle$ the summation index p represents any combination of quantum numbers $p = (F, M; F', M')$ and one has

$$T_{q,p}^k = \langle (F'), M' | T_q^k | (F), M \rangle | (F'), M' \rangle \langle (F), M | \quad (5.14)$$

and

$$\omega_p^q = \omega_p = \omega_{F',M'} - \omega_{F,M}, \quad (5.15)$$

where the $\omega_{F,M}$ are the eigenfrequencies of H_0 . Since we have assumed $J(\omega)$ to be constant it can be taken out of the sum. By applying the Wigner-Eckart theorem to the operators T_q^k one sees that Eq. 5.13 is proportional to the rate

$$\gamma = J(\omega) |\langle K || T^k || K \rangle|^2,$$

where $\langle K || T^k || K \rangle$ is the reduced matrix element of $T^k(K)$ with $K = S$ for $k = 1$ and $K = I$ for $k = 2$ respectively. We will use this relaxation rate γ as a parameter in the numerical calculations.

When the light field is switched off ρ relaxes towards the thermal equilibrium value

$$\rho_0 = \sum_{F,M} \rho_0^F | (F), M \rangle \langle (F), M |,$$

in which the relative populations of the two hyperfine ground states is determined by the Boltzmann factors $b_F = \exp(-\hbar\omega_F/k_B T)$. For a normalized total ground state population the thermal steady-state density matrices of the two hyperfine levels $F = 3, 4$ are given by $\rho_0^{F=3} = 1/(7+9b)$ and $\rho_0^{F=4} = b/(7+9b)$ where $b = b_4/b_3 = \exp(-\hbar\omega_{hfs}/k_B T)$. A rigorous treatment of the relaxation towards this thermal equilibrium distribution ρ_0 would require a quantum mechanical treatment of the helium lattice (heat reservoir) in the Hamiltonian of Eq. 5.12. In our calculations we have corrected Eq. 5.13 by appropriate Boltzmann factors, so that its steady-state solutions yield the correct thermal populations of the hyperfine levels [12, 15]. The population differences due to the Zeeman shifts inside each hyperfine multiplet F can be neglected at the temperature and field, at which the experiments were performed.

5.3.5 Relaxation of multi-quantum coherences

We have derived algebraic expressions relating the N -quantum coherence rates γ_{N+1} to the rate γ introduced above. We consider only transitions starting from the state $|(4), 4\rangle$, since the optical pumping process mainly populates this state. Evaluation of the right hand side of Eq. 5.13 then shows that the decay of the coherences is described by uncoupled differential equations of the form

$$(\dot{\rho}_{M,M'})_{rel} = -\gamma_{M,M'} \rho_{M,M'}.$$

We define the intrinsic relaxation rate γ_{N+1} of the N -photon coherence $\langle (4), 4-N | \rho | (4), 4 \rangle$ in Eq. 5.3 as $\gamma_{N+1} \equiv \gamma_{4,4-N}$. Table 5.1 shows the analytical results of this calculation for the cases

	$T^1(S)$	$T^2(I)$
$\omega\tau_c \ll 1$	$\frac{N+8}{36}$	$\frac{1}{15} \left(1 - \frac{3}{5} \left(\frac{N-4}{4}\right)^2\right)$
$\omega\tau_c \gg 1$	$\frac{1}{288}N^2$	$\frac{3}{175} \left(2 - \frac{1}{4}(N-4)^2 + \frac{(N-4)^4}{128}\right)$

Table 5.1: $\gamma_{N+1} \equiv \gamma_{4,4-N}$ in units of γ for the four cases of relaxation under discussion.

of relaxation considered here. The same results are displayed as ratios γ_{N+1}/γ_2 in Fig. 5.3. One sees that for relaxation dominated by the $T^1(S)$ perturbation, the relaxation rates grow monotonically with N (linearly in the limit $\omega\tau_c \ll 1$ and quadratically in the limit $\omega\tau_c \gg 1$), while for the quadrupole relaxation mechanism $T^2(I)$ there is a maximum in the relaxation rates and in the limit $\omega\tau_c \ll 1$ the 8-photon coherence has even a slower relaxation than the one-photon coherence.

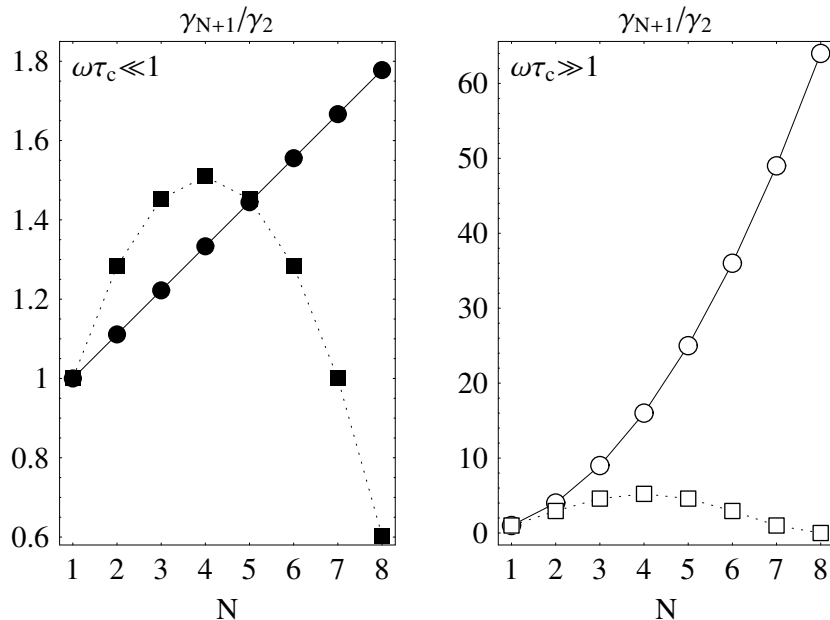


Figure 5.3: γ_{N+1}/γ_2 for the four relaxation mechanism under discussion. $\gamma_{N+1} \equiv \gamma_{4,4-N}$ is defined as the relaxation rate of the $\rho_{4,4-N}$ coherence. $\omega\tau_c \ll 1$: $T^1(S)$ (filled circles) and $T^2(I)$ (filled squares); $\omega\tau_c \gg 1$: $T^1(S)$ (open circles) and $T^2(I)$ (open squares). Corresponding points are joined by lines to guide the eye.

5.3.6 Gain in spectroscopic sensitivity

We are now ready to estimate the gain of spectroscopic sensitivity of the N -photon resonances compared to the $N = 1$ single photon resonance for different relaxation schemes. As in section 5.2.2 we assume that under optimal conditions the amplitudes of the multi-photon resonances in each generation are independent of N , so that the gain is basically determined by the ratio of linewidths $G_N = \gamma_2/\gamma_{N+1}N$ defined in Eq. 5.5. Fig. 5.4 shows the resulting values of G_N for the four relaxation processes. We have also calculated the gain factor G_N for the simplest case of relaxation, in which the decay of the coherences is due to optical pumping only. The relaxation

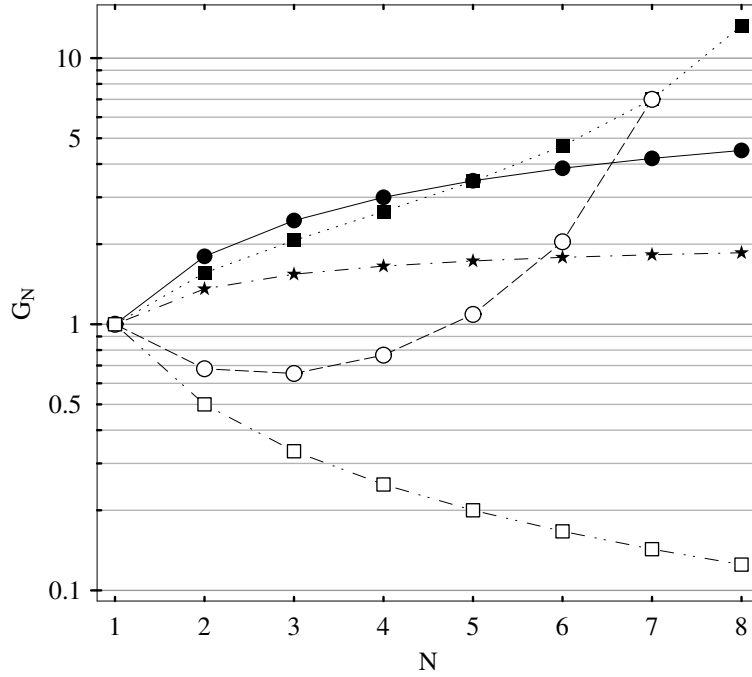


Figure 5.4: Estimations for the gain in spectroscopic sensitivity G_N of the N -photon resonances with respect to the single photon resonance for several multipole relaxation mechanisms and optical pumping relaxation: For $\omega\tau_c \ll 1$: $T^1(S)$ (filled circles) and, $T^2(I)$ (filled squares); for $\omega\tau_c \gg 1$: $T^1(S)$ (open circles) and, $T^2(I)$ (open squares); and for the relaxation by optical pumping only (stars). Corresponding points are joined by lines to guide the eye. The values are calculated from Eq. 5.5 of Sec. 5.2.2.

rates γ_{N+1} for that case are obtained from Eq. 5.10. Optical power broadening was the only relaxation mechanism considered in the work by Pazgalev and Alexandrov [2]. From Fig. 5.4 it can be seen that G_N strongly depends on the underlying relaxation mechanism of the spin ensemble. For a pure dipolar dephasing relaxation mechanism described by $T^1(S)$ in the limit $\omega\tau_c \gg 1$ one even finds a strong loss in sensitivity, whereas the highest gain is predicted for a quadrupolar relaxation mechanism described by $T^2(I)$ in the limit $\omega\tau_c \ll 1$. It is also interesting to note that in the case of quadrupolar relaxation in the limit $\omega\tau_c \gg 1$ the calculation shows that $\gamma_9 = 0$, i.e., that the $N = 8$ -photon coherence between the states $M = 4$ and $M' = -4$ is not effected by the relaxation interaction.

It is further interesting to note that only a factor of approximately two can be won in resolution by using multiphoton resonances when the decay of spin coherence is dominated by optical pumping.

The data given in the figure can only serve as a rough estimate, as they merely consider magnetic resonance transitions originating from the $|(4), 4\rangle$ state and as they rely on the validity of the algebraic formulas given in Sec. 5.2.2. The complex steady state population distribution among the ground states resulting from the interplay of magnetic and optical interactions has not been considered. A more realistic estimation of $G_N = R_N/R_1$ can only be achieved by complete calculations of the ODMR spectra from the solutions of the steady state master equation (5.6) for realistic parameters. The results of such calculations will be presented below.

5.3.7 Technical details of the calculations

We have calculated the multi-photon ODMR spectra of Cs by numerically solving Eq. 5.6 for the density matrix ρ describing the 16 sublevels of the $6S_{1/2}$ ground state hyperfine structure. Since all coherences between the two hyperfine levels $F = 3$ and $F = 4$ are neglected this calculation is equivalent to solving 130 coupled linear algebraic equations. From ρ the ODMR signal $\mathcal{F}(\rho)$ could then be obtained from Eq. 5.11. The system of equations was first formulated in a symbolic way using Mathematica [17] and then solved, after replacing all parameters by appropriate values, by a sparse-matrix solving algorithm, implemented in Mathematica. An important task consisted in determining from the rather complicated ODMR spectra the amplitudes and widths of single peaks. For this purpose we differentiated the system of equations algebraically with respect to the radio frequency ν_{rf} . After inserting the previously obtained steady-state solutions for the elements of ρ , a new system of 130 equations is obtained, whose solutions yield $\partial\rho/\partial\nu_{rf}$. Here we used the interchangeability of the differentiations with respect to time and frequency in the master equations. Since \mathcal{F} is linear in ρ the derivative of the fluorescence rate with respect to the r.f. frequency is given by $\partial\mathcal{F}/\partial\nu_{rf} = \mathcal{F}(\partial\rho/\partial\nu_{rf})$. By repeating this procedure higher derivatives of \mathcal{F} with respect to the frequency can be obtained. From the first two derivatives the amplitudes and widths of the Lorentzians are easily found, if the underlying background can be regarded as locally flat. This condition is well fulfilled for the non saturated N -photon peaks sitting on top of power broadened lower order peaks.

5.4 Experiment

5.4.1 Experimental setup and data recording

The experimental procedure used is an improved version of the one described previously[1]. Only the main features and the modifications will be addressed here. The experiments were performed on Cs atoms implanted in a helium crystal contained in a pressure cell immersed in a superfluid helium bath cooled by pumping on the bath (Fig. 5.5). Quartz windows provide optical access from three orthogonal directions. The cesium atoms are implanted into the crystal from a metal target by means of laser ablation. The temperature of the crystal is actively stabilized to $1.5K$ at a level of 10^{-5} K over intervals of 100 seconds [18]. The cesium atoms are excited on the D_1 transition ($6S_{1/2} \rightarrow 6P_{1/2}$) at 850 nm with a beam from a single-mode extended cavity diode laser. The absorption is monitored by detecting the $6P_{1/2} \rightarrow 6S_{1/2}$ fluorescence light at 888 nm using a cooled, biased avalanche-photodiode. An interference filter suppresses scattered laser light. A set of three Helmholtz coils inside the pressure cell allows the application of r.f. fields in any direction. Three layers of μ -metal surround the cryostat and suppress laboratory magnetic fields by more than three orders of magnitude.

A new feature of the set-up is the generation of the B_0 field by a pair of superconductive Helmholtz coils operated in a self-sustained (persistent) current mode. After injecting a current from an external current source the coils are bypassed by closing a temperature-controlled super-switch (graphite resistor) mounted in an evacuated copper housing placed at the bottom of the helium bath.

The data acquisition was also improved by significantly reducing the scan speed. In our previous experiments spectral distortions due to fast scanning led to significantly asymmetric line shapes. The sweep duration was now increased from 20 s to 100 s while reducing at the same time the swept frequency span from 50 kHz to 15 kHz. This implied that only multi-photon resonances of the type $|(4), 4\rangle \rightarrow |(4), 4 - N\rangle$ in the $F = 4$ multiplet were recorded. The non-observation of the lines in the $F = 3$ multiplet constitutes nonetheless a minor loss of information, since due to the optical pumping process almost all population is transferred to

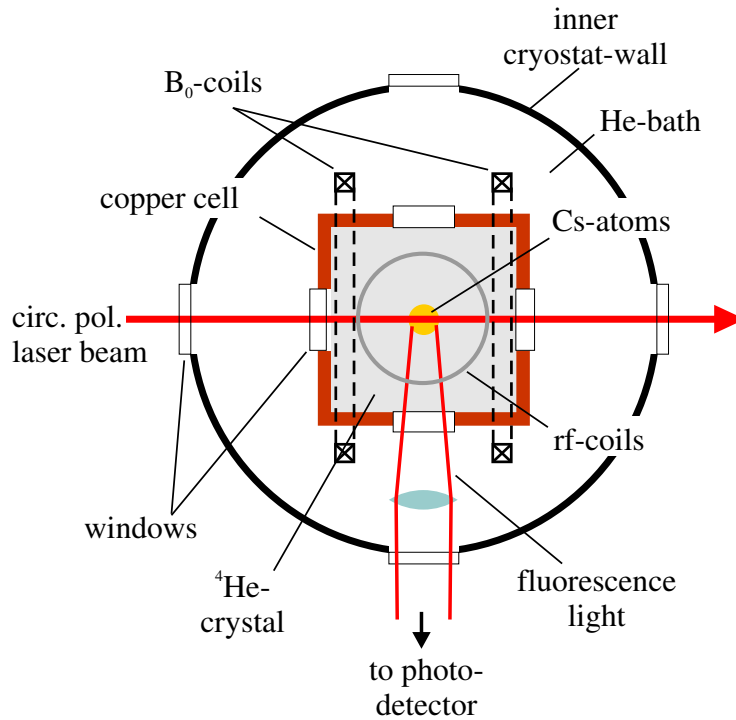


Figure 5.5: Section (top view, not to scale) through the helium containing part of the cryostat. The isolation vacuum part and a liquid nitrogen shield are not shown.

the $|(4), 4\rangle$ state, so that the $|(3), 3\rangle \rightarrow |(3), 3 - N\rangle$ transitions are in general much weaker and carry no relevant additional information.

5.4.2 Experimental results

Fig. 5.6 shows a series of eight ODMR-spectra taken in the b.c.c. phase of solid ^4He at a temperature of 1.501 K and a pressure of 26.71 bar. The spectra were recorded in a field of 1.0414 mT by scanning the frequency of the r.f. field over the multiphoton resonances of the $F = 4$ multiplet. The origin of the frequency axis corresponds to the frequency of the $|(4), 4\rangle \rightarrow |(4), 3\rangle$ one-photon transition ($\nu_{ref} = 3633.72$ kHz). The spectra were recorded for different r.f. powers, chosen experimentally such that the multi-photon lines of a given order N present the dominant feature of the spectrum. The corresponding relative r.f. field strengths for the subsequent spectra (top to bottom in Fig. 5.6) were 10000 : 6662 : 4436 : 2826 : 1669 : 933 : 192 : 44.

The extension of the scan time is however accompanied by a diminished signal to noise ratio. In the raw data of the presented measurements the multiphoton spectra are superposed on a monotonously decreasing fluorescence signal, which is due to a loss of atoms by recombination of the implanted Cs atoms during the r.f. sweep with clusters and/or other Cs atoms. Before each sweep these clusters were dissociated by applying a Nd:YAG-laser pulse focused into the Cs doped volume. The atomic signal then drops on a time scale of several tens of seconds, which implies that the signal to noise ratio of the data points steadily drops as the scan proceeds. Hence the data points show a steadily decreasing signal to noise ratio during a sweep. The ordinate of the spectra presented in Fig. 5.6 represents $\mathcal{F}/\mathcal{F}_b - 1$, where \mathcal{F} is the recorded fluorescence and \mathcal{F}_b the background fluorescence underlying the magnetic resonance spectra proper. \mathcal{F}_b was

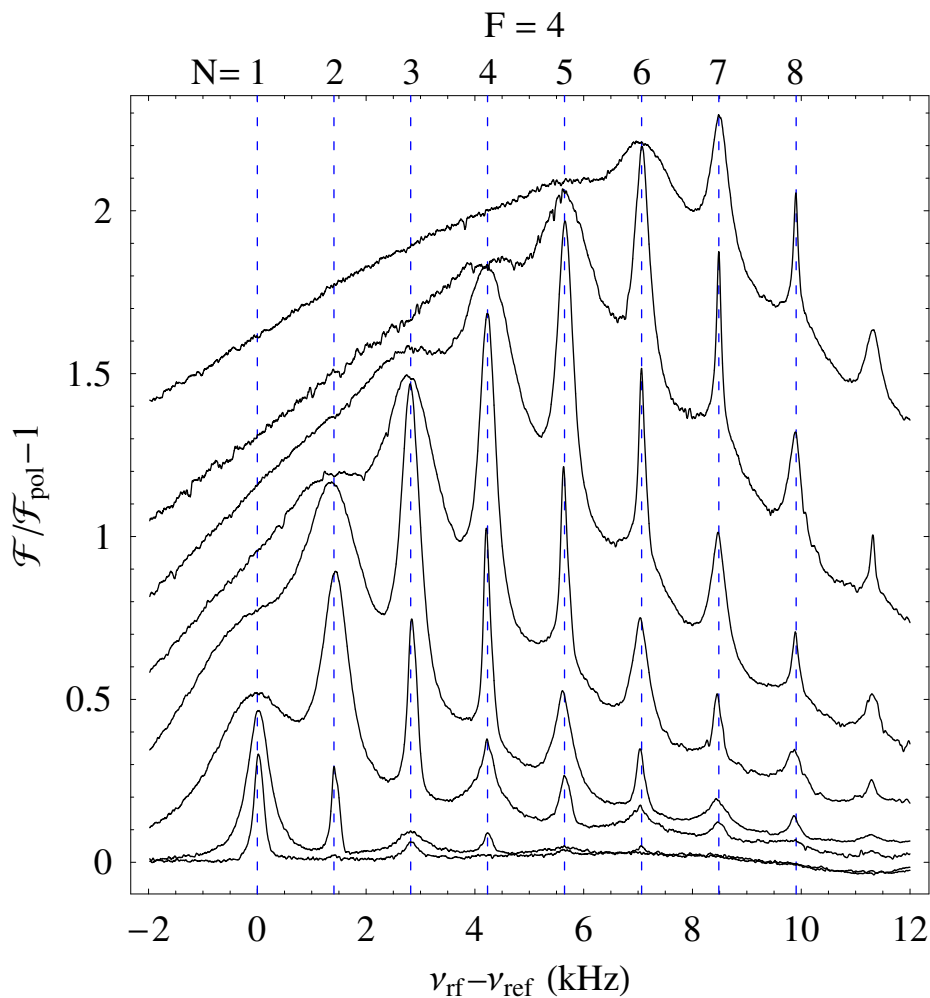


Figure 5.6: Background corrected (see the text) measured multiphoton resonance spectra in a field B_0 of 1.0414 mT. The origin of the frequency axis corresponds to the frequency of the $|4, 4\rangle \rightarrow |4, 3\rangle$ one-photon transition ($\nu_{\text{ref}} = 3633.72$ kHz). Dashed lines indicate the positions of the N -photon resonances $|4, 4\rangle \rightarrow |4, 4 - N\rangle$. The r.f. power is increased (ratios given in the text) in each of the eight spectra going from bottom to top in such a way that the newly appearing N -photon lines show an optimal spectral resolution.

determined by fitting an appropriate function to the time dependent background. In this way the normalization $\mathcal{F}/\mathcal{F}_b - 1$ does not only remove the background, but it also corrects for the loss of atoms and hence for the apparent loss of signal amplitude during the scan. The r.f. frequency was swept from higher to lower frequencies, which explains the larger noise levels at low r.f. frequencies in Fig. 5.6. This procedure of normalizing the signals has the further advantage that the experimental signal amplitudes can be compared to the corresponding theoretical spectra on an absolute scale.

5.4.3 Comparison with the calculations

We reproduced the experimental data by calculating the ODMR spectra according to the method given in Sec. 5.3.1. Since the linewidths of the measured resonances were still dominated by the technical and optical pumping broadening rather than by intrinsic relaxation processes, the later could be neglected, i.e., we set $\gamma = 0$.

Beside $B_{r,f}$ which is different for all eight spectra, three common parameters, viz. B_0 , γ_p , and the parameter φ , characterizing the degree of circular polarization, entered the calculations. By fitting Lorentzians to the measured multi-photon spectra (Fig. 5.6) we inferred B_0 from the line positions in accordance with the Breit-Rabi formula taking the perturbation of the hyperfine constant by the helium matrix into account [1]. A typical value for φ of 0.5 rad could be obtained from earlier measurements [14]. From the measured light intensity of 78 mW/cm² we inferred the optical pumping rate to be $\gamma_p \approx 390 \text{ s}^{-1}$ using again results of recent experiments [4]. Fig. 5.7 shows the calculated ODMR spectra. By representing the quantity $\mathcal{F}/\mathcal{F}_{\text{unpol}} - 1$ the theoretical results are commensurable with the experimental spectra of Fig. 5.6 on an absolute scale.

Since we do not have a precise calibration of the r.f. field inside the pressure cell, we adjusted $B_{r,f}$ for the uppermost curve in Fig. 5.7 so that we achieved optimal consistency with the corresponding measured spectrum. This was at $B_{r,f} = 2.57 \mu\text{T}$, which is in good agreement with the value we estimated from the output current of our r.f. generator and the dimensions of the r.f. field coils. The other curves were then obtained at lower r.f. fields, with amplitudes in the same ratios as in the experiment. All other parameters were kept fixed.

The peaks of the calculated spectra whose widths are determined by r.f.-power broadening reproduce well the overall structure of the experimental data with respect to their relative heights and shapes, whereas the lesser broadened peaks are too high in amplitude and too small in width. As we assign this to small magnetic field inhomogeneities in the experiment we take such inhomogeneities into account in the calculations by convoluting the theoretical data with a Lorentzian distribution of the magnetic fields around the average field value. A FWHM of 70 Hz of the convolution profile (corresponding to a field inhomogeneity of $2 \cdot 10^{-5}$) yielded the best agreement between measurement and theory. Not only is the agreement excellent regarding the different relative heights and widths of the peaks, but the amplitudes of the spectra also coincide on an absolute scale. We stress again that a single set of parameters was used for all spectra. A residual small discrepancy of the absolute signals may be assigned to stray fluorescence light of non-atomic origin and/or to electronic offsets, which both introduce errors in the normalization procedure of the experimental signals. Compared to our previous study [1], now even details of the calculated spectra, such as the reduced $N = 2$ -photon peak height in the second (from the bottom) spectrum fit well the experimental data, thus confirming the suitability of our model.

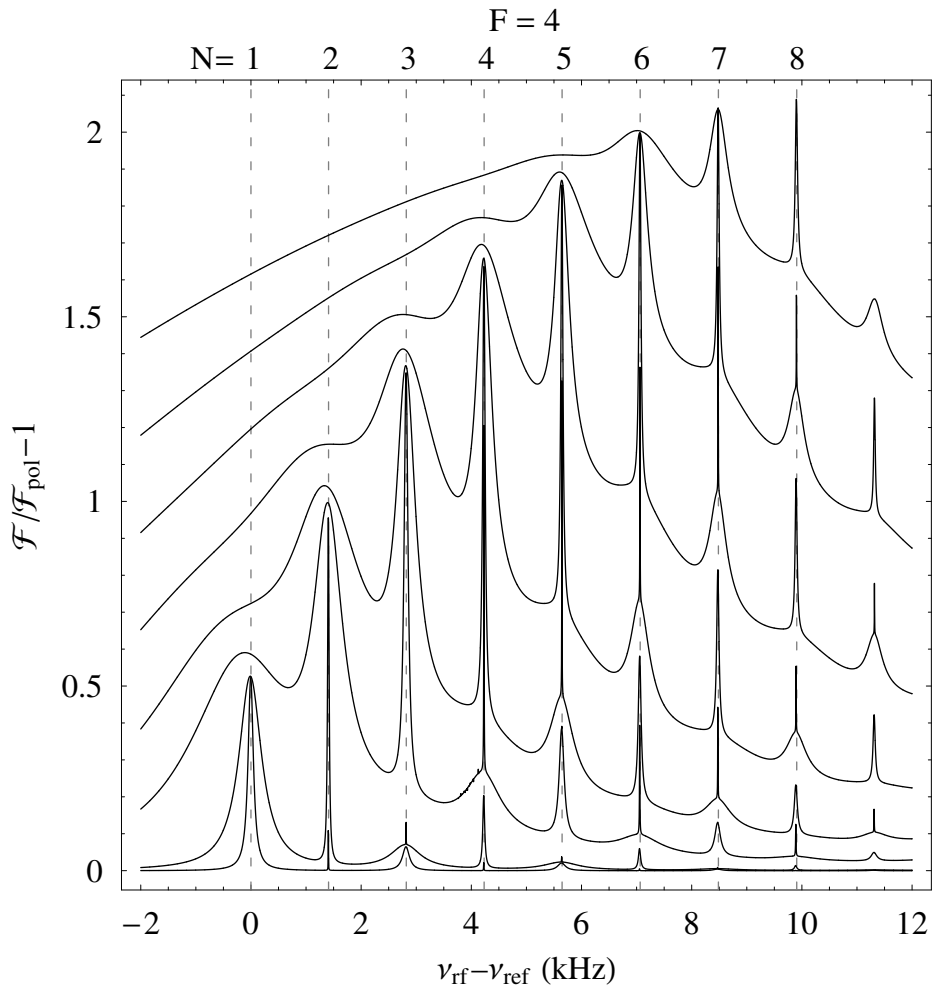


Figure 5.7: Multi-photon spectra calculated by solving the master equation Eq. 5.6 for various values of $B_{r,f}$. The fixed parameters B_0 , γ_p , and φ were adjusted to the experimental values. $B_{r,f}$ was changed in the same proportions as in the experiment shown in Fig. 5.6. No intrinsic relaxation was considered and the linewidths are determined by r.f. and optical pumping broadening only. The fluorescence rate \mathcal{F} is represented in units of the thermal equilibrium fluorescence rate \mathcal{F}_0 of the unpolarized spin ensemble.

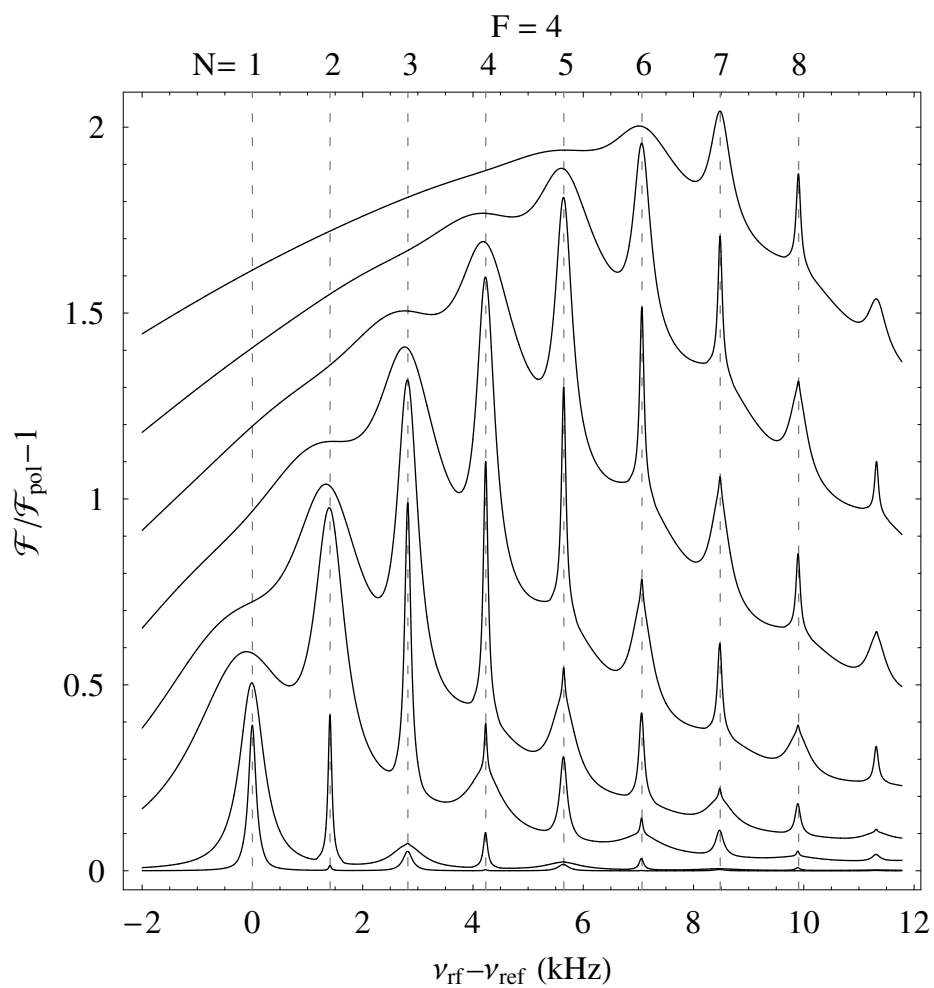


Figure 5.8: The calculated data of Fig. 5.7 convoluted with a Lorentzian shaped curve with a FWHM of 70 Hz. The convolution mimics the influence of the technical broadening which is not included in the master equation calculation leading to the results shown in Fig. 5.7 .

5.5 Effect of intrinsic multipole relaxations on the multi-photon spectra

One of our goals was to extract information about the mechanism which determines the spin relaxation of Cs atoms in the cubic phase of ^4He by comparing experimental multi-photon spectra to theoretical spectra based on different relaxation models. This difficult goal could not yet be reached because the experimental line shapes are dominated by an inhomogeneous technical broadening, whose origin lies most probably in small (we talk about effects on the order of $\Delta B/B \approx 10^{-5}$) residual magnetic field inhomogeneities. In future experiment it should be possible to overcome this problem. In order to demonstrate nonetheless the anticipated consequences of different relaxation mechanism we calculated the multiphoton spectra for ideal conditions, i.e., for a perfectly homogeneous magnetic field.

We consider the two cases of dipolar and quadrupolar perturbations, described by $T^1(S)$ and $T^2(I)$ respectively, and restrict the discussion to the limit $\omega\tau_c \ll 1$, for which the fluctuating interactions not only lead to transverse spin relaxation, but also to longitudinal relaxation by inducing sublevel transitions. In this case the parameter γ , which characterizes the strength of the relaxation mechanism under consideration can be inferred from the experimentally determined longitudinal relaxation rate γ_1 at which $\langle J_z \rangle$ relaxes. In the limit $\omega\tau_c \gg 1$ only transverse spin relaxation occurs, and no reasonable quantitative predictions of γ can be made with our present knowledge. In order to determine γ from the experimental value of γ_1 we solved $\dot{\rho} = (\dot{\rho})_{rel}$ for both cases of multipolarity assuming $\rho_{4,4}(t=0) = 1$ as initial condition for the normalized density matrix. From $\rho(t)$ the temporal evolution of $\langle J_z \rangle$ was obtained.

In the case of $T^1(S)$ relaxation we were able to derive the following algebraic function that describes the decay of $\langle J_z \rangle$

$$\langle J_z \rangle(t) = \frac{1}{62} (24e^{-\frac{4}{9}\gamma t} + 7e^{-\frac{1}{72}\gamma t}). \quad (5.16)$$

The polarization is thus seen to have two decay channels whose rates differ by a factor of 32. Moreover, the slow channel is responsible for the decay of 77% of the initial polarization. The time scales in our previous T_1 measurements were too small to reveal the presence of two strongly differing time scales, and the question arises, which of the two channels should be identified with the measured values of $\gamma_1 \approx 1 \text{ s}^{-1}$. As in the experiments a large amplitude decay of the polarization was observed it seems natural to identify the experimental γ_1 value with $\frac{4}{9}\gamma$, which yields $\gamma = 2.25 \text{ s}^{-1}$. The second component thus has a decay time of 32 seconds. This relaxation rate is hard to measure as it is comparable to the loss rate of atoms due to recombination as described in Sec. 5.4.2. In the case of $T^2(I)$ relaxation we did not succeed to derive an algebraic function describing the decay of $\langle J_z \rangle$. However, numerical calculations suggest that $\langle J_z \rangle$ has an exponential decay with a single rate, for which comparison with the experimental decay yields $\gamma \approx 88.3 \text{ s}^{-1}$.

These values of γ form the basic input parameters, besides the experimentally determined parameters B_0 and γ_p , for the theoretical calculations. As already stated several times the experimental spectra were limited by technical line broadening. The pump rate γ_p in the experiments was chosen in such a way that the broadening due to optical pumping was slightly smaller than the technical linewidth of the unsaturated multi-photon resonances. If in future experiments the inhomogeneous broadening can be substantially reduced or eliminated, then, of course, the optimal pump rate for the experiments should be reduced correspondingly. For this reason we decided to calculate the spectra comparing the influence of the perturbation multipolarity for a light intensity, which is 10 times lower than in the experiments described above. Figs. 5.9 and 5.10 show the spectra obtained with $\gamma_p = 39 \text{ s}^{-1}$ for $T^1(S)$ and $T^2(I)$ relaxation respectively.

The parameter distinguishing the curves in these figures is the r.f. field amplitude B_{rf} . For each curve B_{rf} was chosen such as to maximize the spectroscopic resolution of the multi-photon generation that emerged in that spectrum.

Note that we have also calculated the same spectra as in Figs. 5.9 and 5.10 with $\gamma_p = 390 \text{ s}^{-1}$, i.e., the pump rate used in the present experiments. As anticipated the resulting resonance systems look identical for $T^1(S)$ and $T^2(I)$ relaxation, as the widths are dominated by optical pumping broadening. These spectra are not shown.

We determined the amplitude A_N and widths (FWHM) $\Delta\nu_N$ of the dominant non-saturated multi-photon line in each trace of Figs. 5.9 and 5.10. The dependences of the relative amplitudes $A_N/A_{N=1}$ and relative inverse widths $(1/\Delta\nu_N)/(1/\Delta\nu_1)$ on the multi-photon order N are shown in Figs. 5.11 a,b.

In the simplified discussion of magnetic resonance in sections 5.2.2 and 5.3.6 the gain in spectroscopic sensitivity $G_N = \Delta\nu_1/\Delta\nu_N = \gamma_{N+1}/\gamma_2 N$ depended only on the relative line widths. The data in Fig. 5.11 a show the ratios of linewidths from the present complete calculation. Note that the qualitative N -dependence is similar to the one shown in Fig. 5.4 derived from the simplified treatment, which did not consider the optical pumping process by which coherences are also destroyed.

The optical pumping process is also responsible that now the amplitudes have a significant N -dependence (Fig. 5.11 b) due to the complex interplay of the production of population differences by optical pumping and their destruction by saturated lower order multi-photon transitions. In the discussion of sections 5.2.2 and 5.3.6 it was assumed that all population was in the $|(4), 4\rangle$ state, which implied that the amplitudes for optimal sensitivity were found to be N -independent.

As both the amplitudes and the widths of the multi-photon resonances depend on N the gain in spectroscopic resolution has to be calculated according to

$$G_N = \frac{A_N}{\Delta\nu_N} / \frac{A_1}{\Delta\nu_1}.$$

The corresponding dependence is shown in Fig. 5.11 c. For the case of the dipolar $T^1(S)$ relaxation the gain grows in a monotonous way to reach a maximum value of approximately 8 for the eight-photon transition. It is interesting to note that this factor corresponds to the naive expectation discussed in the introduction. In the case of quadrupolar $T^2(I)$ relaxation a maximum gain of approx. 5.6 is found for the five-photon process and there is a loss of sensitivity for higher order processes.

5.6 Summary and outlook

We have performed a theoretical analysis of the influence of stochastic spin perturbing interactions of dipolar and quadrupolar symmetry on the spectra of multi-photon transitions in the ground state of cesium in solid helium. Algebraic results for the multipole relaxation rates were derived for both cases in the limits $\omega\tau_c \gg 1$ and $\omega\tau_c \ll 1$. Numerical results for the multi-photon spectra taking optical pumping, magnetic resonance and relaxation into account were obtained. The results were used to predict the gain in spectroscopic resolution of multi-photon transitions and yielded a maximum gain factor of 8 for quadrupolar relaxation. Unfortunately the quality of the present experimental spectra is not sufficient for discriminating between these two most likely relaxation mechanisms. However the experimental spectra can be well reproduced by the calculations taking field inhomogeneities into account. In the future we plan to reduce the magnetic field inhomogeneities by appropriate shim coils and by replacing recently identified remote parts of the cryostat which show a residual magnetization.

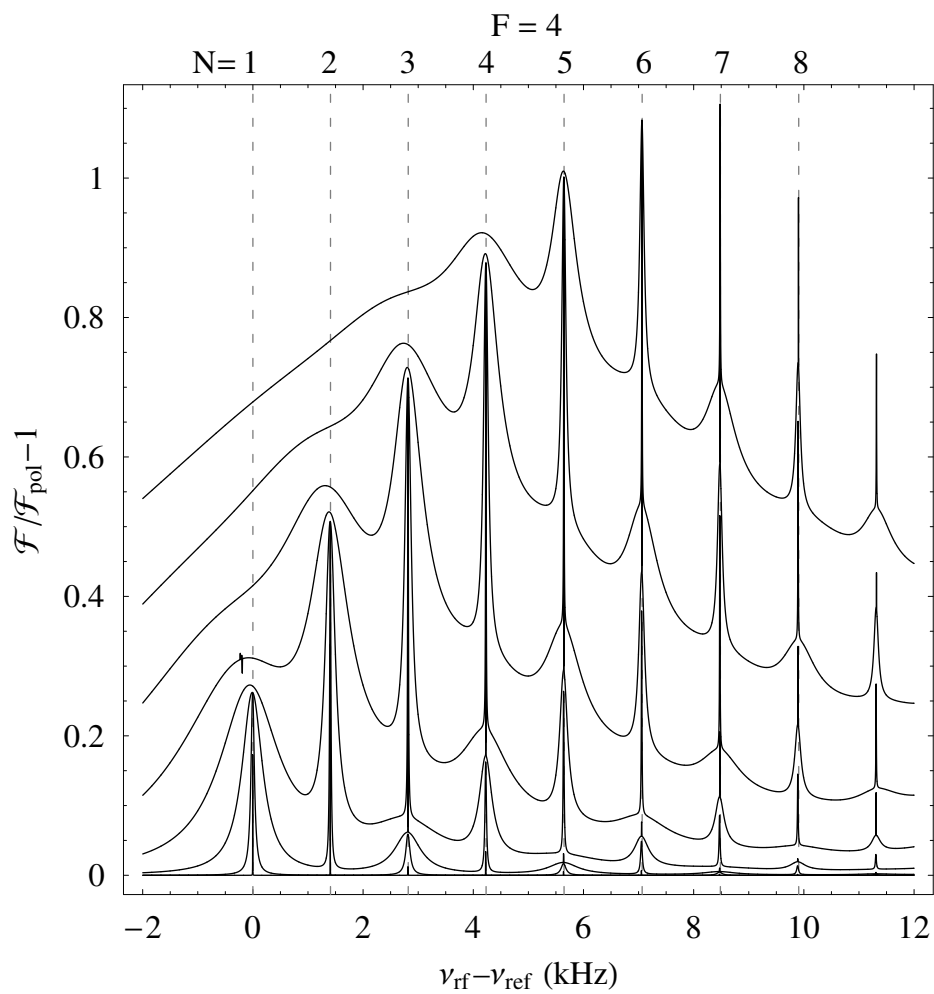


Figure 5.9: Calculated multi-photon spectra for $T^1(S)$ relaxation in the limit of $\omega\tau_c \ll 1$. The optical pumping rate γ_p is ten times lower than in the experiment.

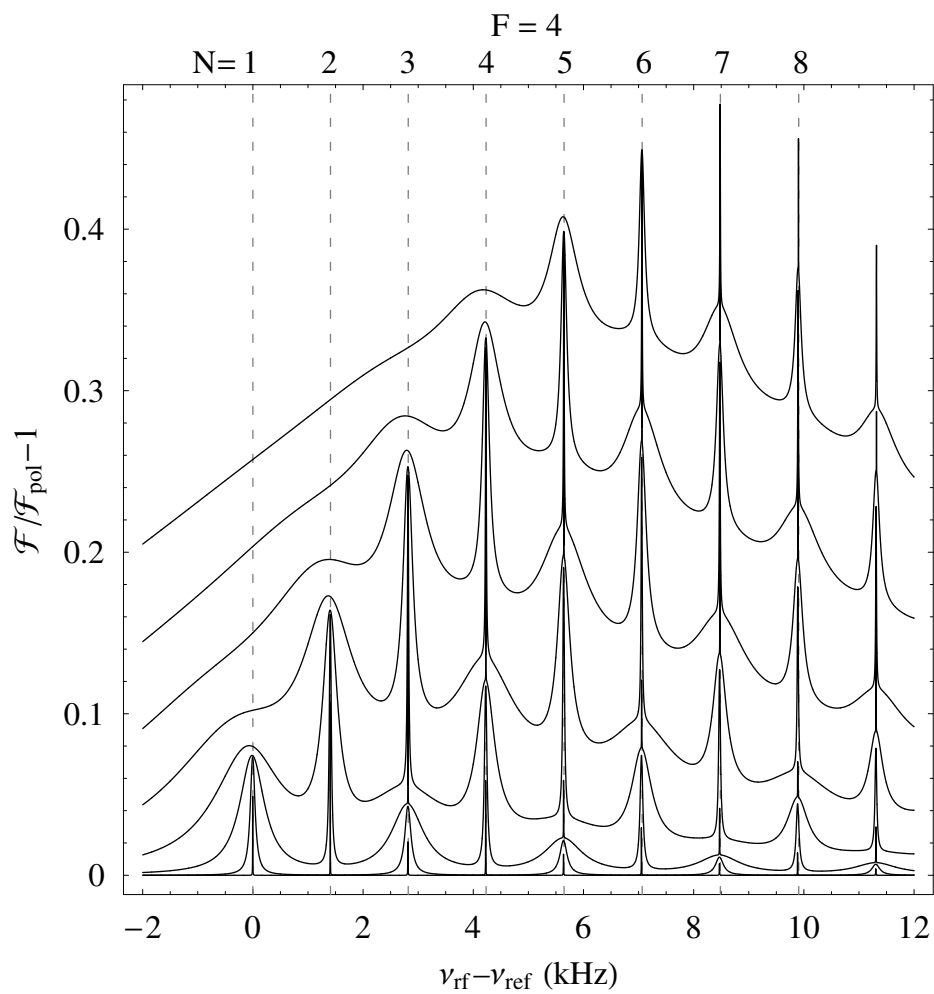


Figure 5.10: Calculated multi-photon spectra for $T^2(I)$ relaxation in the limit of $\omega\tau_c \ll 1$. The optical pumping rate γ_p is ten times lower than in the experiment.

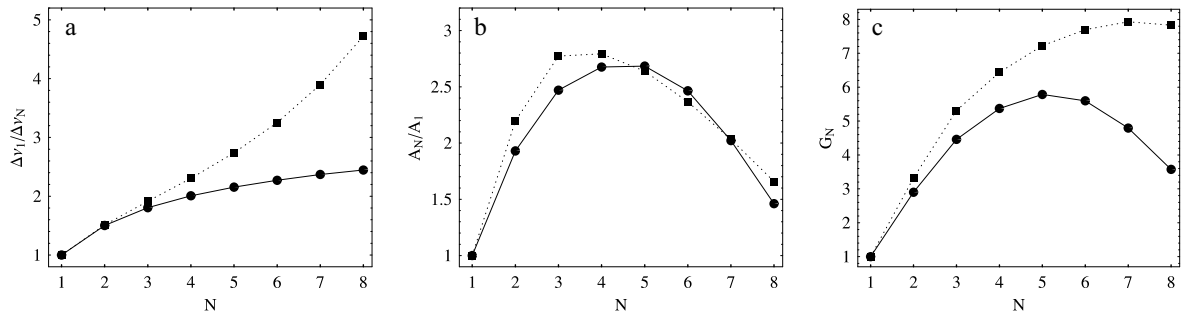


Figure 5.11: **a** Ratio of inverse linewidths $\frac{1}{\nu_N}/\frac{1}{\nu_1}$ determined from the spectra of Fig. 5.9 and Fig. 5.10. Filled circles: $T^1(S)$ -relaxation, filled squares: $T^2(I)$ -relaxation. **b** Ratio of amplitudes A_N/A_1 . **c** Gain of spectroscopic resolution G_N . Note that G_N can be calculated by multiplying the corresponding data in **a** and **b**.

Of course it would be interesting to measure the relaxation rates of the individual multi-quantum coherences directly as their N -dependence offers the most promising way to identify the multipolarity of the perturbation (Fig. 5.11a). Another promising approach to this goal is the recording of free-induction decay signals following the selective excitation of a given resonance. The relative intensities of the single-photon lines at low r.f. power, which are barely visible on Figs. 5.9 and 5.10 seem to offer yet another characteristic feature, which reflects the multipolarity of the interactions. Work along these directions is in progress.

5.7 Appendix: Ground state master equation for optical pumping

The density matrix σ of the ground $6S_{1/2}$ and excited $6P_{1/2}$ states has the form

$$\sigma = \begin{pmatrix} \sigma_{gg} & \sigma_{ge} \\ \sigma_{eg} & \sigma_{ee} \end{pmatrix},$$

where $\sigma_{ab} = P_a \sigma P_b$ with $a, b = e, g$. σ_{gg} is identical with ρ of the main text. We assume the substates inside a level to be degenerate in the sense that their hyperfine and Zeeman structure cannot be resolved by optical means. In the rotating wave approximation the atom light interaction Hamiltonian is then given by

$$H_{AL} = \hbar \begin{pmatrix} 0 & D_{ge} \\ D_{eg} & -\Delta \end{pmatrix}, \quad (5.17)$$

where $\Delta = \omega - \omega_{eg}$ is the detuning of the laser frequency from the optical transition frequency ω_{eg} . We describe relaxation processes by the rates $(\dot{\sigma}_{ab})_{rel}$ with

$$\begin{aligned} (\dot{\sigma}_{ee})_{rel} &= -\Gamma \sigma_{ee} \\ (\dot{\sigma}_{eg})_{rel} &= -1/2(\Gamma + \gamma) \sigma_{eg} \\ (\dot{\sigma}_{ge})_{rel} &= -1/2(\Gamma + \gamma) \sigma_{ge} \\ (\dot{\sigma}_{gg})_{rel} &= \Gamma \frac{2L+1}{L} \sum_{q=-1}^1 (C_{-q}^1)_{ge} \sigma_{ee} (C_q^1)_{eg}. \end{aligned} \quad (5.18)$$

$1/\Gamma$ is the lifetime of the $6P_{1/2}$ level and γ the homogeneous width of the optical transition. $L = 1$ is the orbital angular momentum of the excited state. Since in this experiment $\gamma \gg \Gamma$, we will neglect the $\Gamma/2$ terms in the relaxation of the optical coherences.

The Liouville equation for the atom-light interaction is

$$\dot{\sigma} = -i/\hbar[H_{AL}, \sigma] + (\dot{\sigma})_{rel}. \quad (5.19)$$

After inserting Eq. 5.17 and Eq. 5.18 into Eq. 5.19 and setting $\dot{\sigma}_{eg} = 0$ and $\dot{\sigma}_{ge} = 0$ (adiabatic elimination) we get for σ_{gg} and σ_{ee} :

$$\dot{\sigma}_{ee} = D_{eg}\sigma_{gg}D_{ge}\frac{2\gamma}{\Delta^2 + (\gamma/2)^2} - \Gamma\sigma_{ee} \quad (5.20)$$

$$\begin{aligned} \dot{\sigma}_{gg} = & -i\left(\frac{D_{ge}D_{eg}\sigma_{gg}}{\Delta + i\gamma/2} - \frac{\sigma_{gg}D_{ge}D_{eg}}{\Delta - i\gamma/2}\right) \\ & + (\dot{\sigma}_{gg})_{rel}. \end{aligned} \quad (5.21)$$

Here we have neglected all terms describing stimulated transitions from the excited state to the ground state, which is justified because of the very large homogeneous linewidth (10 nm) and the modest laser intensities (several 10 mW/cm²) used. Since the lifetime of the excited state ($1/\Gamma \approx 10^{-8}$ s) is very short, we further neglect the evolution of σ_{ee} under the influence of the magnetic fields. In the steady state $\dot{\sigma} = 0$ we can solve Eq. 5.20 for σ_{ee} and insert the result into $(\dot{\sigma}_{gg})_{rel}$ of Eq. 5.21. We get

$$\begin{aligned} \sigma_{ee} &= \frac{1}{\Gamma} \frac{\gamma}{\Delta^2 + (\gamma/2)^2} D_{eg}\sigma_{gg}D_{ge} \\ \dot{\sigma}_{gg} &= -i\left(\frac{D_{ge}D_{eg}\sigma_{gg}}{\Delta + i\gamma/2} - \frac{\sigma_{gg}D_{ge}D_{eg}}{\Delta - i\gamma/2}\right) \\ &+ \frac{3\gamma}{\Delta^2 + (\gamma/2)^2} \sum_{q=-1}^1 (C_{-q}^1)_{ge} D_{eg}\sigma_{gg}D_{ge} (C_q^1)_{eg}. \end{aligned} \quad (5.22)$$

The fluorescence rate \mathcal{F} is then calculated to be

$$\mathcal{F} = \Gamma \text{tr}(\sigma_{ee}) = \frac{\gamma}{\Delta^2 + (\gamma/2)^2} \text{tr}(D_{eg}\sigma_{gg}D_{ge}). \quad (5.23)$$

By setting $\Delta = 0$ in Eq. 5.22 and Eq. 5.23 we get the expressions Eqs. 5.10 and 5.11 of the main text.

Acknowledgments

This work was supported by a grant of the Schweizerischer Nationalfonds.

We thank S. Ulzega for helping during the experiment preparation and data taking.

References

- [1] D. Nettels, R. Müller-Siebert, Simone Ulzega, and Antoine Weis. Multiphoton processes in the Zeeman structure of atomic Cs trapped in solid helium. Accepted for publication by Appl. Phys. B.
- [2] A. S. Pazgalev and E. B. Alexandrov. Exact solution of the problem of multi-quantum resonances in Zeeman structure of ^{133}Cs and ^6Li atoms. *Optics and Spectroscopy*, 86(1): 6–10, 1999.
- [3] S. I. Kanorsky, M. Arndt, R. Dziewior, A. Weis, and T. W. Hänsch. Optical spectroscopy of atoms trapped in solid helium. *Phys. Rev. B*, 49(5):3645, 1994.
- [4] S. Lang, S. I. Kanorsky, T. Eichler, R. Müller-Siebert, T. W. Hänsch, and A. Weis. Optical pumping of Cs atoms in solid ^4He . *Phys. Rev. A*, 60(5):3867, 1999.
- [5] M. Arndt, S. I. Kanorsky, A. Weis, and T. W. Hänsch. Long electronic spin relaxation times of Cs atoms in solid ^4He . *Phys. Rev. Lett.*, 74(8):1359, 1995.
- [6] S. I. Kanorsky, S. Lang, S. Lücke, S. B. Ross, T. W. Hänsch, and A. Weis. Millihertz magnetic resonance spectroscopy of Cs atoms in body-centered-cubic ^4He . *Phys. Rev. A*, 54(2):R1010, 1996.
- [7] H. Salwen. Resonance transitions in molecular beam experiments. I. general theory of transitions in a rotating magnetic field. *Rev. Mod. Phys.*, 99(4):1274–1286, 1955.
- [8] J. Hermann and S. Swain. Resonance lineshapes in multi-level atomic systems. *J. Phys. B*, 10(10):1815–1833, 1977.
- [9] William Happer. Optical pumping. 44(2):169–249, 1972.
- [10] William Happer. Multipole relaxation times of a weak perturbing spin system. *Phys. Rev. B*, 1(5):2203–2207, 1970.
- [11] S. Lang, S. I. Kanorsky, M. Arndt, S. B. Ross, T. W. Hänsch, and A. Weis. The hyperfine structure of Cs atoms in the b.c.c. phase of solid ^4He . *Europhysics Letters*, 30(4):233, 1995.
- [12] A. Abragam. *The principles of nuclear magnetism*. Clarendon Press, Oxford, 1961.
- [13] V. J. Minkiewicz, T. A. Kitchens, F. P. Lipschultz, R. Nathans, and G. Shirane. Phonon spectrum of hcp He^4 . *Rev. Mod. Phys.*, 174(1):267, 1968.
- [14] Steffen Lang. *Optisch detektierte Magnetresonanz an Cäsium Atomen in festem ^4He* . Ph.D. thesis, Ludwig-Maximilians-Universität München, 1997.
- [15] Karl Blum. *Density matrix theory and application*. Plenum Press, New York, second edition, 1996.
- [16] Mitchel Weissbluth. *Photon-Atom Interactions*. Academic Press, London, 1989.
- [17] Wolfram Research, Inc. *Mathematica*. Wolfram Research, Inc., Champaign, Illinois, 2002. Version 4.2.1.0.
- [18] R. Müller-Siebert, D. Nettels, and Antoine Weis. To be submitted.

Chapter 6

Magnetic and electric properties of alkali atoms in solid helium

D. Nettels, R. Müller-Siebert, X. Huang, S. Ulzega, and A. Weis

Département de Physique, Université de Fribourg, Chemin du Musée 3, 1700 Fribourg, Switzerland

published in *PHYSICA B* **329**, 406 (2003)

Abstract: The magnetic properties of alkali atoms implanted in crystalline ^4He matrices are extremely sensitive to the symmetry of the local trapping sites. For Cs atoms trapped in the body-centered-cubic phase of ^4He spin relaxation times up to 1 s have been observed. In the hexagonal-close-packed phase on the other hand the Cs spins are readily depolarized and a number of phenomena specific for this phase, such as zero field magnetic resonance spectra, forbidden transitions and anomalous hyperfine shifts have been observed in magnetic resonance experiments with optical detection. Our present interest focuses on spin perturbations of implanted Cs atoms by strong (30 kV/cm) external electric fields. These perturbations are measured as shifts of the magnetic resonance lines using a phase-sensitive optical magnetic resonance technique.

6.1 Introduction

Since the 1990s several lower temperature research groups have investigated atomic, ionic and molecular defects in superfluid ^4He (He II). Mainly optical and motional properties have been studied, whereas magnetic resonance studies were limited by the relatively short observation times. To overcome this problem we have chosen to use solid helium as a host matrix for high resolution spectroscopy of paramagnetic (alkali) impurity atoms. The solid matrix offers the advantage of extremely long trapping times. As in superfluid helium the impurity atoms reside in bubble-like cavities and have long spin relaxation times due to the diamagnetic character of ^4He . In particular in the body-centered-cubic (b.c.c.) phase of ^4He , where the trapping sites show a perfect spherical symmetry, longitudinal spin relaxation times T_1 of 1-2 seconds

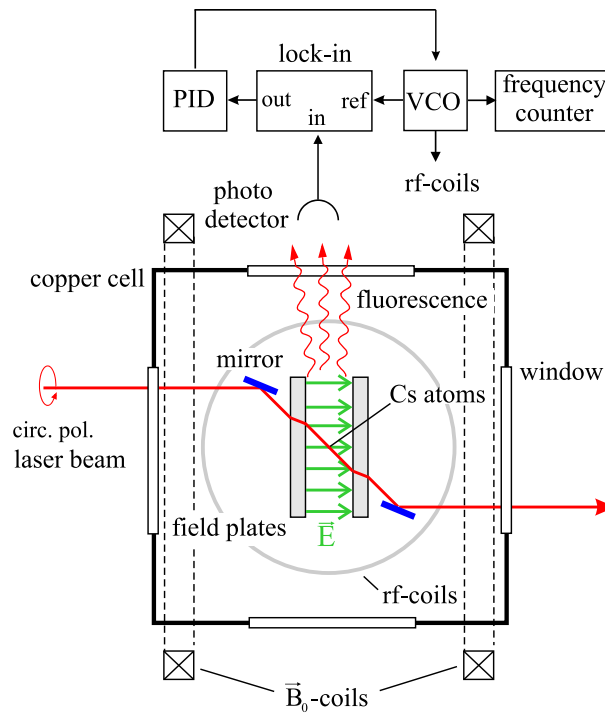


Figure 6.1: Top view of the solid ^4He pressure cell and of the phase-sensitive detection scheme.

and intrinsic transverse relaxation times T_2 up to 100 ms have been measured [1]. The narrow magnetic resonance lines open the door to high resolution spectroscopy[2]. One challenging perspective for the use of solid He trapped heavy alkalis is the search for permanent electric dipole moments (edm) of atoms whose existence is forbidden unless the discrete symmetries P (parity) and T (time reversal) are violated[3]. The experimental signature of an edm is a tiny linear Stark shift of a magnetic resonance line. In this work we present our new setup for measurements in strong electric fields (up to 30 kV/cm) using a phase stabilized magnetic resonance technique.

6.2 Setup

A helium crystal is grown inside a copper pressure cell [4]. Five windows give optical access from three orthogonal directions. The cell is loaded from a solid Cs target by using laser ablation with a frequency-doubled Nd:YAG-laser beam. The cesium atoms are detected by monitoring their fluorescence at 888 nm induced by excitation of the D_1 transition at 850 nm with a diode laser. The optical absorption and emission lines are blue shifted with respect to the corresponding vacuum values. The pressure cell is surrounded by magnetic field coils. Two layers of μ -metal suppress laboratory magnetic fields by three orders of magnitude. Radio-frequency coils and a pair of electric field plates are inside the cell. The electric field plates are made of float glass, which is coated on one side with a conducting layer of tin oxide. The advantage of these electrodes is their optical transparency (80%) at 850 nm and their extreme flatness and high conductivity at 1.5 K. Quartz spacers provide a defined separation of 0.6 cm between the plates. Fields up to 30 kV/cm were applied.

6.3 The phase stabilized magnetometer

Spin perturbations of the Cs atoms are measured by operating the sample as a phase-locked magnetometer. The magnetometer is based on the facts that Cs atoms irradiated by circular polarized resonant D_1 -radiation become spin polarized by optical pumping and that the optical absorption coefficient α of the atoms depends on the relative orientation of the spin polarization \mathbf{P} with respect to the the \mathbf{k} -vector of the light.

The sample is situated in parallel static magnetic and electric fields \mathbf{B}_0 and \mathbf{E} . The laser beam has an angle of $\alpha = 45^\circ$ with respect to the field directions (see Fig.6.1). The spin polarization produced by optical pumping along \mathbf{k} precesses around the magnetic field. This precession is driven by an oscillating radio-frequency magnetic field \mathbf{B}_{rf} perpendicular to \mathbf{B}_0 and produces a modulation of the absorption coefficient at the radio-frequency, which can be efficiently monitored by measuring the fluorescence light with a lock-in detector. The signal of interest is the phase between the rf-field and the system response, which shows a resonant dispersively-shaped enhancement when the rf-frequency matches the Larmor frequency of the static field. This signal is fed back via a PID-amplifier to a voltage-controlled oscillator (VCO) supplying the rf-coils. In this way the radio-frequency can be phase-locked to the Larmor frequency.

We have investigated the magnetometric sensitivity and stability of the system by recording the Allan-variance of the Larmor frequency. Fig. 6.2 shows a typical result at a Larmor frequency $\nu_L = 77.2$ kHz. The falling slope up to an integration time of 100 s can be ascribed to the white noise characteristic of the current source driving the \mathbf{B}_0 -coils. On longer time scales the system shows drifts of yet unexplained origin.

Stark effect measurements are in progress. Preliminary calculations have shown that the quadratic Stark splitting due to the tensor polarizability of the Cs ground state can be measured with the presented magnetometer, too. The vacuum value has recently been remeasured by our group[5].

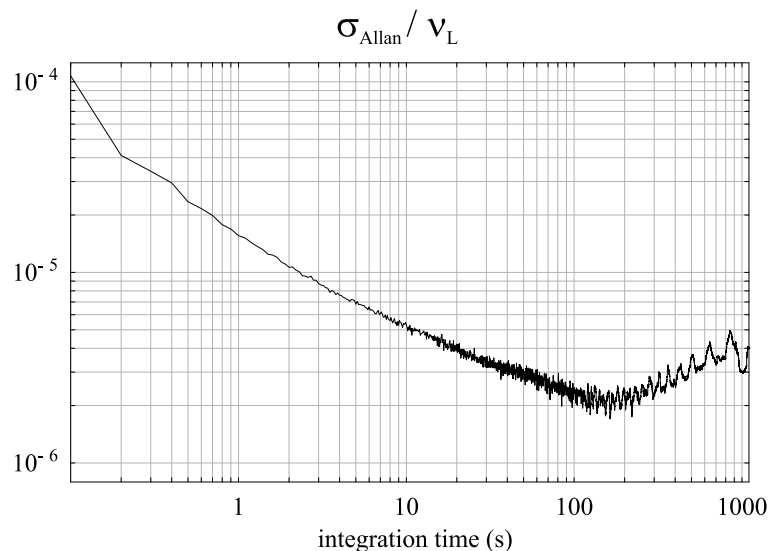


Figure 6.2: Allen variance σ_{Allan} in units of the Larmor frequency $\nu_L = 77.2$ kHz against integration time.

Acknowledgments

This work was supported by a grant of the Schweizerischer Nationalfonds.

References

- [1] S. I. Kanorsky, S. Lang, S. Lücke, S. B. Ross, T. W. Hänsch, and A. Weis. Millihertz magnetic resonance spectroscopy of Cs atoms in body-centered-cubic ^4He . *Phys. Rev. A*, 54(2):R1010, 1996.
- [2] Taro Eichler, R. Müller-Siebert, Daniel Nettels, S. I. Kanorsky, and A. Weis. Optical detection of nonradiating alkali atoms in solid helium. *Phys. Rev. Lett.*, 88(12):123002, 2002.
- [3] E. M. Purcell and N. F. Ramsey. On the possibility of electric dipole moments for elementary particles and nuclei. *Rev. Mod. Phys.*, 78:807, 1950.
- [4] S. Lang, S. I. Kanorsky, T. Eichler, R. Müller-Siebert, T. W. Hänsch, and A. Weis. Optical pumping of Cs atoms in solid ^4He . *Phys. Rev. A*, 60(5):3867, 1999.
- [5] C. Ospelkaus, U. Rasbach, and A. Weis. Measurement of the forbidden tensor polarizability of Cs using an all-optical Ramsey resonance technique. *Phys. Rev. A*, 67:011402, 2003.

Danksagung

Das Helium-Experiment besteht nun seit mehr als zehn Jahren. Der Pioniergeist der Anfangsjahre hat sich gelegt, und der Weg zur Messung eines EDM's hat sich als steinig erwiesen. Unser Spezialgebiet lebt aber bekanntlich von je her nicht nur von dieser einen - Nobelpreis trächtigen - Perspektive. Am Wegesrand wachsen reichlich andere exotische Pflanzen, denen wir Namen wie zum Beispiel "Optischer Blasenzyklus" oder auch "Nullfeldresonanz" gaben. Froh bin ich, dass auch ich schliesslich meine Pflänzchen gefunden habe. Ich möchte daher all' denen danken, die zum Gelingen dieser Arbeit beitrugen.

An erster Stelle ist hier Prof. Antoine Weis zu nennen. Tun bin ich in vielerlei Hinsicht zu Dank verpflichtet. Er hat es ermöglicht, dass ich etwas herum gekommen bin in der Welt. Am Anfang meiner Doktorarbeit schickte er mich für ein halbes Jahr nach England zu Professor Ed Hinds, dem ich an dieser Stelle mitsamt seiner Forschungsgruppe auch meinen Dank aussprechen möchte. Ich war noch nicht aus England zurück, da hiess es, dass die nächste Station Fribourg sei. Ich freute mich auf dieses neue "Abenteuer", welches den Umzug der gesamten Arbeitsgruppe von Bonn in die Schweiz bedeuten sollte. Auch die Konferenzen, die mich bis nach St. Petersburg und Japan führten, sind hier zu nennen.

Vor allem aber möchte ich mich bei Tun dafür bedanken, dass er immer ein guter Chef und Lehrer war, der alles zusammenhält, und mit dem man auch über ausser-physikalische Dinge gut reden kann. Von seiner vielgelobten Begeisterung für die Physik habe auch ich mich anstecken lassen.

Sehr stimulierend waren für mich ebenso die vielen interessanten Kaffeepausendiskussionen, die wir zusammen mit Robert Wynands führten. Leider war Robert nur kurz bei uns in Fribourg tätig. Ihm und Prof. Jean-Claude Dousse danke ich für ihr Interesse an meiner Arbeit und dafür, dass sie sich bereit erklärten, die Begutachtung zu übernehmen.

Mein ganz spezieller Dank gebührt natürlich dem Kryo-Team. Die Arbeit am Heliumexperiment ist nur im Team möglich. Ohne engagierte Mitarbeiter kommt man da nicht weit. Auch braucht man am Anfang eine gute Einführung in die Handhabung des Kryostaten. Diese haben in meinem Fall Taro Eichler und Reinhard Müller-Siebert besorgt.

Nachdem Taro unsere Gruppe verlassen hatte, war Reinhard der Erfahrenste unter uns. Er hat mit seinem technischen Know-how und seinem unermüdlichen Einsatz entscheidend zur Verbesserung der Apparatur beigetragen. Auch für die vielen fruchtbaren Diskussionen und das kameradschaftliche Verhältnis möchte ich danken.

Ebenso danke ich allen anderen ehemaligen Kryomitgliedern aus Bonner Zeiten: Sergej Karnorsky, Steffen Lang und Karoline Winkler.

Simone Ulzega und Adrian Hofer, in deren Händen zukünftig die Geschicke des Heliumexperimentes liegen werden, wünsche ich viel Erfolg, und ich danke für die gute Mitarbeit.

Seit Taros Weggang hat es immer an einem guten Post-Doc im Team gemangelt - bis dann endlich vor einigen Monaten Peter Moroshkin zu uns stiess. Ich danke ihm für sein reges Engagement und seine Hilfsbereitschaft. Die fruchtbaren Diskussionen mit ihm haben mir in den letzten Wochen vor der Abgabe dieser Arbeit sehr geholfen.

Weiterhin danke ich allen anderen Mitgliedern der Arbeitsgruppe. Mit Georg Bison und Ulrich Rasbach hatte ich eine sehr kameradschaftliche Zusammenarbeit. Beiden danke ich auch für den vielen gemeinsamen Spass im Labor und privat. Georg danke ich im speziellen für seinen grenzenlosen Optimismus, der keine unlösbaren Probleme kennt. Auch Stephan Gröger möchte ich danken. Er ist ein angenehmer Gesprächspartner, und ich wünsche ihm - ebenso wie Georg - viel Erfolg für die Doktorarbeit.

Mein erster wissenschaftlicher Erfolg war die Optische Magnetresonanztomographie. Ich

danke Guido Hinz und Dominik Giel, die meine Mitstreiter waren. Ebenfalls - aus Bonner Tagen - danke ich Christian Kurz, Björn Heitmann, Frank Rex und Gerhard Zündorf für die Zusammenarbeit. Und aus Fribourger Zeiten danke ich Patrick Haymoz, Christian Ospelkaus, Silke Ospelkaus-Schwarzer, Philippe Sproll, Stephan Tandler und Xueren Huang.

Von entscheidender Bedeutung für das Gelingen dieser Arbeit war auch die Kreativität und der Fleiss unserer hervorragenden Werkstätten. Direkten Kontakt hatte ich vor allem mit Elmar Moser, der in dringenden Fällen immer rasch eine Lösung parat hatte - mit Oswald Raetzo, für den immer alles kein Problem, sondern machbar war - mit Jean-Luc Schenker der schnell und zuverlässig unsere elektronischen Wünsche erfüllte - und mit Roland Schmid, der wie die anderen viel für uns gearbeitet hat und dazu immer einen Scherz auf Lager hatte. Diesen und auch den übrigen Werkstattangehörigen möchte ich für ihre Arbeit danken.

Wie die Werkstätten, so trägt auch die Administration viel zu der allgemein guten Atmosphäre im Hause bei. Ich danke allen, dass immer alles so reibungslos abgelaufen ist. Mein besonderer Dank gilt Elisabeth François, die uns Doktoranden weitestgehend alle Formalitäten abnimmt. Auch den Werkstätten und der Administration in Bonn am IAP sei gedankt.

Nadia möchte ich für ihre liebevolle Unterstützung und Geduld - in turbulenten, angespannten und fröhlichen Zeiten - ganz besonders herzlich danken!!!

Curriculum vitae

Personal details

Family name	Nettels
First name	Daniel
Date of birth	August 23, 1971
Place of birth	Münster, Germany
Nationality	German
Status	Single

School

1978 - 1984	Basic education in Papenburg, Germany
1984 - 1985	High School, Städtisches Gymnasium, Papenburg
1985 - 1991	High School, Kardinal-von-Galen-Gymnasium, Kevelaer, Germany
1991 - 1992	Zivildienst (community service), Marienhospital, Bonn, Germany

Studies

1992 - 1998	Studies in Physics, Rheinische Friedrich-Wilhelms-Universität Bonn, Germany
1998	Diploma work in Atomic Physics: <i>“Optische Magnetresonanztomographie an spinpolarisiertem Cäsiumdampf”</i> under the direction of Prof. Dr. Weis
Nov. 1998 - 2000	Graduate student in the research group of Prof. Dr. Weis, Institute for Applied Physics, University of Bonn, Germany
Jun. 1999 to Nov. 1999	Scientific visitor in the research group of Prof. Dr. Ed Hinds, University of Sussex, Brighton, England
since Apr. 2000	Graduate student in the research group of Prof. Dr. Weis, Department of Physics, University of Fribourg, Switzerland

Publications

1. D. Giel, G.Hinz, D. Nettels, and A. Weis. Diffusion of Cs atoms in Ne buffer gas measured by optical magnetic resonance tomography. *Opt. Express*, 6(13):251, 2000.
2. A. Weis, D. Giel, and D. Nettels. Motion of vapor atoms studied by optical magnetic resonance tomography. *Laser Phys.*, 11(4):470, 2001.
3. Taro Eichler, R. Müller-Siebert, Daniel Nettels, S. I. Kanorsky, and A. Weis. Optical detection of nonradiating alkali atoms in solid helium. *Phys. Rev. Lett.*, 88(12):123002, 2002.
4. D. Nettels, R. Müller-Siebert, X. Huang, S. Ulzega, and A. Weis. Magnetic and electric properties of alkali atoms in solid helium. *Physica B*, 329:406, 2003.
5. D. Nettels, R. Müller-Siebert, Simone Ulzega, and Antoine Weis. Multiphoton processes in the Zeeman structure of atomic Cs trapped in solid helium. (Accepted for publication by Appl. Phys. B.)
6. D. Nettels, R. Müller-Siebert, and Antoine Weis. Relaxation mechanisms of multi-quantum coherences in the Zeeman structure of atomic Cs trapped in solid He. (Invited paper. Accepted for publication by Appl. Phys. B.)
7. R. Müller-Siebert, D. Nettels, and Antoine Weis. Temperature stabilization of solid helium crystals by a double-circuit technique. (To be submitted.)
8. D. Nettels, A. Hofer, P. Moroshkin, R. Müller-Siebert, Simone Ulzega, and Antoine Weis. Observation of apple- and dumbbell-shaped Cs*He_n exciplexes in solid He⁴. (To be submitted.)

Awards

Poster Award: The 23d International Conference on Low Temperature Physics, Hiroshima (Japan), 20.-27. August 2002

Invited paper: D. Nettels, R. Müller-Siebert, and Antoine Weis.
Relaxation mechanisms of multi-quantum coherences in the Zeeman structure of atomic Cs trapped in solid He.
(Accepted for publication by Appl. Phys. B.)

Ich versichere, dass ich diese Arbeit selbstständig und ohne unerlaubte Hilfe verfasst und keine anderen als die angegebenen Quellen und Hilfsmittel benutzt sowie Zitate kenntlich gemacht habe.

1700 Freiburg (Schweiz), den 7. November 2003

A handwritten signature in black ink, appearing to read 'D. Nettels', with a stylized flourish extending from the end.

Daniel Nettels